

Ferroelectric and Resistive Switching in Epitaxial $\text{Hf}_{0.5}\text{Zr}_{0.5}\text{O}_2$

Von der Fakultät für Elektrotechnik und Informationstechnik der
Rheinisch-Westfälischen Technischen Hochschule Aachen zur Erlangung
des akademischen Grades einer

Doktorin der Naturwissenschaften

genehmigte Dissertation vorgelegt von

Judith Rebecca Knabe, M. Sc.

aus Neuss

Berichter*innen: Professorin Dr. rer. nat. Regina Dittmann
Professor Dr. rer. nat. Uwe Klemradt

Tag der mündlichen Prüfung: 26. August 2025

Diese Dissertation ist auf den Internetseiten der Universitätsbibliothek online verfügbar.

Curriculum Vitae

26.08.2025 Examination for Dr. rer. nat.
2021 – 2025 Research Assistant and Doctoral Candidate
Peter Grünberg Institute 7
Forschungszentrum Jülich GmbH & RWTH Aachen University
06.2021 Master of Science
2019 Exchange Semester at National Chiao Tung University (NCTU)
Hsinchu, Taiwan
2017 Exchange Semester at Pohang University of Science and Technology (POSTECH)
Pohang, Republic of Korea
08.2017 Bachelor of Science
2014 – 2021 Studies of Physics
RWTH Aachen University, Germany
2006 – 2014 General Higher Education Entrance Qualification (Abitur)
Albert-Einstein-Gymnasium, Kaarst, Germany
1996 born in Neuss, Germany

Abstract

As conventional CMOS technology approaches its scaling limits, alternative memory and logic device concepts are being actively pursued. Among these, resistive and ferroelectric switching mechanisms have emerged as promising candidates for non-volatile memory technologies due to their potential for high density, low power consumption, and compatibility with existing semiconductor processes. In particular, hafnium oxide-based materials stand out for their ability to support both valence change memory and ferroelectric switching phenomena at low thickness.

This thesis investigates the coexistence and independent operation of resistive and ferroelectric switching in epitaxial $\text{Hf}_{0.5}\text{Zr}_{0.5}\text{O}_2$ (HZO) thin films grown on $\text{La}_{0.8}\text{Sr}_{0.2}\text{MnO}_3$ (LSMO)-buffered SrTiO_3 . The crystalline model system is found to demonstrate both robust ferroelectricity and filamentary-type resistive switching within the same device, without the need for electroforming or external current compliance. Devices of this system exhibit reproducible polarization hysteresis loops upon AC bias, while resistive switching cycles can be initiated by quasi-static voltage sweeps. The resistive switching can be terminated through a standard RESET operation, returning to a pristine-like high-resistance state in which subsequent ferroelectric measurements can be performed. These findings demonstrate that the two switching modes are fundamentally decoupled and can operate in parallel in the same device under different electrical conditions.

X-ray photoemission electron microscopy and hard X-ray photoelectron spectroscopy are employed to characterize the spatial and electro-chemical nature of the switching mechanisms. The localized filament responsible for resistive switching is directly visualized, with associated valence changes identified at the HZO/electrode interface. Filament formation at a site of enhanced oxygen vacancy mobility is suggested, as such structures are identified as inherent to the system. In the ferroelectric switching regime, depth-dependent spectroscopy reveals subtle electro-chemical changes associated with oxygen vacancy migration across the thickness of the HZO layer under common switching conditions. Oxygen vacancies accumulate preferentially at the LSMO/HZO interface, superimposed by polarization direction-dependent redistribution and accompanied by reversible oxygen exchange with the LSMO electrode. Quantitative analysis confirms that the oxygen vacancy concentrations involved in ferroelectric switching are substantially lower than those observed during filamentary switching.

The dual-mode functionality established in this thesis, within which filamentary and ferroelectric switching mechanisms can coexist and be individually controlled within a single HZO-based device, highlights the pivotal role of oxygen vacancy dynamics, electrode interface engineering, and crystalline quality. It opens new paths for memory applications that can utilize the different strengths of both switching mechanisms and offers a unique platform for the study of oxygen vacancy dynamics and interface effects in hafnium-based systems.

Additionally, the integration of single-crystalline ferroelectric HZO as a free-standing membrane is explored, demonstrating phase stability across different substrates and under mechanical stress. It provides a foundation for future investigations, opening up possibilities for the integration of single-crystalline films into flexible electronics and CMOS-compatible architectures.

Kurzfassung

Da herkömmliche CMOS-Technologie an ihre Skalierungsgrenzen stößt, werden aktiv alternative Konzepte für Speicher- und Logikbauteile verfolgt. Unter diesen haben sich resistive und ferroelektrische Schaltmechanismen aufgrund ihres Potenzials für hohe Dichte, geringen Stromverbrauch und Kompatibilität mit bestehenden Halbleiterprozessen als vielversprechende Kandidaten für nichtflüchtige Speichertechnologien herauskristallisiert. Insbesondere Materialien auf Hafniumoxidbasis zeichnen sich durch ihre Fähigkeit aus, sowohl Valenzwechsel-Speichermechanismen als auch ferroelektrische Schaltphänomene bei geringer Dicke aufzuweisen.

In dieser Arbeit werden die Koexistenz und der unabhängige Betrieb von resistivem und ferroelektrischem Schalten in epitaktischen $\text{Hf}_{0.5}\text{Zr}_{0.5}\text{O}_2$ (HZO)-Dünnschichten untersucht, die auf $\text{La}_{0.8}\text{Sr}_{0.2}\text{MnO}_3$ (LSMO)-gepufferten SrTiO_3 gewachsen sind. Dieses kristalline Modellsystem zeigt sowohl robuste Ferroelektrizität als auch filamentäre resistive Schaltvorgänge innerhalb desselben Bauteils, ohne dass Elektro-Formierung oder externe Stromlimitierung erforderlich sind. Bauteile dieses Systems zeigen bei Wechselspannung reproduzierbare Polarisations-Hysteresen, während resistive Schaltzyklen durch quasi-statische Spannungsverläufe ausgelöst werden können. Das resistive Schalten kann durch einen regulären RESET-Vorgang beendet werden, wodurch eine Rückkehr zu dem ursprünglichen Zustand mit hohem Widerstand ermöglicht wird, in dem nachfolgendes ferroelektrisches Schalten durchgeführt werden kann. Diese Ergebnisse zeigen, dass die beiden Schaltmodi voneinander entkoppelt sind und unter verschiedenen elektrischen Bedingungen parallel in demselben Bauteil betrieben werden können.

Röntgen-Photoemissionselektronenmikroskopie und Hartröntgen-Photoelektronenspektroskopie werden eingesetzt, um die räumliche und elektrochemische Natur der Schaltmechanismen zu charakterisieren. Das für das resistive Schalten verantwortliche lokalisierte Filament wird sichtbar gemacht und die damit verbundenen Valenzänderungen an der HZO/Elektroden-Grenzfläche werden identifiziert. Die Filamentbildung wird an einer Stelle mit erhöhter Sauerstoffleerstellenmobilität vermutet, da solche Strukturen als systemimmanent identifiziert werden. Im ferroelektrischen Schaltmodus zeigt tiefenabhängige Spektroskopie subtile elektrochemische Veränderungen, die mit der Sauerstoffvakanzmigration entlang der Dicke der HZO-Schicht unter realistischen Schaltbedingungen verbunden sind. Sauerstoffvakanz sammeln sich bevorzugt an der LSMO/HZO-Grenzfläche an, überlagert von einer polarisationsrichtungsabhängigen Umverteilung und begleitet von einem reversiblen Sauerstoffaustausch mit der LSMO-Elektrode. Eine quantitative Analyse bestätigt, dass die Sauerstoffleerstellenkonzentration, die an dem ferroelektrischen Schalten beteiligt ist, wesentlich geringer ist als die des filamentären Schalten.

Die in dieser Arbeit etablierte Dual-Mode-Funktionalität, bei der filamentäre und ferroelektrische Schaltmechanismen in einem einzigen HZO-basierten Bauelement koexistieren und individuell gesteuert werden können, unterstreicht die zentrale Rolle der Sauerstoffleerstellen-Dynamik, der Elektrodengrenzflächengestaltung und der Kristallstruktur. Sie eröffnet neue Möglichkeiten für Speicheranwendungen, die die unterschiedlichen Stärken beider Schaltmechanismen nutzen kön-

nen, und bietet eine einzigartige Plattform für die Untersuchung von Sauerstoffleerstellen-Dynamik und Grenzflächeneffekten in Hafnium-basierten Systemen. Darüber hinaus wird die Integration von einkristallinem ferroelektrischem HZO als freistehende Membran untersucht, wobei die Phasenstabilität auf verschiedenen Substraten und unter mechanischer Belastung untersucht wird. Dies bildet die Grundlage für zukünftige Untersuchungen, um die Integration einkristalliner Schichten in flexible Elektronik und CMOS-kompatible Architekturen zu ermöglichen.

Contents

Abstract	5
Kurzfassung	7
1 Introduction	11
2 Fundamentals	15
2.1 Ferroelectricity	15
2.2 Resistive Switching	18
2.2.1 Valence Change Mechanism	19
2.3 Mixed-Valence Manganite - $\text{La}_{1-x}\text{Sr}_x\text{MnO}_3$	21
2.4 Ferroelectric Hafnium (Zirconium) Oxide	22
3 Experimental Techniques	27
3.1 Deposition Techniques	27
3.1.1 Pulsed Laser Deposition	27
3.1.2 Sputtering	28
3.1.3 Evaporation	30
3.2 Microstructuring Techniques	30
3.3 Atomic Force Microscopy	31
3.4 X-Ray Diffraction and Reflectometry	32
3.5 X-Ray Photoelectron Spectroscopy	33
3.6 X-Ray Absorption Spectroscopy	35
3.7 Photoemission Electron Microscopy	35
4 Growth of the Oxide-Heterostructures	37
4.1 Substrates	37
4.2 $(\text{La}, \text{Sr})\text{MnO}_3$	37
4.3 $\text{Hf}_{0.5}\text{Zr}_{0.5}\text{O}_2$	39
5 Sample Preparation	45
5.1 XPEEM Experiments	45
5.1.1 Graphene Electrode Samples	45

5.1.2	Electrode Delamination Samples	48
5.2	HAXPES Experiments	50
5.2.1	<i>Operando</i> Samples	50
5.2.2	Array-Type Samples	53
6	Electrical Characterization	55
6.1	Ferroelectricity	55
6.2	Resistive Switching	61
6.3	Dual-Mode Switching	67
7	Spectromicroscopic Analysis of the Switching Phenomena	73
7.1	Photoemission Electron Microscopy - Filamentary Switching	73
7.1.1	Stability under radiation	74
7.1.2	Filament & Reduced Structures	74
7.1.3	Shifts Near Needle Contact & Other Observations	82
7.1.4	SrO _x Segregation	86
7.2	Hard X-Ray Photoelectron Spectroscopy - Ferroelectric Switching	88
7.2.1	Stability under radiation	90
7.2.2	Hf 3 <i>d</i> vacancy profile	90
7.2.3	Mn 2 <i>p</i> vacancy profile	94
7.2.4	Summary	97
7.2.5	Array-type Samples	98
7.3	Dual-Mode Switching	100
8	Free-Standing Hf_{0.5}Zr_{0.5}O₂ Membranes	103
8.1	Fabrication	104
8.2	Phase Stability	106
8.3	Switching Characteristics	112
8.4	Summary	115
9	Conclusion and Outlook	117
A	Appendix	121
	Bibliography	121
	List of Publications	143
	Acknowledgements	145

1 Introduction

As complementary metal-oxide-semiconductor (CMOS) technology approaches its physical and thermodynamic limits with continued miniaturization, there is growing interest in alternative device concepts for data processing and memory applications. To overcome these scaling challenges, new materials and mechanisms are being investigated to complement traditional CMOS functionality [1, 2]. Among the most promising approaches are memory devices based on resistive switching phenomena, which offer potential for high-density, low-power, and non-volatile data storage solutions [3–5]. Resistive random access memory (ReRAM) devices operate by switching between distinct non-volatile resistance states when a voltage is applied. Within this category, valence change memory (VCM) devices rely on the electric-field-induced migration of mobile donors, which trigger localized redox reactions in the material. The devices typically feature a metal-oxide layer sandwiched between two metal electrodes, where one forms a Schottky barrier and the other establishes an ohmic contact with the oxide, allowing controlled resistive switching behavior [6–8]. During the operation of a VCM cell, a conductive filament composed of oxygen vacancies forms and dissolves within the oxide layer, establishing stable, non-volatile resistance states. Typically, initiating this switching behavior involves an electroforming step, essentially a soft dielectric breakdown, achieved using a higher bias than that required for subsequent switching cycles. This initial formation of a conductive filament irreversibly reduces the resistance of the oxide by a substantial degree [8–10].

Amorphous and crystalline hafnium oxide are, among other materials, commonly used high- k dielectrics and switching oxides utilized in VCM-based devices [11–13]. The filamentary nature of various other switching oxides employed in VCM-based applications has been explored [14–17]. In comparison, experimental insights into HfO_2 remain relatively limited, especially in systems utilizing oxide-based electrodes and standard biasing schemes. Consequently, further investigations into the electro-chemical nature of the filament and its behavior across different material systems are of significant interest.

Another promising mechanism for non-volatile resistance states is utilizing the switchable polarization of ferroelectrics. Ferroelectricity was first observed in 1921 in Rochelle salt, marking the beginning of a field that would later focus on more robust and technologically relevant materials [18]. Classic ferroelectric compounds that emerged are lead zirconate titanate (PbZrO_3 - PbTiO_3 , PZT) and barium titanate (BaTiO_3), which became widely studied due to their strong ferroelectric properties. These materials were early candidates for non-volatile memory devices via the integration into, e.g., ferroelectric random access memory (FeRAM). However, these materials face several limitations, including thickness scaling, as ferroelectric behavior often diminishes in

ultrathin films. Additionally, environmental concerns regarding the toxicity of lead-containing materials like PZT motivated the search for lead-free alternatives. Another critical obstacle was the integration of ferroelectrics with silicon-based CMOS technology. The high crystallization temperatures typically required to achieve ferroelectric phases often exceeded CMOS process limits, complicating direct integration [19–21]. The discovery of CMOS-compatible ferroelectricity in HfO₂-based thin films in 2011 solidified the relevance of ferroelectric thin films as part of non-volatile memory technology [22–24]. Crystalline hafnium oxide has been shown to adopt a ferroelectric orthorhombic phase, e.g., by doping with several possible materials or via mechanical stress, typically introduced through annealing under strain [22, 25]. Within HfO₂-based systems, Hf_xZr_{1-x}O₂ has emerged as a particularly promising candidate [26, 27]. Additionally, in epitaxial Hf_{0.5}Zr_{0.5}O₂ (HZO), a rhombohedral ferroelectric phase has been identified, and studies emphasize the significant influence of substrate-induced stress and choice of bottom electrode [28–31].

While the crucial role of oxygen vacancies in filamentary switching is well established, their influence on ferroelectric switching in HfO₂-based films continues to be actively researched. The presence and redistribution of oxygen vacancies have been shown to critically affect the ferroelectric properties of hafnium oxide systems [32–34]. Bias-induced structural changes linked to oxygen migration have been observed in HZO and at La_{0.67}Sr_{0.33}MnO₃/HZO interfaces [35]. However, depth-dependent chemical modifications under electrical cycling, along with the associated degradation mechanisms, remain subjects of ongoing investigation and discussion.

Generally, ferroelectric and VCM-based filamentary switching are expected to be mutually exclusive on a single device level, as the irreversibly lowered resistance after electroforming masks ferroelectric switching. While there are isolated studies reporting the coexistence of ferroelectricity and resistive switching in polycrystalline HfO₂, these studies demonstrated that ferroelectric switching could not be restored after VCM switching was performed, or that a deep reset was required to thermally dissolve the filament, which could only be triggered in few devices [36, 37]. Jiang et al. reported the coexistence of ferroelectric and resistive switching in polycrystalline HZO, demonstrating the ability to switch between the two modes. However, electroforming was still necessary to initiate resistive switching. Subsequently, a current compliance was required to sustain the resistive switching and high reset currents to revert to ferroelectric switching afterward [38]. Devices that allow the reversible operation between both mechanisms upon normal SET, RESET, and ferroelectric switching are yet to be reported.

In this work, the coexistence and interchangeable operation of ferroelectric and resistive switching in epitaxial HZO is established and investigated. Hf_{0.5}Zr_{0.5}O₂ is epitaxially grown on La_{0.8}Sr_{0.2}MnO₃ (LSMO) buffered SrTiO₃, a material system that has been shown to exhibit stable ferroelectricity in a wide growth window [28–30, 39]. In this crystalline model system, filamentary switching is observed without the need for electroforming or current compliance, within devices that also demonstrate ferroelectric switching characterized by distinct hysteresis loops. The transition from resistive switching back to ferroelectric switching is explicitly possible via the standard RESET operation. The parallel, yet non-interfering observation of these two switching modes, characterized in Chapter 6, establishes them as disconnected mechanisms taking place on different time and voltage scales within the same device.

The use of this system, with unique dual-mode operation of ferroelectric and filamentary-type resistive switching, enables the extension of experimental studies on oxygen-deficient filaments to an epitaxial model system. The highly localized filaments in the resistive switching mode are identified, which is of particular interest given that an oxide electrode functions as both an oxygen reservoir and an internal current limiter, allowing forming-free switching behavior and the absence of an external current compliance. Additionally, the enhanced oxygen mobility in crystalline HZO and the phase dependence of its resistive switching behavior [40, 41] can be expected to produce deviations from previously reported results on amorphous or metal/oxide structures. Addressing this requires high spatial resolution while simultaneously preventing filament re-oxidation, posing a significant experimental challenge. It is approached by *operando* experiment design for surface-sensitive X-ray photoemission electron microscopy (XPEEM) in Section 7.1, where filaments are identified via the detection of a local valence change at the HZO/electrode interface. Thus, it demonstrates the direct characterization of a previously unexamined filament in orthorhombic hafnium (zirconium) oxide.

Regarding the ferroelectric switching, polarization charges are expected to impact both the top and bottom interface of the HZO, depending on the polarization direction. Consequently, high-energy X-rays are required to access both the surface and the buried LSMO/HZO interface. Various effects may contribute to or overlap with the initial migration of oxygen vacancies during ferroelectric switching. These include the internal electric field generated by polarization charges, which can induce vacancy (re-)migration over extended timescales, as well as adsorbates that introduce surface charges on exposed oxide regions [42, 43]. To capture the redistribution of oxygen vacancies in both HZO and LSMO under conditions closely representative of actual ferroelectric switching, including representative electrical biasing and device geometry, an *operando* experimental approach is essential. This methodology provides further significant benefits by eliminating device-to-device variability, which would otherwise complicate state comparisons across separate devices. Using *operando* HAXPES, the analysis of core-level spectral line shapes and binding energy shifts in Section 7.2 uncovers correlated electro-chemical modifications at both the oxide surface and the buried LSMO/HZO interface. This allows for the identification of depth-dependent variations in oxygen vacancy concentration and distribution in HZO induced by ferroelectric field cycling.

Lastly, the potential of ferroelectric HZO as a free-standing membrane is explored in Chapter 8. This technique opens up the possibility of integrating epitaxially grown film into CMOS technology. Here, the focus of this work lies in investigating the stability of the ferroelectric orthorhombic phase in membranes transferred onto different substrates, subjected to heat treatment, and upon bending in the context of potential application in flexible electronics.

The required theoretical background is introduced at the beginning of this work, in Chapter 2. A description of relevant experimental methods is given in Chapter 3, followed by the growth and sample preparation in Chapters 4 and 5. A conclusion of the work and outlook on possible future investigations is given in Chapter 9.

2 Fundamentals

2.1 Ferroelectricity

Ferroelectric materials exhibit a spontaneous electric polarization that arises due to their unique crystal symmetry. This polarization can be reoriented by applying an external electric field, which is the defining characteristic of ferroelectricity. The existence of two distinct polarization states originates from two energetically equivalent, but structurally different polar crystallographic configurations within a unit cell. This bi-stable nature makes ferroelectrics valuable for memory and switching applications.

Ferroelectric materials exhibit a hysteretic polarization behavior when subjected to an external electric field (Figure 2.1b). The polarization P , defined as the electric dipole moment density (Cm/m^3), does not change linearly with the applied field but instead follows a characteristic hysteresis loop. When the external electric field exceeds a critical value known as the coercive field E_C , the polarization switches direction. This switching process results from domain reorientation, where the alignment of dipoles within the material adapts to the applied field. Unlike linear dielectric materials, where polarization is purely induced and disappears when the field is removed, ferroelectrics retain a remanent polarization P_r , even after the external field is set to zero. The polarization of an ideal ferroelectric crystal persists up to the Curie temperature T_C , above which the material undergoes a phase transition to a non-polar (typically paraelectric) state [44–46]. On a microscopic level, ferroelectric materials consist of many domains. Domains are microscopic regions where the polarization is aligned in a uniform direction. In an un-poled sample, these domains are randomly oriented, leading to a net polarization of $P = 0$. Ferroelectric switching does not occur uniformly across the entire material. When an electric field is first applied, the polarization increases as domains realign with the field direction. The domain evolution during switching is a complex process involving the nucleation of new domains and the movement of domain walls. Their nucleation starts at the electrodes, then the domains grow perpendicular to the electrodes and widen, progressively reorienting the overall polarization of the ferroelectric. Depending on the material and thickness, either the nucleation of reversed domains or the domain wall motion is the kinetically limiting process during switching [47–49]. Since some dipoles return to a randomized state, the resulting remanent polarization without applied field (P_r , Figure 2.1b) is typically lower than the saturation polarization reached with a field applied.

To reduce the polarization back to zero, an electric field in the opposite direction ($-E_C$) must be

applied. Beyond this threshold, the polarization follows a symmetric hysteresis loop but in the negative direction. This repeatable, switchable behavior is the fundamental property of ferroelectricity, making these materials promising for non-volatile memory, capacitors, and piezoelectric devices [44–46].

To experimentally observe and measure ferroelectric switching, an electric field is applied across the electrodes enclosing the ferroelectric material. The resulting current includes a dielectric displacement current, which originates from the charging of the capacitor formed by the electrodes and the ferroelectric layer in between. However, when a field of opposite polarity is applied, the current consists of two components: The displacement current due to charging and an additional current component resulting from the reorientation of domains, which is known as the ferroelectric switching current I_f . By comparing the total current in both field directions, the ferroelectric contribution can be isolated and analyzed.

The polarization P is approximated by the surface charge density and is obtained using the following integral expression:

$$P \approx \frac{Q}{A} = \frac{1}{A} \int_{t_0}^{t_1} I_f dt \quad (2.1)$$

Where the ferroelectric displacement current I_f is integrated over a time span that covers the complete polarization reversal, from time t_0 to t_1 , and normalized by the capacitor area A . This integral represents the net charge displacement due to ferroelectric switching.

In practice, real ferroelectric materials deviate from the ideal capacitor model due to their inherent resistive properties. This manifests as a leakage current I_R , which arises from the finite conductivity of the ferroelectric material. The leakage current follows Ohm's law: It is proportional to the externally applied voltage V_{ext} and inversely proportional to the resistance R :

$$I_R = \frac{V_{ext}}{R} \quad (2.2)$$

Here, the resistance R is typically assumed to be independent of the frequency of the applied voltage [46, 50]. In polarization measurements, I_f and I_R can not fully be told apart. Therefore, it is important that the leakage current is small compared to I_f . Otherwise, the polarization obtained from Equation 2.1 is incorrectly overestimated.

Leakage current generally plays a crucial role in device performance, as excessive leakage can degrade the stability and reliability of ferroelectric switching, affecting applications in memory and logic devices. Thus, optimizing material properties to minimize leakage while maintaining robust switching characteristics, especially when reducing the thickness, is a key challenge in ferroelectric technology.

The characteristic parameters of a ferroelectric thin film, the remanent polarization P_r , and the coercive field E_C are obtained from the hysteresis as described above. In practice, a voltage is applied to the film, and the resulting current is analyzed. For the measurements in this work, an aixACCT TF Analyzer 3000 is used. Multiple defined triangular voltage pulses are applied, in the

sequence shown in Figure 2.1a. The dashed pulses act as pre-polarization pulses, setting the device into a defined negative and positive polarization state, respectively, before the actual hysteresis measurement. Subsequently, another pulse cycle of the same polarity is applied, measuring the relaxed remanent polarization ($P_{r,relaxed}$) for each polarity. Following this, a hysteresis curve as in Figure 2.1b is constructed. From the red half-cycles in the pulse sequence, the dynamic hysteresis can be extracted. The resulting curve gives the remanent polarization instead of the relaxed remanent polarization, meaning the polarization immediately after removing the bias.

Square voltage pulses of a defined frequency are applied, in case the polarization is supposed to switch for an extended time without a hysteresis measurement. This is commonly used to induce so-called fatigue (see Section 2.4) in the ferroelectric material, analyzing the degradation process.

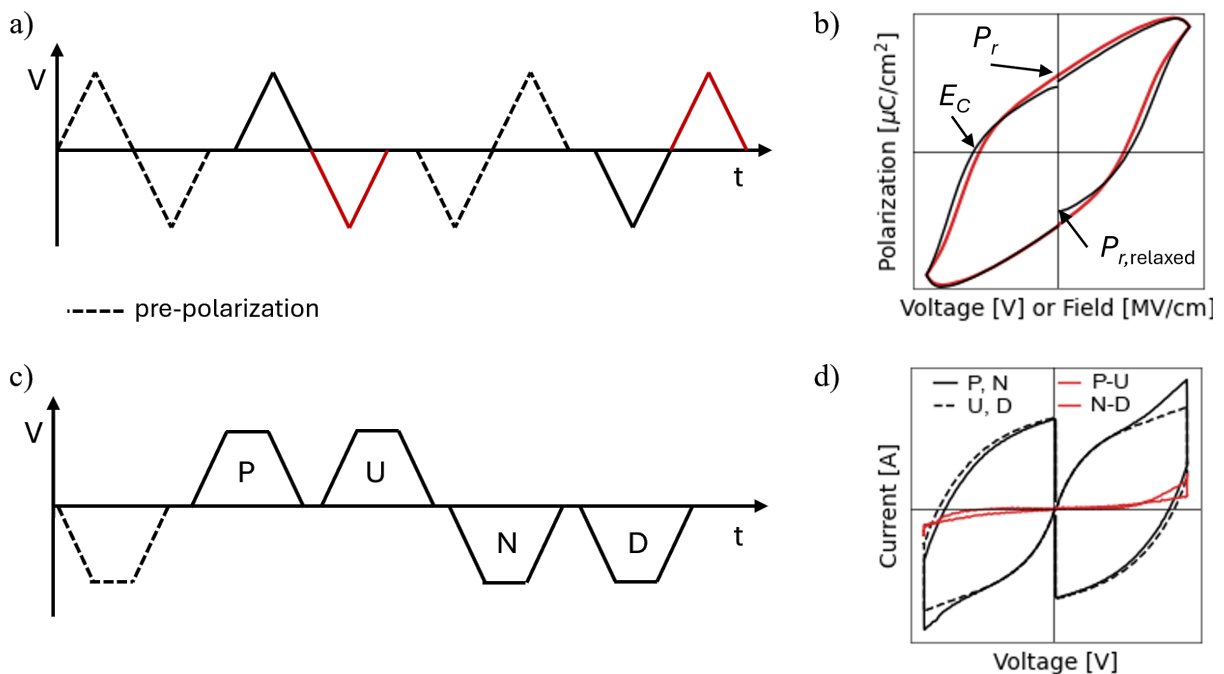


Figure 2.1: a) Pulse sequence for a dynamic hysteresis measurement b) Extracted dynamic (red) and relaxed (black) hysteresis with key parameters labeled. c) Pulse sequence for a PUND measurement. For both polarities, a switching (P and N) and non-switching (U and D) pulse are applied. d) Extracted current response for the switching and non-switching pulses. The difference in red corresponds to the ferroelectric contribution.

In the case of less insulating devices, the leakage current superimposed on the displacement current and ferroelectric switching current can severely distort the measured dynamic hysteresis. A typical way to tell apart the ferroelectric contribution from the other contributions is the so-called PUND (Positive-Up Negative-Down) measurement protocol. Consecutive voltage pulses are applied in a specific sequence (see Figure 2.1c): First, a pre-polarizing pulse sets the device into a defined state. Then a positive pulse (P) switches the polarization in one direction, followed by a second (non-switching) positive pulse (U). A negative pulse (N) reverses the polarization, while the subsequent

negative pulse (D) measures the non-switching response. By calculating the difference between the measured current transients of switching and non-switching pulses, the purely ferroelectric contribution can be determined [44]. This difference is shown in red in Figure 2.1d, for an exemplary leaky ferroelectric, which is further subjected to insufficiently high bias. The PUND measurement enables to still identify ferroelectricity, and an integration over the red current contribution can offer a rough estimation of P_r .

The non-volatile character of two polarization states leads to the obvious application in ferroelectric memories. A ferroelectric capacitor together with a transistor forms a ferroelectric random-access memory (FeRAM), where the data is stored in the polarization state of the capacitor. Reading the stored data requires applying a voltage above E_C to check whether the polarization direction changes. This process is destructive, requiring that the data is rewritten after each read operation. In a ferroelectric field-effect transistor (FeFET), in turn, the ferroelectric is integrated into the gate stack of a field-effect transistor. The source-drain current is then modulated by the polarization state, offering the advantages of a non-destructive readout and reduced memory device size. Ferroelectric tunnel junctions (FTJ) use a thin ferroelectric layer between two different electrodes to modulate the tunneling current through the ferroelectric material itself or an adjacent dielectric tunnel barrier. A difference in screening by the electrodes results in a higher or lower average tunneling barrier depending on the polarization direction. FTJs also offer non-destructive readout and scaled-down device sizes [45, 51].

2.2 Resistive Switching

Resistive switching phenomena can be attributed to various underlying physical mechanisms, including electrical effects, phase change mechanisms, and nanoionic effects driven by redox reactions. In this study, the resistive switching behavior is primarily governed by the latter mechanism, where redox-based ionic migration plays a crucial role in modulating the resistance states of a device [4].

Resistive switching can generally be categorized into two distinct operational modes, namely unipolar and bipolar switching, which differ based on the voltage polarity required for switching. In the unipolar switching mode, the transition between high-resistance (HRS) and low-resistance state (LRS) is independent of the polarity of the applied voltage. A current compliance is typically employed during the SET process (switching to the on-state) to limit the current and protect the device from excessive power dissipation. Conversely, during the RESET process (switching to the OFF-state), the current is significantly higher, and the RESET voltage is lower than the SET voltage. In contrast, the bipolar switching mode exhibits a polarity-dependent switching mechanism, where the SET transition occurs at one voltage polarity while the RESET transition occurs at the opposite polarity. Depending on the material system and device architecture, a current compliance may be applied during the SET operation to prevent damage or unintended degradation of the switching layer. This mode is often associated with electrochemical redox reactions and the formation and dissolution of conductive filaments, which dictate the resistive switching characteristics [12, 52].

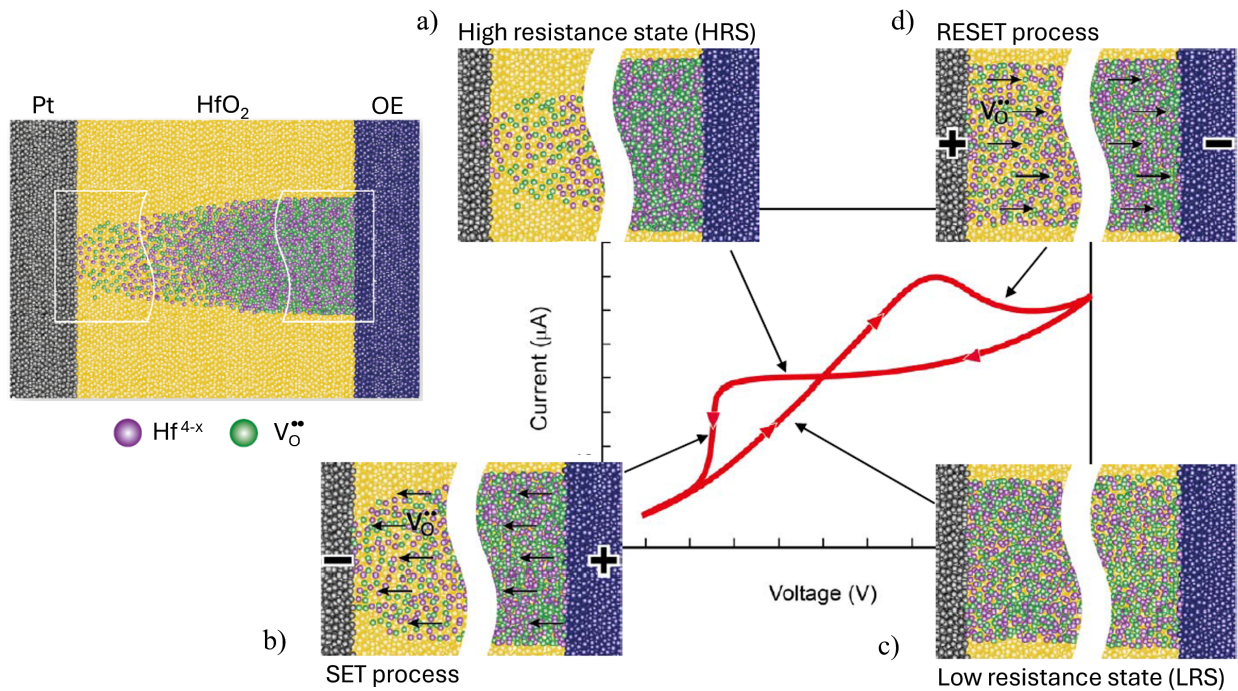


Figure 2.2: Schematic switching mechanism of *counter-eight-wise* filamentary switching. a) High resistance state. b) SET process: Upon negative voltage at the AE, oxygen vacancies migrate into the gap between AE and the disrupted filament, establishing the LRS. c) Low resistance state with fully established filament. d) RESET process: With a positive voltage the vacancies move back, breaking the conductive filament, restoring the HRS. Adapted with courtesy of Stephan Menzel.

2.2.1 Valence Change Mechanism

The resistive switching mechanism investigated in the material system of this work is the valence change mechanism (VCM). Therefore, a more detailed introduction to this mechanism is given in the following.

VCM is primarily driven by the migration of anionic species, particularly oxygen, where the process is typically described in terms of the movement of oxygen vacancies within the switching material. The redistribution of oxygen vacancies leads to localized changes in stoichiometry, resulting in oxidation or reduction within the switching material. This valence change directly influences the electronic properties of the device, as the modulation of the oxygen vacancy concentration acts as n-type doping. The formation or annihilation of oxygen vacancies alters the charge carrier density, thereby inducing a reversible change in resistance. The direction of the valence change, whether oxidation or reduction occurs, is dictated by the individual interfaces of the switching material in a system and the polarity of the applied voltage, defining the bipolar character of this switching mechanism [3, 8].

Figure 2.2 schematically illustrates the operation of a filamentary switching VCM cell. In this configuration, the voltage is referenced to the active electrode (AE), which exhibits a higher workfunction, here platinum. The counter electrode is an ohmic electrode (OE) with a lower

workfunction, e.g., titanium, and is connected to ground. The insulating oxide layer between the electrodes, e.g., HfO_2 , exhibits both ionic and electronic conductivity, enabling the migration of oxygen vacancies that govern the resistive switching behavior. In the HRS or OFF-state, a disrupted conductive filament (*plug*) is present within the insulating layer. However, it remains separated from the active electrode by a nanoscale region referred to as *disc*, which acts as a potential barrier, preventing significant current flow (Figure 2.2a). Upon applying a, in this case, negative SET voltage to the active electrode, oxygen vacancies migrate from the plug toward the disc region (Figure 2.2b). This localized reduction process decreases the Schottky barrier at the interface, effectively restoring the conductive pathway and switching the device into the LRS or ON-state (Figure 2.2c). Conversely, when a positive RESET voltage is applied, the double positively charged oxygen vacancies migrate back into the plug, leading to an oxidation process that re-establishes the insulating barrier. This restores the HRS, by effectively breaking the conductive filament once again (Figure 2.2d). This switching behavior follows a characteristic polarity known as *counter-eight-wise* switching [8, 10].

In *eight-wise* switching, in contrast, the SET and RESET processes occur at inverted polarities. This stems from an oxygen exchange at the oxide/AE interface (disc region) as opposed to the vacancy migration within the oxide. The key difference between the two types lies in which mechanism is dominating, the redistribution of vacancies in the switching oxide or the oxygen release and re-incorporation at an interface. Whether a system exhibits *eight-wise* switching, *counter-eight-wise* switching, or coexistence of both, depends on the chosen switching material, electrodes, and device architecture [53–55].

Typically, oxides used in VCM cells are very insulating when pristine. The cells, therefore, require an initial electroforming process, during which a high voltage is applied and the current is limited by a current compliance in the measurement setup to prevent unintentional damage. The applied bias, accompanied by Joule-heating, causes the formation of oxygen gas at the positive polarity electrode, which is incorporated into the electrode or forms a metal oxide, depending on the used material. This release introduces the required oxygen vacancies into the switching oxide via:



With O_{O}^{\times} representing an oxygen ion at an oxygen lattice site and $V_{\text{O}}^{\ddot{\cdot}}$ an oxygen vacancy (in Kroeger-Vink notation). This serves as a soft dielectric breakdown of the oxide, creating an asymmetry in the cell. The introduced vacancies drift towards the cathode under the applied bias, leading to the initial formation of a conducting filament creating the plug and, therefore, reducing the resistance of the oxide to a significant extent irreversibly. The electroforming does not only initiate the switching, but it can also have an impact on the switching behavior itself. Parameters like the forming polarity, sweep rate, and current compliance can influence the switching [9, 56].

For application in memory devices, highly non-linear switching kinetics are essential. These devices must transition within nanoseconds upon applying the SET voltage while maintaining their state for years under a read voltage. This behavior is primarily enabled by Joule heating, which exponentially accelerates the involved processes such as ion migration, redox reactions, and

electro-crystallization. Additionally, the applied bias contributes by lowering the activation energy required for these processes [8, 57].

SET and RESET voltages, as well as resistance states, inherently exhibit fluctuations, leading to cycle-to-cycle variability. These temporal variations within a single device arise from the random distribution and migration of defects, stochastic oxygen vacancy generation and recombination, and the coexistence of multiple (sub-)filaments. It has been observed that the current during the SET process plays a crucial role in determining this variability, as it directly influences the filament size. A higher current results in a larger filament, thereby reducing variability. Similarly, the chosen RESET voltage impacts the spread of the HRS. The extent of filament deconstruction dictates variability, with both (near) complete re-oxidation and an (almost) unchanged filament exhibiting reduced fluctuations [58–60].

For the operation of memristive devices, the logic '0' can be associated with the HRS, while the logic '1' corresponds to the LRS. It is further possible, to operate devices in an analog manner, utilizing multiple discrete resistance states. This is commonly achieved by adjusting the current compliance during the SET process, modifying the RESET voltage, or applying voltage pulses with varying amplitude and duration [61, 62].

2.3 Mixed-Valence Manganite - $\text{La}_{1-x}\text{Sr}_x\text{MnO}_3$

$\text{La}_{1-x}\text{Sr}_x\text{MnO}_3$ (LSMO) is a mixed valence manganite of perovskite ABO_3 crystal structure with Mn on the B site and La, Sr on the A site. It shows interesting electronic and magnetic properties, such as metal-insulator transitions and colossal magnetoresistance. However, in this work, only electrical properties are considered. LSMO can be regarded as a mix between the insulating $\text{La}^{3+}\text{Mn}^{3+}\text{O}_3^{2-}$ and $\text{Sr}^{2+}\text{Mn}^{4+}\text{O}_3^{2-}$.

The Sr doping results in partial replacement of La^{3+} with Sr^{2+} . This results in acceptor doping, which is compensated by a valence change of Mn^{3+} to Mn^{4+} , hence the classification as "mixed-valence". The resulting LSMO structure for $x \leq 0.3$ is shown in Figure 2.3a [63, 64]. At medium Sr doping levels ($x \approx 0.16$ until $x \approx 0.55$), the LSMO becomes conductive (and ferromagnetic) due to the *double exchange* mechanism. This is based on the electrons from Mn^{3+} hopping to Mn^{4+} via an oxygen ion, as sketched in Figure 2.3b. This transfer is energetically favorable but only possible for aligned spins, due to Hund's rule [65].

In this work, LSMO ($x=0.2$ and $x=0.3$) are used as conductive oxide bottom electrode and sacrificial layer to stabilize $\text{Hf}_{0.5}\text{Zr}_{0.5}\text{O}_2$ growth in the ferroelectric orthorhombic phase. LSMO is epitaxially grown via pulsed laser deposition on Ti-terminated SrTiO_3 (001) substrates.

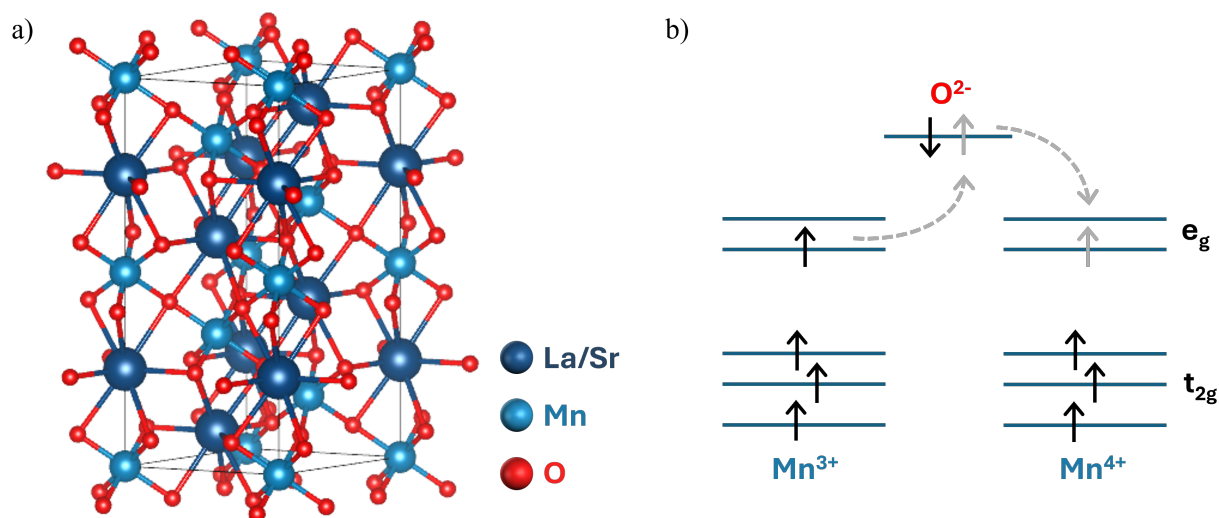


Figure 2.3: a) Rhombohedral (R3ch) $\text{La}_{1-x}\text{Sr}_x\text{MnO}_3$ $a = b = 0.551$, $c = 1.336$, parameters taken from literature [64] and structure drawn with [66]. b) Illustration of the spin states in Mn^{3+} – O^{2-} – Mn^{4+} . Double exchange occurs via electron hopping across the oxygen ion.

2.4 Ferroelectric Hafnium (Zirconium) Oxide

The discovery of ferroelectricity in hafnium oxide (HfO_2)-based thin films has sparked great interest in the field of materials science and nanoelectronics. Traditionally, ferroelectricity was associated with complex perovskite oxides, such as lead zirconate titanate (PZT) and barium titanate (BaTiO_3), which, despite their excellent ferroelectric properties, suffer from challenges including integration incompatibility with modern semiconductor processes, environmental concerns due to lead content, and size scaling limitations. In contrast, hafnium oxide, a material already established in CMOS technology as a high- k dielectric, presents a silicon-compatible, environmentally abundant, and highly scalable alternative.

The observation of ferroelectricity in both doped and undoped hafnia thin films has opened new possibilities for incorporating ferroelectric properties into semiconductor technologies. Notably, ferroelectric hafnium oxide exhibits robust ferroelectric behavior at nanoscale dimensions, even below 10 nm, a regime where traditional ferroelectrics typically lose their polar properties due to size effects [22, 23, 51].

The ferroelectricity of hafnia is based on the stabilization of a metastable non-centrosymmetric orthorhombic phase ($\text{Pca}2_1$), which does not exist in bulk hafnium oxide but can be induced and stabilized through factors such as doping (with elements like silicon, yttrium, or zirconium), oxygen deficiency, mechanical stress, and surface energy considerations. Despite significant progress, the fundamental mechanisms governing phase stabilization, domain switching dynamics, interface properties, and degradation of ferroelectric hafnia-based systems remain active areas of research. This section aims to provide a comprehensive overview of the fundamental principles governing ferroelectricity in hafnium oxide, with particular emphasis on its crystallographic structures, phase

stability, and the influence of processing conditions such as doping, annealing, and mechanical stress. Furthermore, the chapter reviews the current state of research concerning the physical mechanisms underlying wake-up, switching, and fatigue of ferroelectric hafnia thin films. Special emphasis is given to the epitaxial material system of $\text{Hf}_{0.5}\text{Zr}_{0.5}\text{O}_2$ grown on $\text{La}_{1-x}\text{Sr}_x\text{MnO}_3$ buffered SrTiO_3 , as this system is the subject of this work.

Stabilization

The fluorite crystal structure of HfO_2 does not include any thermodynamically stable polar phase in its phase diagram. Among the stable ones are the monoclinic $\text{P}2_1/\text{c}$ bulk phase shown in Figure 2.4a, a tetragonal and cubic phase, stable at high temperatures, and an anti- and a non-polar orthorhombic phase under high pressure [67]. The polar, ferroelectric orthorhombic $\text{Pca}2_1$ phase (o-phase in the following) can nevertheless be stabilized via various paths that manipulate the free energy and activation barriers of the different possible phases. In this o-phase, not the metal atoms, but four oxygen atoms of the crystal structure in Figure 2.4b are displaced vertically, depending on the polarization direction. One way to stabilize the o-phase is by doping the HfO_2 , where a wide range of possible dopants with varying atomic radii have been explored, including among others, Si, Zr, Y, Sr, Al. Increasing the doping concentration was found to increase the P_r , until the t- to o-phase transition gets suppressed, leaving the thin film tetragonal at higher doping concentrations [22, 25, 68–70]. Also, oxygen vacancies, introduced during deposition or scavenged by interfacing materials, were found to be suitable dopants, suppressing the m-phase and reducing the o-phase free energy [71, 72]. Zr has been found an especially favorable dopant, allowing a wide doping range while also lowering the crystallization temperature of the compound [25, 73]. The emergence of the o-phase is assigned to the tetragonal (t-) to o-phase transition due to mechanical stress and strain during the cooling phase of annealing the amorphous (doped) HfO_2 . This is closely connected to the capping of the HfO_2 by a top electrode and the mismatch of the thermal expansion coefficient of both layers or with the substrate, which suppresses the volume expansion that would be connected with a t- to m-phase transition during cooling [74–76].

The thickness dependence of the stabilization of the ferroelectric behavior is related to the surface and interface energy of the thin film. With varying grain sizes, largely influenced by the thickness, more or less symmetric phases become energetically favorable. Calculations showed that below the favorable grain sizes, the thin films become tetragonal and for larger grain sizes monoclinic. Also here, Zr doping was found to allow a wider thickness range. The additional application of an electric field was further found to lower the energy of the ferroelectric o-phase over the t-phase [27]. Contrary to these findings, to this day, from 1 nm up to 1 μm thick films of ferroelectric, (doped) HfO_2 have been fabricated [77, 78].

Switching behavior

Initially, as-deposited HfO_2 -based films exhibit suppressed polarization switching due to defects, non-ferroelectric regions, and internal bias fields. Upon electrical cycling, a phenomenon known as the wake-up effect occurs, characterized by an increase in remanent polarization and the open-

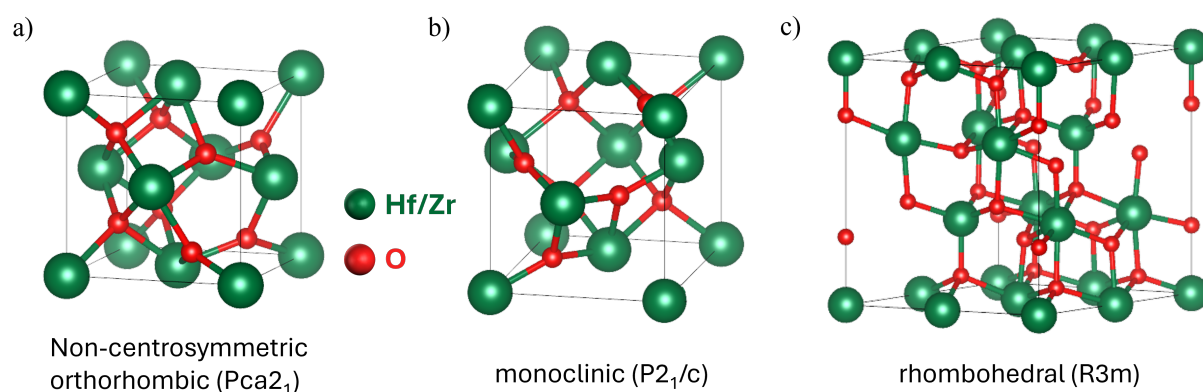


Figure 2.4: Selection of relevant phases of HfO₂. a) Polar orthorhombic phase Pca₂. b) Monoclinic bulk phase P₂/c. c) Polar rhombohedral phase R3m [28]. Structures drawn with [66].

ing of the hysteresis loop. This behavior is primarily attributed to field-induced redistribution of oxygen vacancies and the gradual depinning of domain walls. These processes reduce the internal bias and enhance domain mobility [32, 36, 79]. Additionally, field-driven t- to o-phase transition can be promoted. Generally, the switching in HfO₂-based thin films is limited by the nucleation of domains, so-called nucleation-limited switching (NLS), mediated by possible inhomogeneous fields and oxygen vacancy concentration [80, 81].

Continued cycling leads to fatigue, where the remanent polarization progressively degrades. The fatigue mechanism includes charge trapping at interfaces and grain boundaries, which locally screen the applied field and suppress domain switching. Furthermore, the migration and generation of defects, namely oxygen vacancies, lead to the formation of non-switchable regions and domain wall pinning. These trapped charges create internal fields opposing the polarization reversal and thereby reducing the polarization. Additional defects can further lead to an o- to m-phase transition, an increase in leakage current that superimposes the ferroelectric switching, or ultimately a dielectric breakdown [32, 82]. Notably, both wake-up and fatigue are strongly dependent on various factors such as film thickness, dopant type, grain size, and electrode configuration.

Understanding and controlling the wake-up and fatigue behavior is critical for optimizing the performance and reliability of HfO₂-based ferroelectric devices. Defect engineering, interface optimization, and tailored doping are, thus, widely investigated strategies to prolong stable ferroelectric switching.

Epitaxial HZO on LSMO

In addition to the intensely studied polycrystalline films, the development of epitaxial HfO₂ and Hf_{0.5}Zr_{0.5}O₂ (HZO) thin films has opened opportunities to investigate the intrinsic properties of ferroelectric hafnia. Epitaxial growth provides precise control over crystallographic orientation, strain state, and interface quality, all of which are critical factors influencing phase stability and ferroelectric performance, as described before. In particular, the integration of HZO with the conductive oxide electrode La_{1-x}Sr_xMnO₃ (mainly for x=0.33) (LSMO) has been utilized widely

to study interface effects and phase stability under well-defined structural conditions.

The t-phase stabilizes due to additional surface energy effects, relevant in thin films. During cooling the t- to o-phase transition takes place, further facilitated by epitaxial strain and the different lattice constants of the involved phases [83]. LSMO grown epitaxially, under tensile strain, leads to a pronounced o-phase in subsequently grown HZO, while compressive strain in the LSMO favors the m-phase. The strain in the HZO itself varies minimally, indicating that domain-matching epitaxy and the specific LSMO/HZO interface play a crucial role [29, 84]. The ferroelectric switching in such epitaxial systems typically does not show a pronounced wake-up, but a similar increase of the m-phase with increasing thickness as observed in polycrystalline films [28, 85].

The LSMO/HZO interface has been the subject of extended investigation. It was found that a manganite electrode is crucial, forming an interface reconstruction, where the Mn is partially replaced by Hf (and Zr) atoms under the subject of electron transfer, facilitating the heteroepitaxy. Other perovskite electrodes or higher Sr doping of the LSMO did not result in similarly pronounced ferroelectricity [30, 31, 86, 87].

It is also the LSMO/HZO epitaxial system where a further ferroelectric phase was found. Wei et al. identified a polar rhombohedral R3m phase (r-phase) in thin HZO, stabilized by compressive strain (Figure 2.4c) [28]. A few monolayers of highly strained tetragonal HZO form at the interface, which are believed to stabilize this polar r-phase under slightly oxygen-deficient conditions and due to tensile strain of the LSMO. DFT calculations revealed a large out-of-plane lattice constant to realize the polarization found for the r-phase [28, 86]. Although, experimentally the HZO lattice parameter does not vary much, opening up the possibility of a rhombohedral distortion of the o-phase emerging instead of a r-phase. The LSMO was further found to supply and take up oxygen during ferroelectric switching, depending on the applied voltage and time scale, demonstrating its active role in the ferroelectric performance of the material system [35].

3 Experimental Techniques

3.1 Deposition Techniques

3.1.1 Pulsed Laser Deposition

Oxides can be epitaxially grown using pulsed laser deposition (PLD), a versatile thin-film deposition technique. As illustrated in Figure 3.1a, PLD takes place within a vacuum chamber, where a high-energy nanosecond pulsed laser is directed onto a solid target material. Upon interaction with the laser pulse, the target surface is brought into a metastable state, leading to localized vaporization of the material. As the laser pulses continue, the vaporized material absorbs further energy, eventually forming a high-temperature plasma plume composed of energetic electrons, ions, and atoms in various excited states. This plasma expands away from the target due to collisions among the ejected species and propagates toward the substrate. The substrate, mounted on a heated stage, can be maintained at elevated temperatures, up to 900°C, to facilitate epitaxial growth and improve film crystallinity. A key advantage of PLD is its ability to preserve the stoichiometry of the target material in the deposited film, provided that the laser fluence is sufficiently high. Under these conditions, the vaporization process occurs uniformly across different atomic species, preventing elemental loss that would otherwise occur due to their variation in vapor pressure. Additionally, the deposition environment can be precisely controlled by introducing reactive gases at varying partial pressures, allowing for tailored chemical reactions between the ablated material and the surrounding gas. This capability makes PLD particularly useful for synthesizing complex oxides, enabling the growth of high-quality thin films with tunable properties [88–90].

The used system by Twente Solid State Technology (TSST) can be seen in Figure 3.1b. The connected laser is a 50 W KrF excimer laser with 25 ns pulse length and a wavelength of 248 nm.

Growth Modes and Reflection High-Energy Electron Diffraction

During thin film growth, the surface morphology and growth dynamics can be monitored *in-situ* using reflection high-energy electron diffraction (RHEED).

In this method, an electron gun (tungsten filament with 1.4 A current) emits a beam of high-energy electrons, here accelerated with 25 keV, at a grazing incidence angle toward the substrate surface. Due to the shallow angle of incidence, part of the electron beam reaches a phosphor screen directly, while the other part undergoes diffraction at the crystal lattice of the growing thin film. The

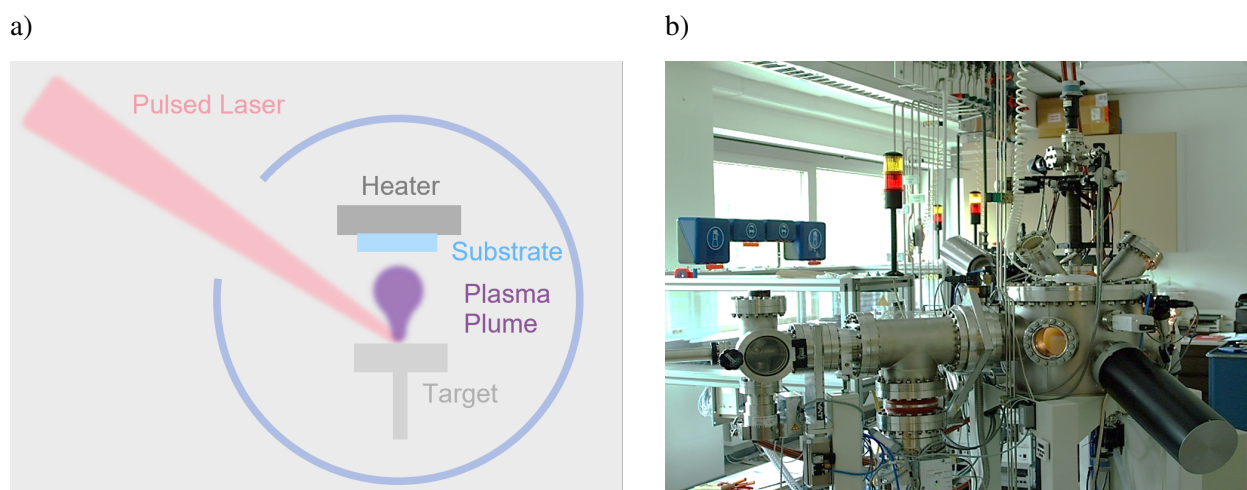


Figure 3.1: a) Schematic PLD chamber. b) Photo of the TSST PLD system utilized in this work.

resulting diffraction pattern, displayed on the phosphor screen and recorded by a camera, is highly sensitive to surface features on the sample, making RHEED a valuable tool for studying film growth mechanisms. An important feature of RHEED analysis is the specular reflection, where a fraction of the electron beam is directly reflected off the film surface without undergoing diffraction. By tracking the intensity of this specular spot or other diffraction spots, one can assess the roughness of the growing thin film. Oscillations in the intensity of the specular spot demonstrate layer-by-layer growth, a measure of high quality thin film growth. The intensity reaches a maximum when a full unit cell layer is completed, resulting in a smooth surface. As deposition continues, step-edges form, increasing surface roughness and causing a drop in intensity. The lowest intensity corresponds to a maximum step density, indicating a half-formed layer. As the gaps between steps are filled, the surface smooths out again, and the intensity rises. The periodicity of these oscillations corresponds to the growth of one unit cell per oscillation, allowing precise tracking of the deposition rate. An exemplary demonstration of layer-by-layer growth with its characteristic oscillations is the growth of LSMO on STO shown in Section 4. A gradual decrease in intensity, superimposed to the oscillations, can occur due to slightly imperfect growth conditions, such as the oxygen partial pressure in the chamber, which may promote a transition from layer-by-layer growth to a more three-dimensional growth mode, or extended strain as the thin film thickness increases [91, 92].

3.1.2 Sputtering

Sputter deposition is a widely used physical vapor deposition (PVD) technique that relies on plasma generation to deposit thin films onto a substrate. Extensive explanation can be found in [93–95]. The sputtering process involves bombarding the surface of a target material with high-energy argon ions, which physically vaporizes target atoms. These ejected atoms then travel through the vacuum chamber and condense on the substrate, forming a thin film. As illustrated in Figure 3.2, the target and substrate are positioned opposite each other within a vacuum system.

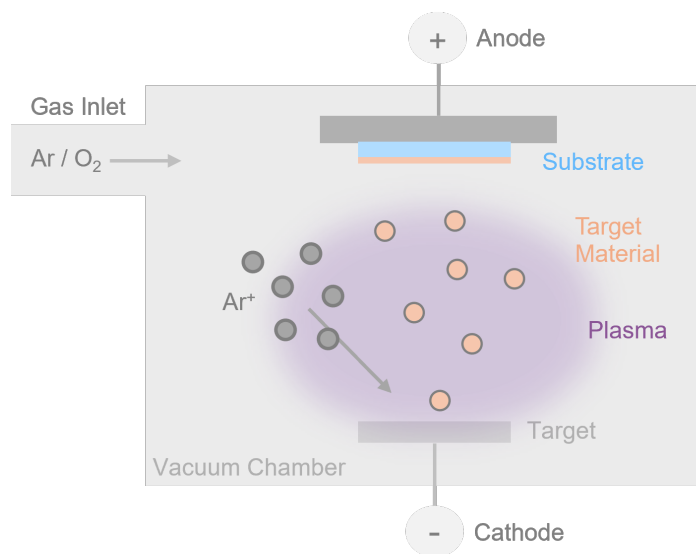


Figure 3.2: Sketch of sputter deposition. Sputter gas (Ar) and reactive gas (O₂) are led into the chamber. The target material is sputtered by Ar ions and travels towards the substrate, where it deposits a thin film. O₂ as a reactive gas enables a chemical reaction of the target material before forming the thin film. Depending on the target material a DC (conductive target) or RF (insulating target) voltage is applied between target and substrate.

To ignite a plasma, argon gas is introduced into the chamber and a high voltage is applied between the target and substrate. In the electric field, free electrons accelerate, collide with argon atoms, ionizing them and generating more free electrons in a cascading effect, thereby sustaining the plasma. The positively charged argon ions accelerate toward the negatively charged target, where their impact results in the ejection of target atoms via momentum transfer. Direct current (DC) sputtering is suitable for conductive targets, where the target serves as the cathode while the substrate acts as the anode at ground potential. However, DC sputtering is ineffective for insulating materials since charge accumulation on the target surface would hinder further ion bombardment. In such cases, radio frequency (RF) sputtering is employed. RF sputtering applies an alternating voltage to the target electrode, periodically reversing the surface potential. During the negative half-cycle, the target behaves similarly to a DC cathode, facilitating sputtering. In the positive half-cycle, incoming electrons neutralize the surface charge, allowing continuous operation.

To enhance sputtering efficiency at lower pressures, magnetron sputtering can be utilized. This technique incorporates a magnetic field near the target, confining electrons to spiral paths and increasing their interactions with the argon atoms. The increased ionization enhances plasma density, leading to higher sputtering rates with reduced gas pressure and applied voltage (not depicted here).

In addition to pure element deposition, reactive sputtering allows for the synthesis of compound films by introducing reactive gases into the chamber. This method is used when depositing oxides, nitrides, or other compounds either from elemental targets or to compensate for the loss of volatile elements when sputtering from compound targets.

3.1.3 Evaporation

Thin films of gold and platinum were fabricated using electron-beam (e-beam) evaporation, an alternative PVD technique. Deposition was carried out either through a shadow mask (see Section 3.2) to define specific patterns or covering the entire sample. In the employed setup (various manufacturers), material is evaporated by a high-energy electron beam that heats the target material until it reaches its evaporation point. The evaporated atoms travel within the vacuum chamber and condense onto the substrate, forming a thin film. Precise control over film thickness is achieved through a quartz microbalance, which monitors the deposition rate by measuring the frequency shift caused by accumulating mass. This allows for accurate regulation of the final film thickness. To ensure high-purity deposition and prevent unwanted chemical reactions, ultra-high vacuum (UHV) conditions are maintained within the chamber. This minimizes the presence of residual gases that could otherwise lead to contamination, such as oxidation of the deposited metal.

Additionally, it can be important to consider the thermal effects during deposition. Due to the high-energy e-beam heating process, substrate temperatures can reach up to 100°C, which may influence the film morphology, adhesion, and underlying material properties.

3.2 Microstructuring Techniques

Achieving different kinds of device layouts requires the selective deposition or removal of different thin films. Used techniques are briefly described in the following.

Photolithography

Ultraviolet (UV) light photolithography together with a mask aligner is used to pattern samples. Depending on the desired lithography process, an appropriate photoresist is spin-coated onto the sample. Photomasks with the desired structure are aligned with the sample or already present structures on the sample, then brought into close contact with the surface. Regions of the sample either get exposed to UV light or are covered by structures on the photomask. The used photoresist determines a *positive* or *negative* lithography process. In a *negative* process, regions exposed to the UV light harden, while covered areas can be dissolved afterwards. This process is typically followed by the deposition of a metal thin film to create simple top electrode structures. In a following *lift-off* step, the hardened photoresist is removed and with it the metal deposited onto those regions, leaving behind metal pads in the shape of the structures on the photomask. In contrary, a *positive* process leaves the exposed regions soluble and hardened photoresist remains in the shape of the photomask structures. This is often used for subsequent etching, where the photoresist protects the sample, while uncovered material is etched away.

Shadow Mask

Utilizing a shadow mask for structuring is a straight forward and time efficient process used to create simple top electrodes. A nickel mask with holes in the shape of the desired structures is fixed

on the samples with magnets, acting as a kind of stencil. The material of choice is then evaporated (Section 3.1.3) through the mask. This process is only suitable for simple structures, as no alignment is possible and the structure size is limited to $>10\ \mu\text{m}$. Further, due to a remaining distance between mask and sample, the resulting structures are less defined than with photolithography.

Ion Beam Etching

Etching is a key process used to pattern materials. Ion beam etching is a dry etching technique that utilizes plasma to remove material. The Argon plasma, generated under vacuum by an electromagnetic field, produces high-energy ions that bombard the sample surface, enabling precise material removal. Ion beam etching (Ionfab300plus from Oxford Instruments) was used in combination with a *positive* photolithography process for sample patterning. This physical etching approach is generally less selective than wet etching. Etching rates for each material are determined through dummy films.

3.3 Atomic Force Microscopy

Atomic force microscopy (AFM) examines a sample's topography by measuring the forces between its surface and a scanning tip. A microscopic tip, positioned at the end of a cantilever, oscillates at a predefined frequency and amplitude, driven by piezo elements. As the tip interacts with the sample, distance-dependent forces alter the cantilever oscillation amplitude and phase. A laser, reflected off the top of the cantilever onto a photodiode, detects these changes while scanning the surface. A feedback loop continuously adjusts the tip-sample distance, generating a high-resolution topographical map of the sample. A more detailed description of the technique can be found in [96]. Measurements were performed with a FlexAFM (NanosurfAG) and images were processed with the open source software *Gwyddion*.

Conductive Atomic Force Microscopy

An extension of AFM that additionally measures the local current flow through the sample, is conductive atomic force microscopy (CAFM). The topography of the sample surface is measured similarly to AFM, with the modification that, here, a conductive tip is used, in contact with the sample. Simultaneously, for the current mapping, a voltage is applied between the tip and the sample holder, and the resulting current flow through the sample or individual films is measured. In addition to the tip radius or contact area, the resolution of CAFM is also determined by the (lateral) conductivity of the sample [97, 98]. In this work, CAFM is performed with a Scienta Omicron VT-SPM at room temperature under a base pressure below 10^{-9} mbar. The sample bias is applied with a Keithley 2401, while the tip is grounded to the Omicron Matrix controller. Conductive single-crystal diamond probes, Bruker AD-2.8-SS, with tip radius <5 nm were used.

3.4 X-Ray Diffraction and Reflectometry

X-Ray Diffraction

X-ray diffraction (XRD) enables the structural characterization of crystalline materials. Since X-ray wavelengths lie in the range of below 1 nm, they can be utilised to resolve the lattice constants of a crystal by scattering at atoms and the interference of scattered waves according to Bragg's law:

$$n\lambda = 2d_{hkl}\sin(\Theta), \quad (3.1)$$

where n is an integer of the wavelength λ , d_{hkl} is the distance between two lattice planes of the crystal lattice determined by the Miller indices (hkl), and Θ is the angle between the lattice plane and the incident X-rays. The measurement is performed in the Bragg-Brentano geometry to analyse the thin films on top of a single-crystalline substrate. Data is shown as measured intensity versus 2Θ . The intensity and width of individual reflections are further indicators of the crystals' imperfection [99].

For the analysis in this work, a Bruker D8 discover is used. The machine uses an X-ray wavelength of 1.5406 Å (Cu K_α).

X-Ray Reflectometry

The thickness of thin films or multi-layers can be determined using X-ray reflectometry (XRR). In this technique, an X-ray beam is directed onto the sample in Bragg-Brentano geometry, with the incident angle ω varying from 0.2° up to 5°. At very small angles, the beam is totally reflected on the surface. Once the critical angle Θ_c is exceeded, partial transmission of the beam into the layer occurs. Within the film, the beam undergoes partial reflection at the surface, while the transmitted part continues to the next interface, with the propagation angle determined by the refractive index of the material. At the next interface between different thin films or between the film and the substrate, the beam is reflected back toward the film surface, where it undergoes further partial reflection and transmission. The superposition of these waves, coming from the sample surface, results in constructive and destructive interference, depending on the incident angle and the layer thickness d . This interference gives rise to intensity oscillations measured at $\Theta = 2\omega$. The layer thickness can then be calculated from the oscillations via:

$$d = \frac{\lambda}{2} \frac{1}{\Theta_{m+1} - \Theta_m} \quad (3.2)$$

In the case of multiple layers, the resulting intensity oscillations are a superposition of the different individual layer thicknesses. The noise level of the measurement and the intensity decay are determined by the surface roughness. It is further possible to deduce the film density from Θ_c , where in the case of multi-layer structures, only the most dense film contributes [99, 100].

Measurements are fitted using the software *GenX*.

3.5 X-Ray Photoelectron Spectroscopy

X-ray photoelectron spectroscopy (XPS) is a characterization method that relies on the element-specific binding energies of electrons within the atomic shells. The surface of a sample is irradiated with photons of known energy, and the measured kinetic energy of the emitted electrons can be directly related to the binding energies of the involved energy levels. Photoelectron emission occurs when X-rays with energy $h\nu$ interact with electrons with binding energy E_b . The binding energy in XPS is then given by:

$$E_b = h\nu - E_{\text{kin}} - \phi, \quad (3.3)$$

where E_{kin} is the kinetic energy of the emitted electron, and ϕ is the work function of the instrument. Some of these electrons travel through the solid to the surface, undergoing various scattering events. Electrons that reach the surface are emitted into the vacuum after overcoming the work function threshold. The general working principle is shown in Figure 3.3a, where the density of states $N(E)$ is schematically drawn for discrete core-levels and the continuous valence band. In this case of a metal, the valence band ends at the Fermi energy E_F , which is separated from the vacuum level E_{vac} by the work function ϕ . The related XPS spectrum (right in Figure 3.3a) displays the measured photoelectron emission intensity $I(E)$. XPS spectra are typically plotted as intensity versus binding energy. Since binding and kinetic energies have opposite signs, measurements are generally shown with the E_b scale increasing from right to left.

XPS allows for the identification of the elemental composition of a sample, since the binding energy is an element-specific property. Any change in the atom bonding state leads to changes in the spectral characteristics, such as binding energy position, peak width, and shape.

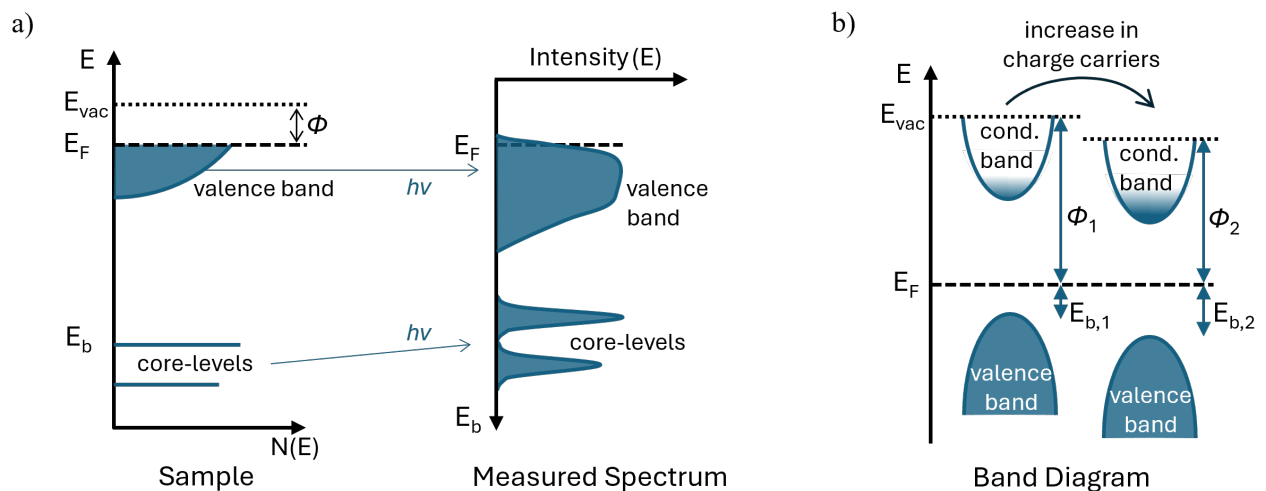


Figure 3.3: a) Schematic relation between the density of states $N(E)$ in a sample and the measured XPS spectrum $I(E)$ with the photon energy $h\nu$. The spectrum is shown over the binding energy, which is referred to E_F . b) Schematic band diagrams illustrating changes upon an increase in charge carrier concentration. E_F shifts closer to the conduction band, leading to an increase in binding energy.

The information depth of XPS is determined by the inelastic mean free path, λ_{imfp} of electrons in the material. Scattering at a length l causes an intensity reduction following:

$$I(l) = I_0 \exp\left(-\frac{l}{\lambda_{imfp}}\right) \quad (3.4)$$

with the initial intensity I_0 and reduced intensity I_l after l . λ_{imfp} generally depends on the material and E_{kin} of the electrons. At a given depth below the surface, the electron path length decreases as the take-off angle (measured from the sample surface) increases. Consequently, a larger take-off angle corresponds to a greater information depth. By adjusting the detection angle of emitted photoelectrons, angle-resolved XPS enables the generation of nondestructive depth profiles. To study buried films or interfaces, conventional lab-based XPS often lacks sufficiently intense X-rays. Higher energies, to enhance λ_{imfp} even at low angles, can be achieved with hard X-rays available at synchrotron facilities. Such experiments are referred to as HAXPES (hard X-ray photoelectron spectroscopy). Details on the working principle and analysis practices can be found in [101, 102].

XPS of (transition) metal oxides

In the case of metal oxides, the XPS peaks appear at a higher binding energy and with a different peak shape in comparison with the metal peak. The amount of the metal oxide peak shift increases with the metal valence state. Defects in metal oxides can lead to differences in the cation valence state, where the commonly occurring oxygen vacancies act as n-type doping. For sufficiently large concentrations, the metal oxide can reduce its full oxidation state to a stable state of lower oxidation. Consequently, even multiple metal oxide peaks can appear if different valence states are present. The shift in binding energy of the different valence states can be explained by the change in the effective charge potential of an atom. Namely, due to the electron transfer to the oxygen ion, the remaining core-electrons are more tightly bonded to the metal ion. This characteristic is used to analyze the bonding character and the oxidation state of species in a sample. Additionally, oxygen vacancies introduce donor states that increase the charge carrier concentration, shifting the Fermi level closer to the conduction band and with that reducing the work function ϕ as schematically shown in Figure 3.3b. In dilute concentrations, i.e., in the nearly stoichiometric case, below the detection limit of a lower valence state peak, the Fermi level is more sensitive to these donor states. This leads to detectable rigid shifts of the metal oxide peak, where a higher Fermi level due to more n-type doping via oxygen vacancies corresponds to an increase in binding energy, detectable via XPS [103].

For nonconducting samples, surface charging can also lead to a shift in peak energies. To address this, the XPS spectra can be referenced to a known metal peak, such as the Pt $4f_{7/2}$ peak (71 eV).

Measurements in this work are conducted with a *Versa Probe 5000* (Physical Electronics Inc., USA), at the GALAXIES beamline at the Soleil synchrotron, France [104] and via XPEEM experiments at the MAXPEEM beamline at MAX IV synchrotron Lund, Sweden and the Nanospectroscopy beamline at Elettra synchrotron laboratory, Trieste, Italy.

3.6 X-Ray Absorption Spectroscopy

X-ray absorption spectroscopy (XAS) is a technique used to study the electronic structure and local atomic environment of materials. It can provide insights into oxidation states, coordination geometry, and interatomic distances.

When X-rays pass through a material, they interact with core electrons. If an X-ray photon has sufficient energy, it can excite an electron from an inner atomic shell into an unoccupied state, where quantum mechanical selection rules determine the possible excited states. This creates a core hole, leaving the atom in an unstable, excited state. The atom returns to a stable state through fluorescence emission and the Auger effect. In fluorescence, an electron from a higher energy shell fills the core hole, releasing a secondary X-ray photon, while in the Auger process, the released energy is transferred to another electron, which is then ejected from the atom. Both can be detected as electron yield and related to the absorption probability, leading to characteristic features depending on the photon energy. The absorption of X-rays is highly energy-dependent, exhibiting sharp increases at element-specific photon energies known as absorption edges. These edges correspond to the ionization energy of core electrons and provide information about the electronic structure of materials. Shifts and intensity changes can therefore be related to, for example, valence changes. The naming convention refers the K- and L-edge to the $1s$ and $2s$ or $2p$ core level, respectively [105, 106].

Oxygen K-edge

The O K-edge spectrum provides information on the density of states of the unoccupied conduction band states together with the O $2p$ - metal d hybridization by exciting an oxygen core electron by XAS. In HZO, the conduction band is made up of metal d states, split into e_g and t_{2g} states. Changes in the local structure, such as the oxygen orbitals, result in changes in the electronic structure that are reflected in the O K-edge. Possible origins of such changes in the spectra are the loss of oxygen and the related doping, leading to shifts of the absorption edge to lower energies and a reduced intensity in the peaks associated with the lower states of the metal d band. A change in the local structure can further cause broadening or splitting of peaks, such as a coordination change of a transition between different phases might result in altered crystal field splitting [107–109].

3.7 Photoemission Electron Microscopy

Photoemission electron microscopy (PEEM) is used for *in-situ* surface analysis with high lateral resolution, generating an image based on local variations in work function and electron yield. It is based on the detection of photoelectrons and secondary electrons, emitted due to electromagnetic irradiation, such as UV light or X-rays (XPEEM). Figure 3.4 illustrates the electron path in a PEEM setup schematically. The sample is placed perpendicular to the lens system. The electrons, leaving the sample surface, are accelerated and focused towards an objective lens by a high voltage applied (10-20 kV in this work's experiments). This ensures an increased electron yield for improved

resolution by also accepting electrons emitted from the sample at small take-off angles. After passing hemispherical energy-filters, the electrons are separated by their kinetic energy and are finally detected on a multichannel plate detector and recorded by a CCD camera.

In contrast to XPS, the spatial resolution is not limited by the photon beam size, but reaches down to nearly 10 nm, limited by the aberrations of electron lenses. Another difference is that at each kinetic energy or binding energy, an image is taken instead of an integrated intensity over the whole beam footprint, meaning that spectroscopic and microscopic information can be acquired simultaneously. The use of soft X-rays limits the escape depth of the electrons, leaving the technique highly surface sensitive. Selective core-level spectra can then be extracted from different regions of interest across the imaged area. Further, it is possible to measure the minimum photon energy required to eject electrons, known as the photoemission threshold. This can be translated into locally resolved work function spectra by analyzing the rising edge of the emission intensity when plotted over $E - E_{kin}$. Image contrast generally results from differences in the elemental composition and chemical state, as well as work function differences. By adjusting the photon energy to match absorption edges, detected secondary electrons can be utilized to measure spatially resolved XAS spectra, too. Undesired topography contrast can occur in PEEM due to the strong electric field applied, which gets altered easily by features on the surface [110–112].

Details on the synchrotron beamlines and experimental setups for XPEEM used in this work can be found in [113] and [114].

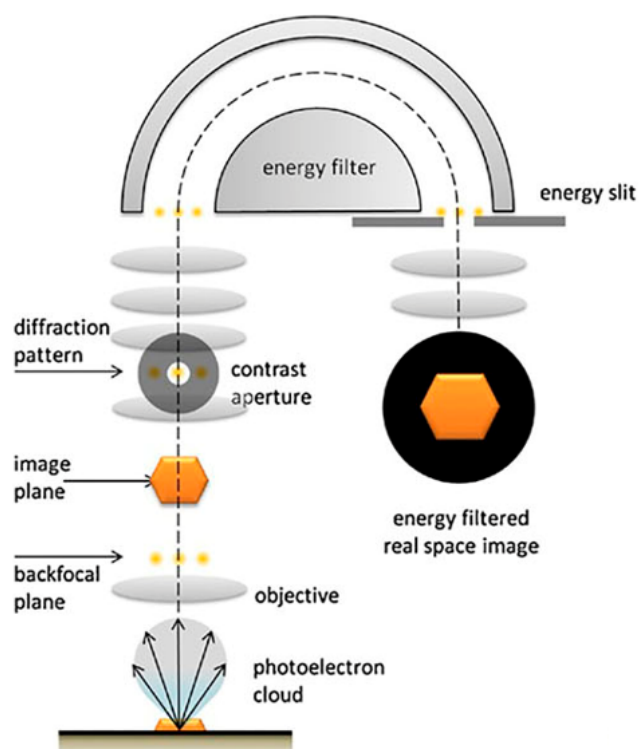


Figure 3.4: Schematic PEEM setup with electron optics configuration for real space imaging. Electrons emitted under a wide range of angles are accelerated towards and through a lens system and energy-filtered by a hemispherical analyzer, obtaining a spatially resolved spectrum. Adapted with permission from [115], Copyright 2012 Elsevier.

4 Growth of the Oxide-Heterostructures

4.1 Substrates

The SrTiO₃ substrates are purchased from SHINKOSHA Co., Ltd. with a (100) crystal orientation and a lattice parameter of 0.3905 nm. The manufacturer-specified purity is said to exceed 99.98%. In preparation for the subsequent LSMO deposition, the substrates undergo a 1:30 min etching process in hydrofluoric acid (HF) to establish a TiO₂ surface termination. To minimize etching-induced defects, they are subsequently annealed in air at 950°C for two hours, with a one-hour ramp. Finally, the substrates are cleaned by ultrasound in acetone and isopropanol, followed by mechanical cleaning with cleanroom paper soaked in isopropanol.

The RHEED diffraction pattern and AFM scan of an exemplary STO substrate are shown in Figure 4.1c and 4.2a, respectively.

4.2 (La, Sr)MnO₃

If not stated otherwise, a 20 nm La_{0.8}Sr_{0.2}MnO₃ (LSMO) thin film is deposited onto the STO substrate using pulsed laser deposition. The substrate is attached to the heater with conductive silver paste and heated to 850°C at 25°C/min under an O₂ pressure of 0.24 mbar. A one-inch LSMO target (Toshiba Manufacturing Co., Ltd.) is ablated by a KrF excimer laser (LAMBDA PHYSIK LPX 300) with a repetition rate of 5 Hz. The laser fluence on the target is adjusted to 1.5-2.1 J/cm² and the target-substrate distance is maintained at 52 mm. The deposition parameters are summarized in Table 4.1.

Substrate	Target	Laser fluence	Oxygen pressure	Temperature	Laser frequency	Cooling
STO	LSMO	1.5 - 2.1 J/cm ²	0.24 mbar	850°C	5 Hz	-
STO/LSMO	HZO	1.5 J/cm ²	0.1 mbar	850°C	2 Hz	200 mbar 10°C/min

Table 4.1: Growth parameters for the pulsed laser deposition of STO/LSMO/HZO heterostructures.

A pre-ablation procedure ensures a consistent condition of the target. For that, the whole target surface is ablated approximately four times before the actual deposition. The growth process is monitored using a RHEED system (TorrRHEED, STAIB Instruments GmbH) operating at a filament current of 1.5 A and an acceleration voltage of 25 kV. The RHEED intensities of the direct beam and several diffraction spots are displayed in Figure 4.1a. Characteristic intensity oscillations of the specular spot and both first order spots indicate layer-by-layer growth. The colors refer to the marked regions in the RHEED patterns in Figure 4.1c for the STO substrate and 4.1d for the completed LSMO growth. The deposition time for the desired film thickness is reliably calculated from the observed RHEED intensity oscillations. Figure 4.2b shows a smooth surface of an exemplary LSMO film cooled down in deposition pressure. Generally though, the LSMO deposition is directly followed by the subsequent HZO deposition. Detailed studies on growth and characterization of (La, Sr)MnO₃ can be found in [116].

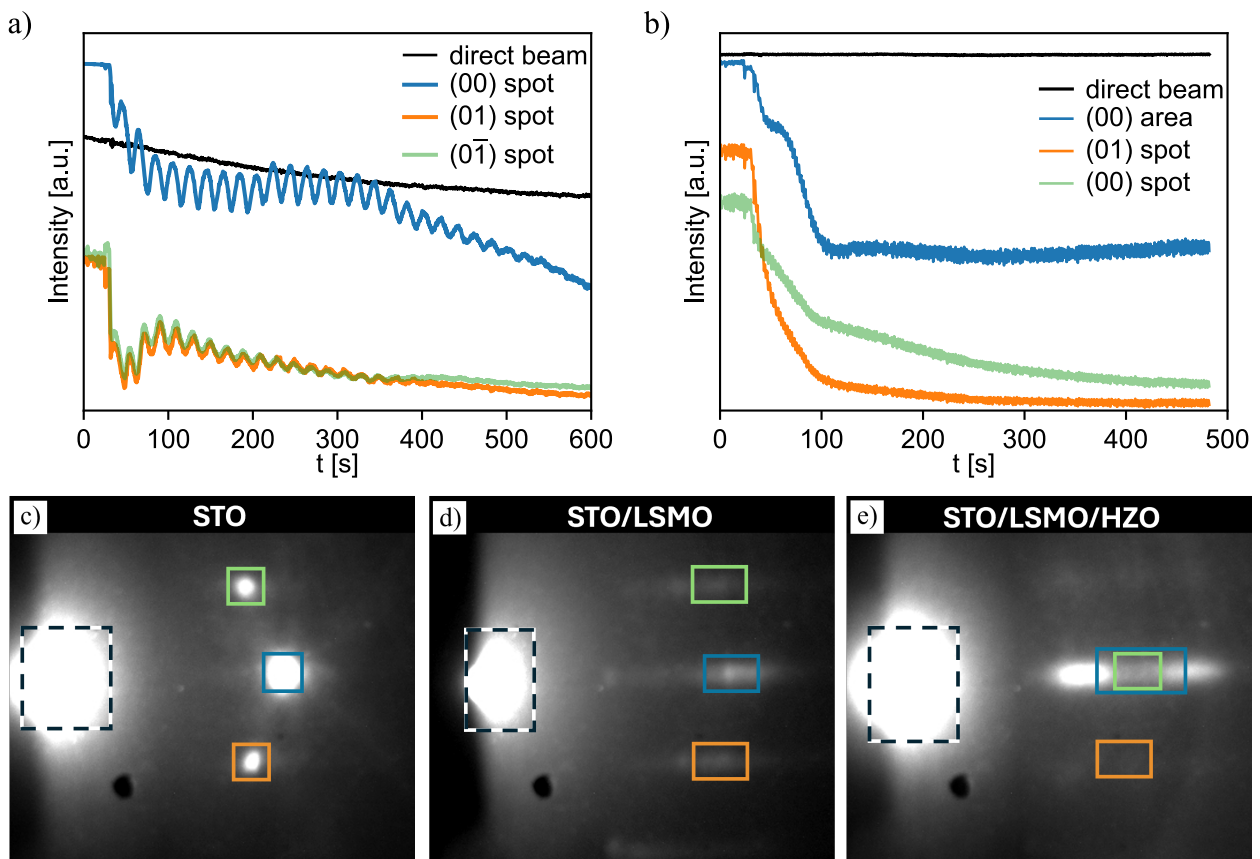


Figure 4.1: a) RHEED intensities of the LSMO growth on STO. Spots refer to the marked regions in c) and d). b) RHEED intensities of the subsequent growth of HZO on STO/LSMO. Spots refer to the marked regions in e). c) Diffraction pattern of an STO substrate with the spots for intensity recording marked. d) Diffraction pattern of 20 nm LSMO grown on STO. e) Diffraction pattern of 8 nm HZO grown on STO/LSMO. Since the HZO does not directly match the LSMO lattice, the spots and recorded regions deviate. A subtle island-growth pattern can be seen.

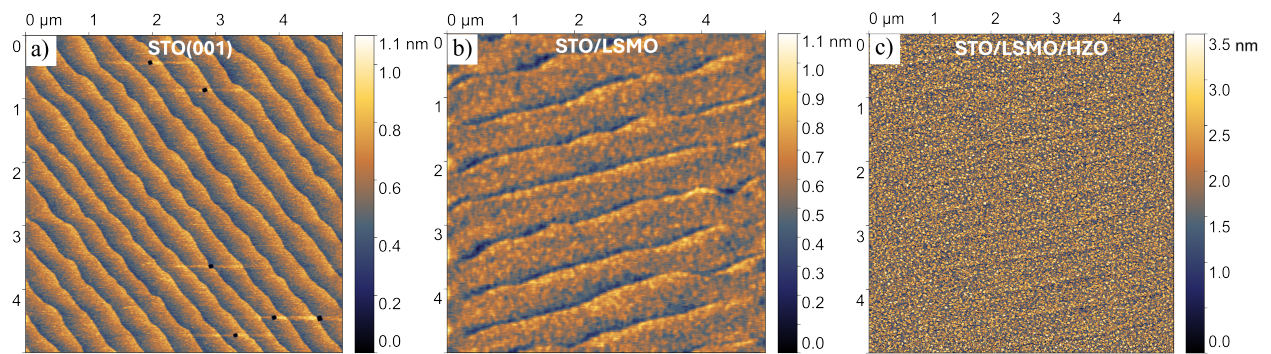


Figure 4.2: AFM scans of an exemplary STO substrate in a), 20 nm LSMO on STO in b) and 7 nm HZO on STO/LSMO in c). Step terraces of the substrate are still visible after each deposition.

4.3 $\text{Hf}_{0.5}\text{Zr}_{0.5}\text{O}_2$

Growth

The growth parameters used for the HZO deposition are derived from reports by various research groups that demonstrated ferroelectric HZO films synthesized via PLD. Lyu et al. systematically investigated the growth window of HZO using a comparable PLD system. The study included a temperature, pressure, and thickness series, though the laser fluence was not specified [117]. Within the studied temperature range of 650°C to 825°C, a continuous reduction of the monoclinic phase in favor of the orthorhombic phase was observed, with complete suppression of the monoclinic phase at temperatures of $T \geq 800^\circ\text{C}$. Between 800°C and 825°C, the crystallinity was still improving, as indicated by emerging Laue fringes. The phase evolution was accompanied by a steady increase in polarization and a decrease in leakage current across the entire temperature range.

In contrast, the deposition pressure exhibited a less pronounced effect. A well-defined orthorhombic phase was observed at oxygen pressures ≥ 0.02 mbar, and the polarization remained largely unaffected within the range of 0.05 mbar to 0.2 mbar. However, higher oxygen pressures led to an increase in leakage current, suggesting to limit the deposition pressure to ≤ 0.1 mbar. From these observations, ideal growth conditions can be estimated at temperatures $\geq 825^\circ\text{C}$ and an oxygen pressure of 0.1 mbar, although the authors consistently employed 800°C in their studies. Given the similarity in setup (thermocouple inside the heater block of the PLD), a reasonable degree of comparability between the reported parameters and the system in this work can be assumed. Further studies involving the LSMO/HZO system have reported the same parameters (0.1 mbar and 800°C in [28, 87]).

Similar conditions (0.1 mbar and 850°C) were also previously chosen for the deposition of HfO_2 on LAO/LSMO by Pinggen, using the same PLD system [118]. There, a generally higher fraction of the monoclinic phase was observed, which can be expected due to the different strain of LSMO grown on LAO substrates. Nonetheless, the results confirm the overall applicability of transferring approximate growth parameter ranges to the PLD system used in this work. In contrast to the temperature and oxygen pressure, the laser fluence is rarely reported in literature. The group of Wei

et al. used 1.1 J/cm^2 , and 1 J/cm^2 was used for the growth of HfO_2 at the PLD system of this work [28, 118]. This laser fluence had proven unsuitable for the growth of HZO in the available PLD system. It was found crucial to keep the laser fluence at 1.5 J/cm^2 or higher to prevent a significant drop of the growth rate, which was simultaneously associated with a discoloring of the target during deposition. Figure A.1 shows exemplary photos of such discoloring. The color change is assumed to result from a back-deposition of reduced target material onto the target, hence the darkening. A detailed evaluation of growth rates of HZO at varying laser fluences and temperatures can be found in Figure A.2. Finally, the growth parameters were chosen as shown in Table 4.1.

$\text{Hf}_{0.5}\text{Zr}_{0.5}\text{O}_2$ is immediately grown onto the STO/LSMO, without breaking the vacuum or cooling the sample down. The heater is kept at 850°C and the O_2 pressure is changed to 0.1 mbar. An one inch HZO target (SurfaceNet GmbH, purity 99.99%) is ablated with a laser fluence of approximately 1.5 J/cm^2 at 2 Hz.

HZO does not grow layer-by-layer on LSMO, therefore, no RHEED intensity oscillations can be utilized to monitor the growth of individual unit cells. RHEED intensity tracking of the HZO is nevertheless shown in Figure 4.1b, for the sake of completion. The green region corresponds to the former (00) spot of STO/LSMO. The specular spot first shifts until approximately 100 s of growth, then vanishes, and two different spots appear, causing an overall monotonous intensity drop. The blue region corresponds to a larger area around the former (00) spot, therefore, also capturing the emergence of the two new spots related to the HZO for $>100 \text{ s}$. Expectedly, the former (01) spot in orange vanishes rapidly. The initial shift of the specular spot aligns with the growth of several monolayers of highly strained tetragonal HZO at the interface, which has been found before in epitaxial HZO and ZrO_2 [28, 119]. Afterwards, it changes to the moderately strained growth that is retained for all thicknesses investigated in this work, resembled by the emergence of two distinguished spots in Figure 4.1e. The final RHEED diffraction pattern of HZO shows a weak island-growth related pattern, which can be expected from the non-ideal lattice matching of LSMO and HZO. The resulting HZO film is nevertheless smooth, still reproducing the step terraces of the STO substrate (Figure 4.2c).

The deposition time for HZO is estimated from the measured thickness of afore-grown films.

Börger investigated the lattice constant of $\text{La}_{0.8}\text{Sr}_{0.2}\text{MnO}_3$ under different oxygen treatment, finding that cooling of the sample in an oxidizing environment can increase the amount of oxygen that is incorporated, reducing the oxygen vacancies generated during growth [116]. Considering oxygen vacancies as a source of leakage current in the system and therefore detrimental to the ferroelectric performance of devices, following the findings on LSMO, the final STO/LSMO/HZO layer stack is cooled down in 200 mbar O_2 pressure at 10°C/min .

Characterization of the final heterostructure

HfO_2 can exhibit a variety of different phases, depending on growth conditions and doping (see Section 2.4). To some extent, the different possible phases can be identified via XRD. Figure 4.3a

shows diffractograms of the STO/LSMO (20 nm) /HZO system with various HZO thicknesses, ranging from 3-12 nm. The main peak originating from the HZO thin film is located at approximately 30° , which is slightly lower than the reported orthorhombic phase (111) peak around 30.4° or the tetragonal (110) peak around 30.8° [22, 120]. This demonstrates a compressive in-plane strain imposed by the LSMO layer for all HZO thicknesses. The position of the presumable orthorhombic peak shifts slightly to smaller angles with thinner films, an indication of a more pronounced strain, or the emergence of a rhombohedral distortion in the HZO for ≤ 5 nm HZO thickness, as has been observed first by Wei et al. [28]. The r-phase is found to stabilize under strained, oxygen-deficient conditions, predominantly for ultra-thin films [28, 121, 122]. The oxidizing conditions during cooling of the samples can be assumed to suppress the rhombohedral phase to some extent. Nevertheless, without further clarification, e.g., via pole figure measurements, the presence of a rhombohedral phase remains possible. For approximately ≥ 9 nm HZO, a small monoclinic phase fraction emerges, becoming more pronounced with thicker films.

Figure 4.3b shows exemplary XRR measurements of the 12 nm and 5 nm thick films. The superimposed oscillations resulting from 20 nm LSMO and the HZO film can be clearly told apart and are utilized for accurate thickness determination.

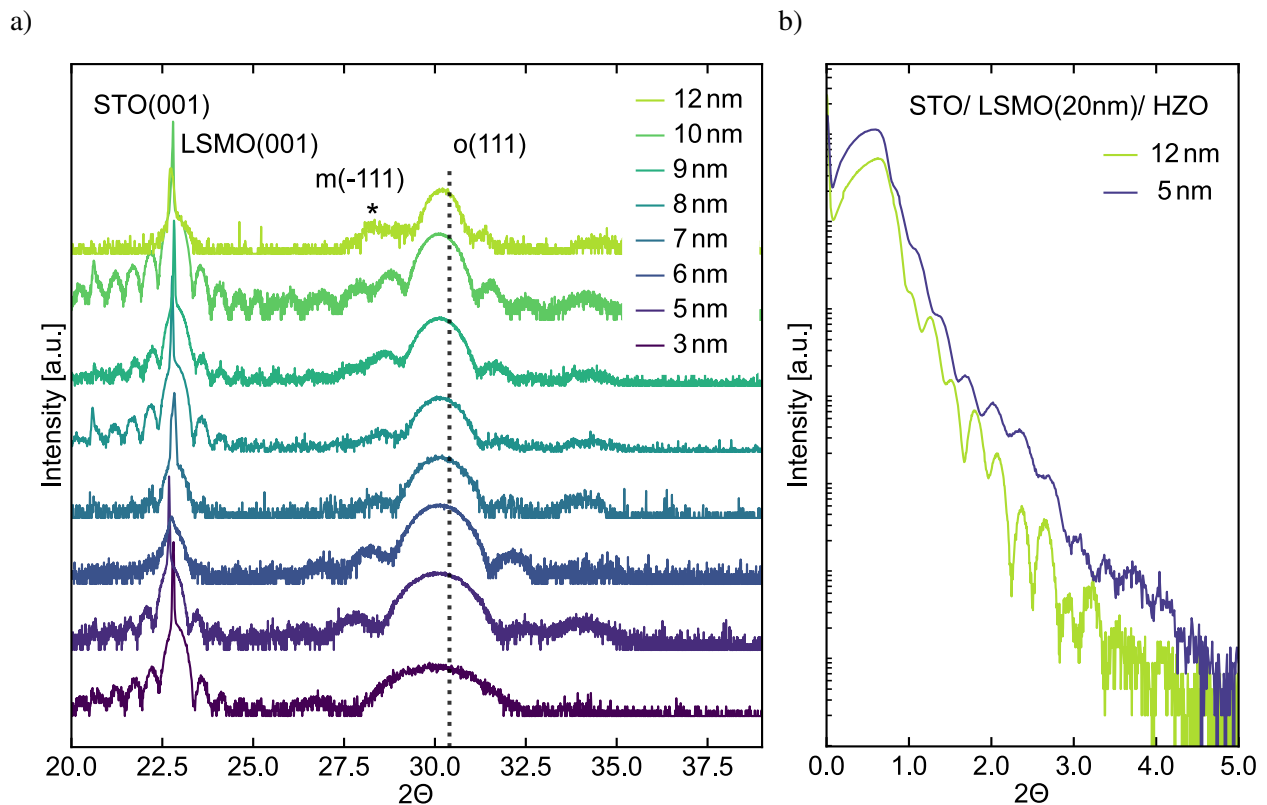


Figure 4.3: a) XRD patterns of the STO/LSMO/HZO system with varying HZO thicknesses, ranging from 12 nm to 3 nm. The predominant orthorhombic phase peak shifts to smaller angles with decreasing thickness. A monoclinic peak emerges for ≥ 9 nm thick HZO films. b) Exemplary XRR measurement of the heterostructure with 12 nm and 5 nm HZO films.

The LSMO/HZO interface has been found an important contributor to the crystallographic and electrical characteristics of the material system (see Section 2.4). Within the scope of this work, the oxygen vacancy concentration and their redistribution is of crucial importance. Following that, one notices that HfO_2 and ZrO_2 have lower formation energies than MnO when considering the standard free energy of the oxidation reactions [123]. To investigate how this impacts the LSMO when capped with HZO, a 3 nm thin HZO layer is grown onto an LSMO film to ensure a sufficient information depth from the underlying LSMO film for XPS characterization. From Figure 4.4, a valence shift of the $\text{Mn } 2p$ core level towards lower binding energies can be identified when LSMO is capped with HZO. This behavior resembles an increase of Mn^{3+} (or decrease in Mn^{4+}), which can be interpreted as an oxygen migration from the LSMO into the HZO. Under equilibrium conditions, the HZO is consequently reducing the LSMO, giving rise to oxygen vacancies stored in the LSMO layer. For the usually thicker HZO films of this work (6-10 nm), a similar or more pronounced effect on the LSMO can be expected.

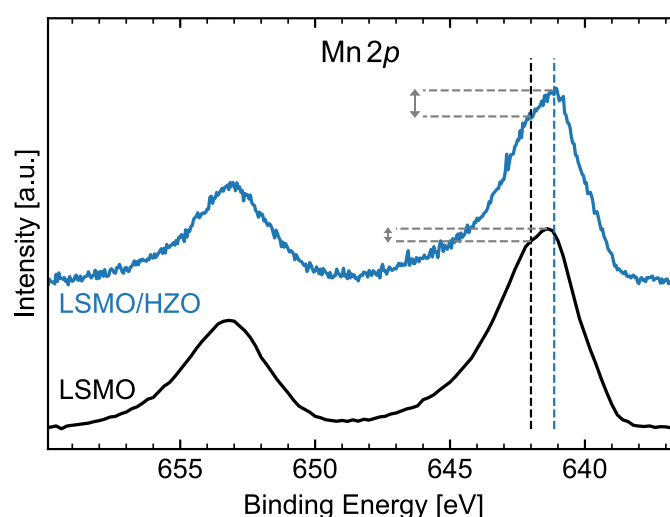


Figure 4.4: X-ray spectroscopy $\text{Mn } 2p$ doublet spectra collected with (blue) and without HZO (black) on STO/LSMO. The vertical lines highlight a right-shift of the peak maximum and the horizontal lines an intensity reduction at the left edge of the $2p_{3/2}$ peak with HZO deposited on LSMO.

Conductive atomic force microscopy (CAFM) is utilized to analyse inherent conductivity differences in the STO/LSMO/HZO system. The CAFM measurements in this work were performed by Yen-Po Liu. The tool is operated at a base pressure below 10^{-9} mbar with the sample biased, while the tip is grounded. The force set point between the cantilever and the sample surface is 1.3 nN, and the scan speed is about 167 nm s^{-1} .

CAFM measurements of a pristine HZO surface in Figure 4.5a (topography) and 4.5c (current) reveal spots and clusters of elevated conductivity in the range of 30 nm to 100 nm. The overlay of topography and current map in Figure 4.5e and a direct comparison of the two exemplary extracted profiles demonstrate that an elevated conductivity can not be related solely to a locally reduced

thickness. The conductivity variations might result from inherent structural variations, such as o-/o-phase grain boundaries or residual paraelectric m-/o-phase boundaries that have a lowered oxygen vacancy formation energy and locally enhance conductivity [124–128].

Additionally, the domain sizes of HZO found in Section 6.1 are in a similar range. Other reported grain and domain sizes of HZO in literature are also approximately in the range of the conductivity spots and clusters [129–131].

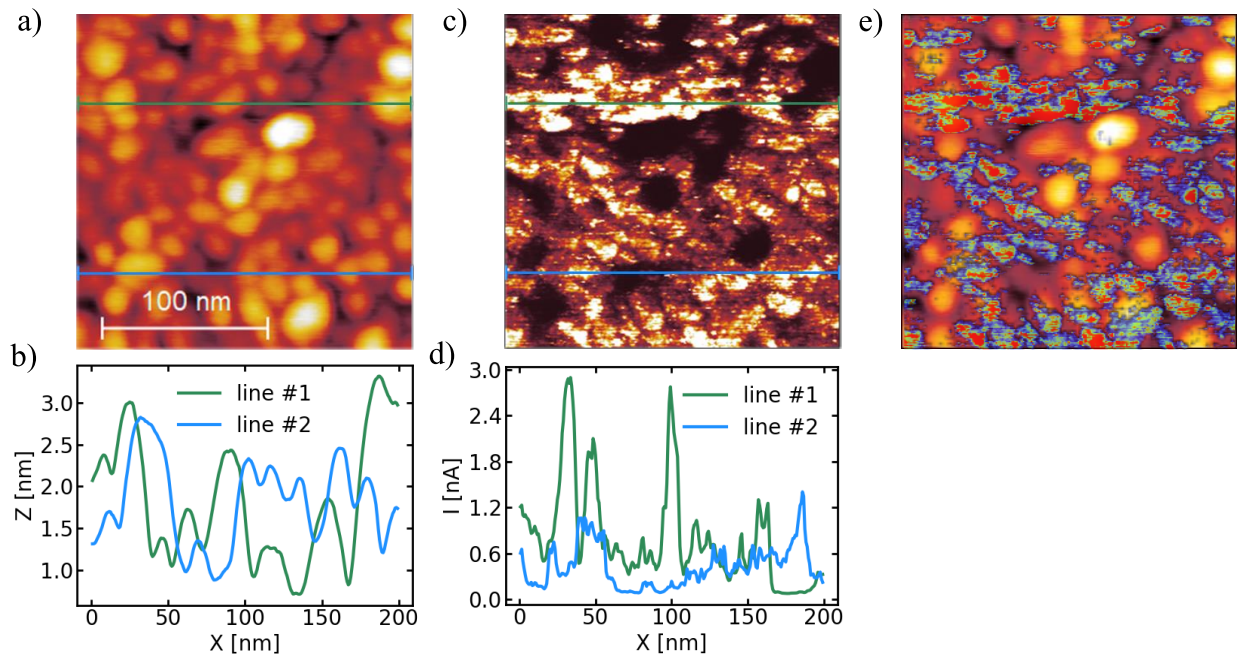


Figure 4.5: Conductive AFM measurement of HZO a) Topography of the HZO surface in a 200 nm by 200 nm region. b) Scan profiles along the green and blue lines shown in a). c) Current map acquired simultaneously with the topography, with a sample bias of +7V, electrically connected to the bottom electrode. d) Current profiles of the green and blue lines are shown in c). e) Overlay of a) and c), highlighting the conductive area corresponding to the topography.

5 Sample Preparation

Standard Capacitor Structure

For general ferroelectric or resistive characterization, Pt square top electrodes of varying sizes were deposited onto the STO/LSMO/HZO heterostructure by either sputtering together with a lift-off process or by evaporation through a shadow mask. No significant difference was identified between the two deposition methods. The LSMO served as a common bottom electrode and was contacted via a scratch through all layers in the sample periphery and conductive silver paste to form a contact pad for probes.

5.1 XPEEM Experiments

The aim of XPEEM experiments is the localization and spectroscopic investigation of filaments of reduced HZO, responsible for the resistive switching. Due to the use of soft X-ray-based techniques, the information depth of acquired XPS and XAS spectra is largely restricted to the sample surface. In order to account for this, two different design approaches were chosen: A complex design enabling *operando* switching inside the chamber and a simpler design requiring devices to be set into desired states in advance, then the sample is sealed by a metal layer, which can be delaminated under UHV conditions in the XPEEM facility.

5.1.1 Graphene Electrode Samples

Devices for *operando* experiments require top electrodes with high photoelectron transparency to maximize the signal, considering that soft X-rays are used and the estimated filament size is well below 1 μm . The chosen approach is a crossbar-type structure with graphene top electrode, that has been found successful for SrTiO₃ and Ta₂O₅ based switching devices [132, 133].

Figure 5.1 shows the different processing steps, including the used photomask (mask name: *Graphene Crossbar V2*) and a schematic of the resulting structure. The processing workflow must be modified from the original design to accommodate the epitaxial growth of LSMO and HZO on the STO substrate. To address the resulting misalignment of the original alignment markers, the first step involves the creation of additional markers. These markers, depicted in Figure 5.1a, are deposited onto the sample via a negative lift-off process using Ti/Pt evaporation. The central structures of the mask can be easily avoided by covering the areas where a deposition is undesired

with aluminum foil. Subsequently, the LSMO bottom electrode and the HZO switching layer are etched to form device structures in the shape of thin fins, as illustrated in the zoom-in of Figure 5.1b. The photoresist of the positive lithography process is kept on the sample. In parallel, it is removed from a dummy sample with the same heterostructure to accurately determine the etched depth. This approach mitigates issues arising from fluctuations in the etch rate, which could otherwise lead to over- or under-filling with the insulating layer later on. During the positive lithography step used to define the device structures, a thicker photoresist wall can form at the sample edges during spin coating. This buildup poses a risk of short-circuiting multiple devices if the LSMO layer at the edges is not completely etched away. This was successfully prevented by selectively illuminating the sample edges in the same fabrication step, using additional illumination with the second mask shown in Figure 5.1b, to facilitate the photoresist removal.

The trenches created around the remaining LSMO/HZO are filled up by sputter depositing Ta_2O_5 , according to the etched depth determined with the help of the dummy sample. Finally, the photoresist is removed, lifting off the excess Ta_2O_5 . As an artifact of the sputter deposition process, so-called fences can form at the edges of the Ta_2O_5 layer, surrounding the device. Since these residues pose a risk of damaging the subsequently deposited graphene layer, their complete removal is essential. To achieve this, the fences are mechanically removed using cleanroom paper soaked in isopropanol. The thorough removal of these structures is verified via AFM.

The graphene used as a top electrode is purchased as a monolayer from *Graphenea, San Sebastian*. It comes on a copper substrate and is covered with a protective layer of polymethyl methacrylate (PMMA). The copper is etched away by placing the substrate for 2 h in a $(\text{NH}_4)_2\text{S}_2\text{O}_8$ solution (0.1 mol L^{-1}). Subsequently, the solution is replaced with purified water multiple times. The graphene and PMMA layer is left floating on the water, where it can be fetched with the sample. Careful removal of water with N_2 and annealing at 110°C for 10 min improves the graphene-sample adhesion. The PMMA layer can be easily removed by a photoresist remover (AR 600-71, Allresist GmbH) or acetone, followed by rinsing in isopropanol.

In the next processing step, shown in Figure 5.1c, the graphene top electrodes of varying width are structured using a positive lithography process. The excess graphene is etched away by using oxygen plasma (Gigabatch plasma tool, PVE TePLa America LLC.) for 120 s, at 200 sccm oxygen flow, 150 W, without faraday cage.

Finally, noble metal leads are fabricated to establish electrical contact with the graphene layer on both sides, extending to the sample edges to enable future wire bonding to sample holders. The mask design was optimized to maximize the metal-covered surface area, thereby minimizing charge accumulation during XPEEM experiments and preventing subsequent discharges that could damage the sample. The leads are patterned using a negative lithography process followed by a lift-off step. The metal stack consists of evaporated Pt (10 nm) and Au (80 nm). It is important to note that ultrasonic baths, used to facilitate lift-off, cannot be employed in this process, as they would cause severe damage to the graphene layer. Instead, an extended soaking in acetone combined with gentle wiping using a cleanroom swab is used to facilitate the lift-off. Despite these precautions, a certain amount of non-functional devices may remain due to residual metal around the device structures.

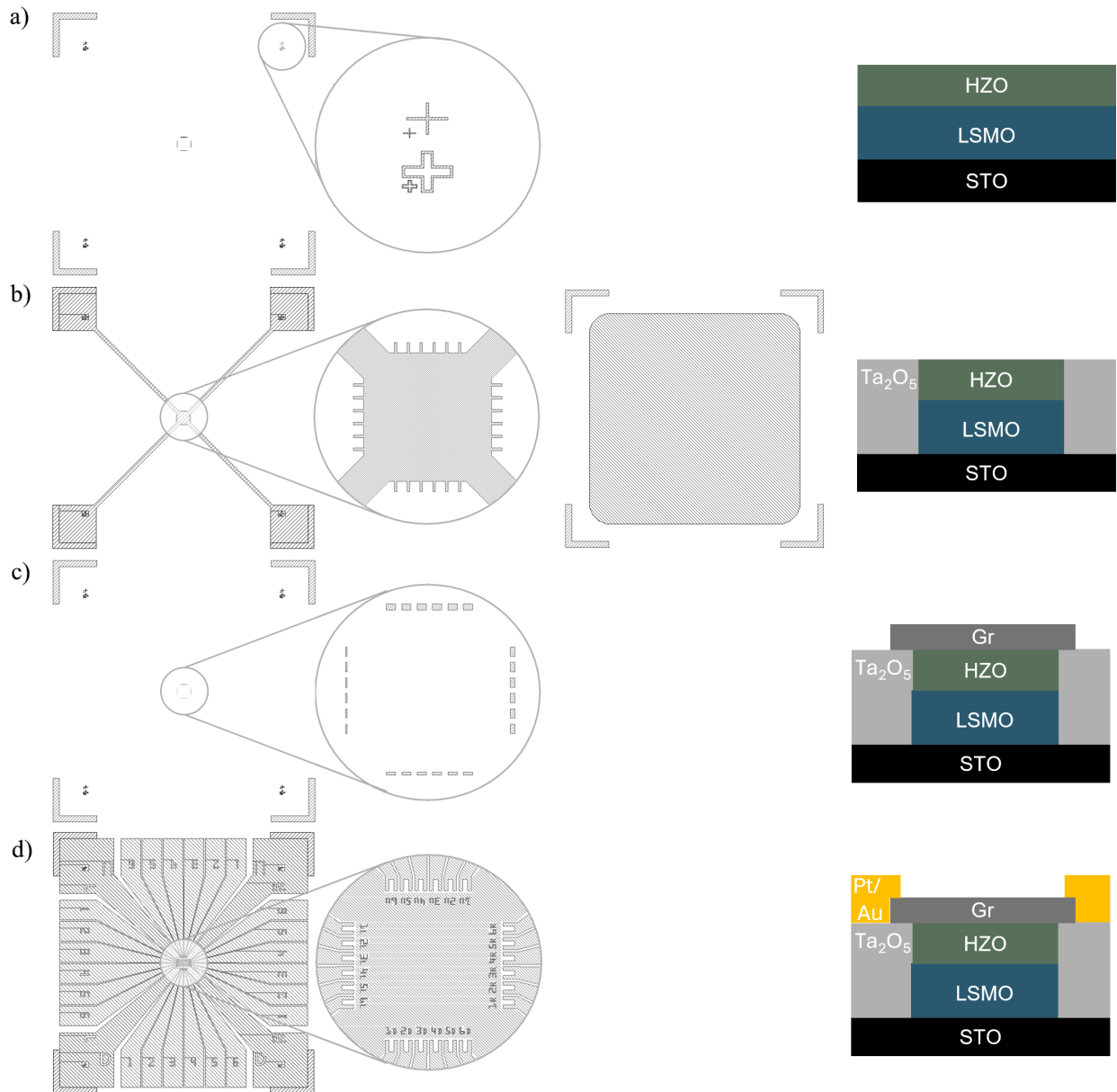


Figure 5.1: Fabrication steps and respective lithography masks for samples with graphene top electrode, used in PEEM experiments. a) Mask used for additional alignment markers and the STO/LSMO/HZO heterostructure grown by PLD. b) Mask to pattern the device structure and additional mask for enhanced edge removal of the photoresist. The photoresist is kept for etching and subsequent filling with Ta₂O₅. c) Structuring of the graphene layer into top electrodes. d) Creation of metallic contact leads from the graphene to the sample edge, including maximized coverage of the sample surface.

A close-up of the resulting device structure can be seen in the scanning electron microscopy image in Figure 5.5a. More details on the different fabrication steps, though modified, can be found in [133].

To integrate the samples with sample holders at XPEEM beamlines, several devices and the common bottom electrode (accessible via wire bonding from all corners) can be wire bonded to printable circuit boards (PCBs) available from the beamline scientists. Figure 5.2b exemplarily shows the layout used at the Nanospectroscopy beamline at Elettra, Italy, where the PCB pads are lastly connected to the sample holder with conductive silver paste.

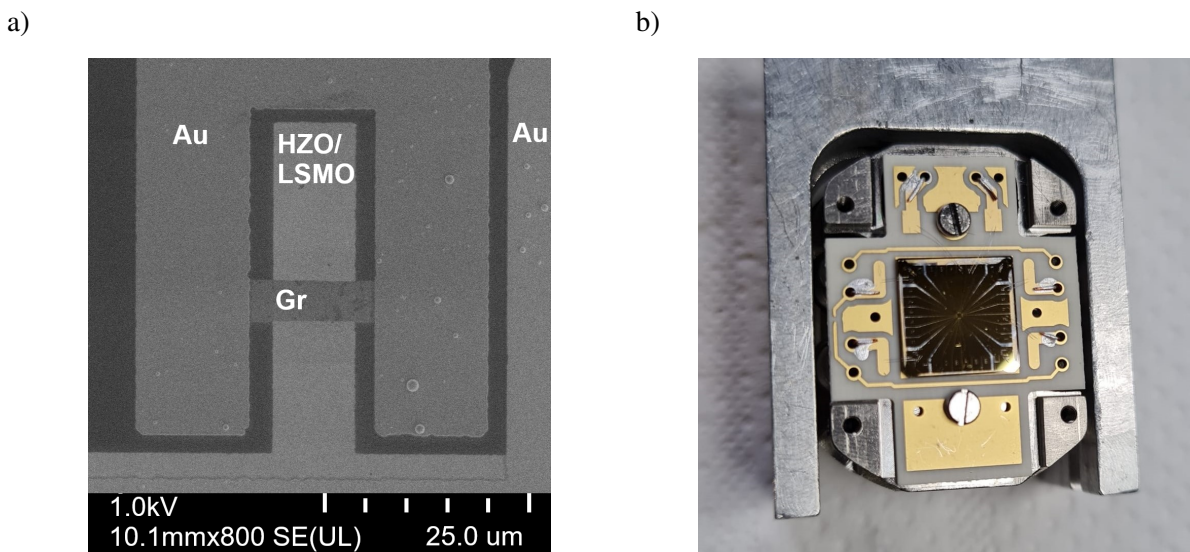


Figure 5.2: a) Scanning electron microscopy image of an exemplary device, highlighting the importance of careful alignment of the lithography masks by the small margin between different structures. The actual, switchable device is formed at the cross-section of the LSMO/HZO fin and the graphene top electrode. Adapted with permission from [134]. b) Exemplary sample electrically connected to a PCB provided by the Nanospectroscopy beamline at Elettra synchrotron, Italy (version 2024). The PCB is further electrically connected to their sample holder for *operando* XPEEM experiments.

5.1.2 Electrode Delamination Samples

A simpler, more direct approach to study the oxide surface in the low resistive state via XPEEM is by mechanically removing top electrodes under UHV conditions. This has the advantage of a much faster and fail-proof fabrication by avoiding a graphene top electrode, and the device geometry can resemble typical capacitor structures.

The STO/LSMO/HZO system (see Section 4) is covered with metal top electrodes via evaporation of about 30 nm Au, utilizing a shadow mask (see Sections 3.1.3 and 3.2). Resulting are labeled groups of nine devices, each about $12 \times 12 \mu\text{m}$ that can be individually subjected to different biasing schemes. Following the biasing process, the entire sample is coated with an additional 80 nm Au layer via evaporation. Au is selected over Pt, and evaporation is preferred over sputtering, as this

combination has been found to reduce the adhesion between the oxide layer and the top electrode, which is advantageous for future electrode delamination. A natural drawback of this approach is the increased fragility of the Au electrodes. Consequently, very careful handling and precise contact using microprobes are essential to minimize the damage.

To delaminate the Au layers, a strip of UHV-compatible copper adhesive tape is applied to the sample surface after mounting it in the designated XPEEM sample holder. Based on experience, copper tape provides optimal adhesion while its flexibility allows for convenient reshaping and the formation of suitable hooks or holes. These enable the controlled peel-off of the tape inside the UHV chamber under various orientations, using different available manipulation tools such as wobble sticks, transfer arms, or similar equipment.

The removal efficiency of the Au layer was consistently found close to 100% across all examined samples, with the exception of residuals at the edges of the tape, as visible in Figure 5.3a. This high yield was reproducible at three distinct synchrotron end-stations, each featuring different chamber geometries. More details on this and other delamination approaches can be found in [135].

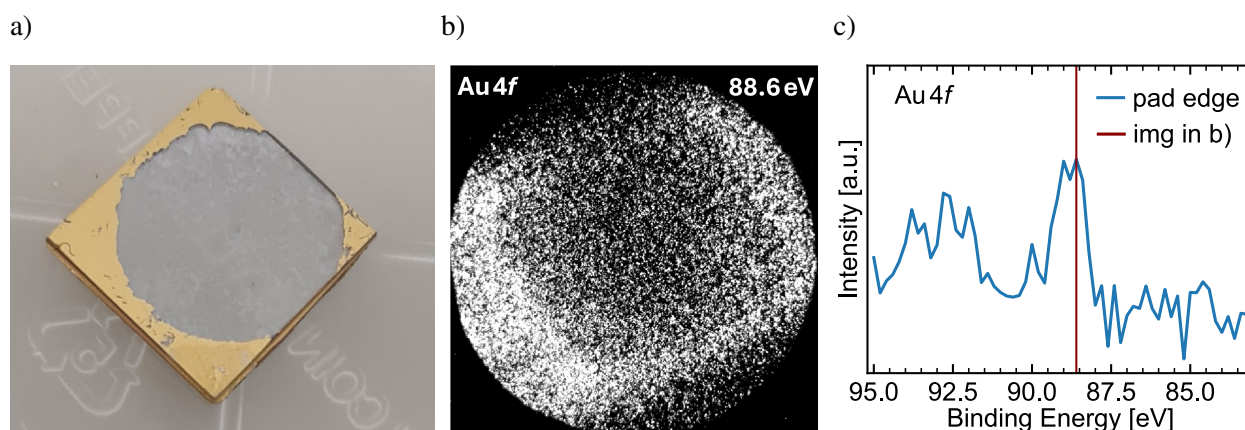


Figure 5.3: a) Photo of an exemplary sample after *in-situ* top electrode delamination using adhesive copper tape. The throughout removal of all gold in the sample center is clearly visible. b) XPEEM Au 4f image extracted at 88.6 eV. c) Au 4f spectrum extracted from the former top electrode edge.

Navigation on the laminated samples *in-situ* can be done via contrast in the workfunction measured by the onset of photoemission. In the XPEEM Au 4f image in Figure 5.3b, an intensity contrast is visible around the former top electrode area. The Au 4f spectrum extracted at the outer rim of the structure confirms weak Au residuals remaining (Figure 5.3c). This results from the diffuse deposition profile of Au evaporation through a shadow mask, which might result in significantly improved adhesion of ultra-thin Au at the outer edge of the electrodes and their labels. Further contrast in the workfunction can result from the different exposure to ambient conditions between the Au-covered and uncovered regions during biasing.

5.2 HAXPES Experiments

During HAXPES measurements, the goal is to investigate electro-chemical changes due to ferroelectric switching. With the use of hard X-rays, the significantly larger information depth allows to probe buried interfaces. At the same time, the spatial resolution of XPEEM cannot be matched, leaving the technique suitable for non-localized mechanisms like ferroelectric switching. For this, larger device sizes compared to XPEEM are beneficial to increase the area subject to the polarization change to match the size of the X-ray footprint of the GALXIES endstation at the Soleil synchrotron, France.

5.2.1 *Operando* Samples

Operando samples are the preferred choice when it comes to comparability of results. By measuring the same device in different states, device-to-device variability can be eliminated. Further, by immediate switching before the measurement, possible relaxation effects or ion migration due to the depolarizing field inside a ferroelectric can be minimized as much as possible. The design of *operando* samples requires more complex fabrication steps than simple capacitor structures to ensure no parasitic signal contributions from regions outside the device and to allow an electrical connection from the device to the periphery of the sample and to the sample holder.

LSMO and HZO were grown on STO via pulsed laser deposition, as described in Section 4. Then, a very thin platinum layer of about 2.5 nm is evaporated on the whole sample. This layer will serve as a top electrode, ensuring a full coverage of the future device while minimizing the loss of generated photoelectrons due to inelastic scattering. Figure 5.4 illustrates the following fabrication steps and the related lithography masks (mask name: *Solei2015 OxideCrossBar Freitag*).

First, a horizontal and vertical line of individual rectangular devices of $190 \times 50 \mu\text{m}$ are created by a positive lithography process and ion beam etching of the Pt and HZO layer. Next, the created devices are covered again in a positive process with slightly smaller rectangles, to ensure that the subsequently sputtered Ta_2O_5 fully covers the etch edge after lift-off (Figure 5.4b). Lastly, contact leads of platinum and gold are created by a negative lithography process, metal evaporation and lift-off. The combination of a thin layer of platinum together with a thicker gold layer ensures improved adhesion together with sufficient thickness of the contacts. The leads connect the devices from the side by a minimal overlap with the device. They extend towards the edge, where they can be electrically connected to the sample holder for *operando* HAXPES experiments. In this work, the connection of the electrodes to the sample holder was established via Au ball-wedge bonding (HB16 wire bonder, TPT wire Bonder GmbH & Co. KG). Despite careful optimization, this method still caused short cuts of many devices, since the bond could penetrate too deep through the insulating Ta_2O_5 layer. For the future, it would be advisable to etch away the bottom electrode in another lithography and ion etching step after the device creation. Here, this was omitted to simplify the fabrication process and because LSMO exhibits a relatively slow etching rate, risking the irremovable hardening of the photoresist. Nevertheless, a mask for that process step is available and shown in Figure A.3 in the appendix. The large rectangle in the bottom left in Figure 5.4b,c is used to electrically connect the bottom electrode to the sample holder.

Additional information on the mask and fabrication steps for a different material system can be found in [136].

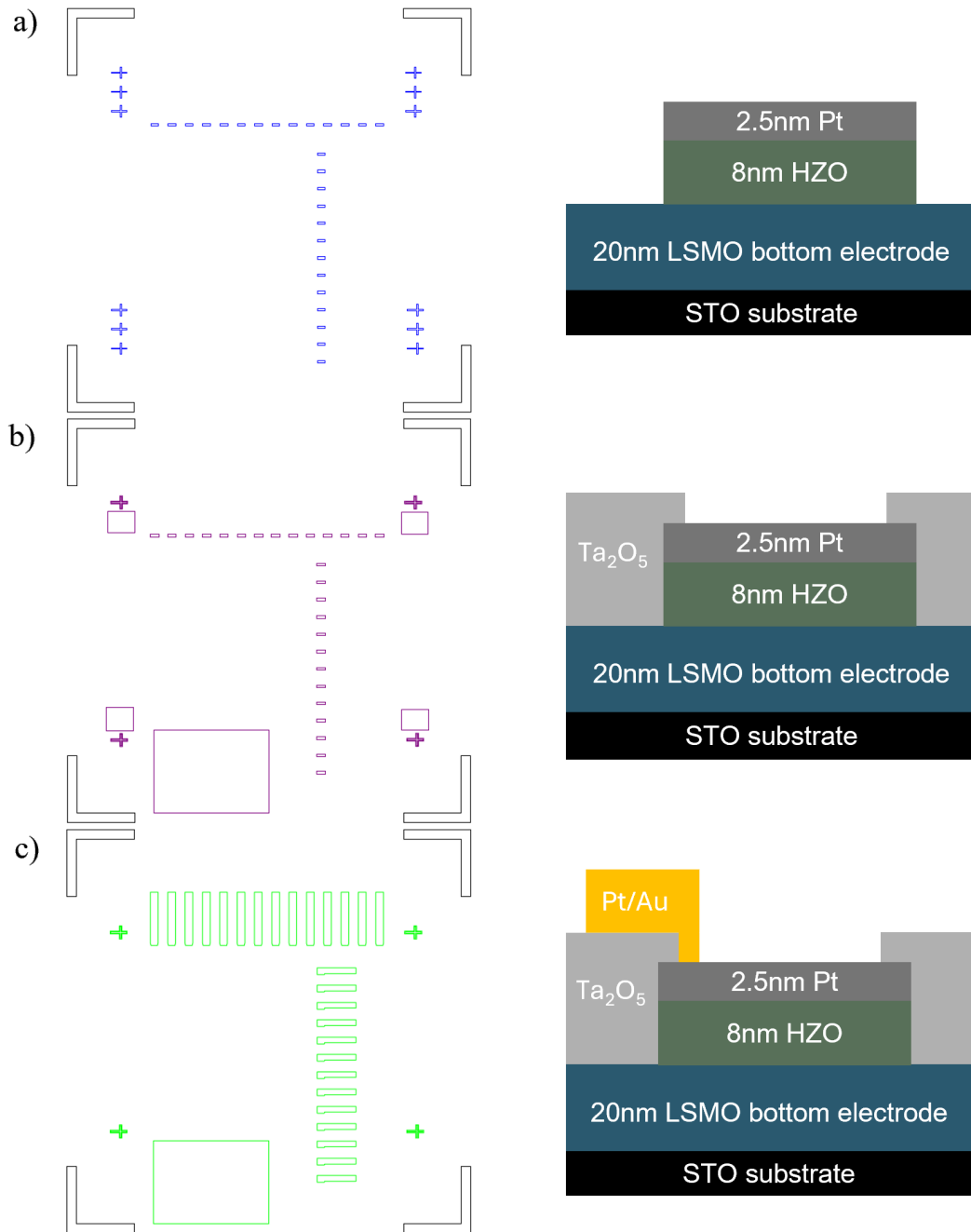


Figure 5.4: Processing steps to fabricate samples for *operando* HAXPES measurements. a) Mask for device etching and resulting cross-section. b) Mask for device protection for subsequent insulator deposition and resulting cross-section after insulator lift-off. c) Mask for the metal leads and cross-section, illustrating the desired minimal overlap at the device edge.

Figure 5.5 shows the scanning electron microscopy image of an exemplary device used for *operando* HAXPES experiments. The inner dashed rectangle shows the open device area with Pt on the surface. The outer rectangle is the complete device area, with the area covered by the intentional Ta₂O₅ overlap in addition to the uncovered area.

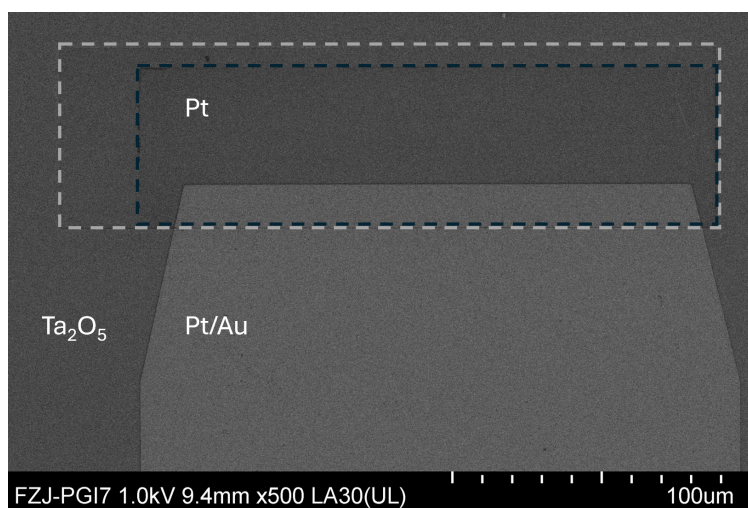


Figure 5.5: Scanning electron microscopy image of an *operando* device. The inner dashed rectangle shows the open device area with Pt on the surface. The outer rectangle is the complete device area, with the area covered by Ta₂O₅ in addition to the uncovered area. Adapted with permission from [134].

5.2.2 Array-Type Samples

Besides *operando*-type samples, a second geometry was used for HAXPES experiments. This array-type layout is designed for spectroscopic investigations with devices set to defined states *ex-situ*. The arrangement of many individual devices along separate stripes allows a large beam footprint to integrate over multiple, identically biased devices, compared to the individual devices fabricated before. This much simpler design has the advantage that the failure or short circuit of a certain amount of individual devices can be tolerated.

LSMO and HZO were grown on STO via pulsed laser deposition, as described in Section 4. A negative photolithography process and the evaporation of about 3 nm rhodium, followed by a lift-off, create individual top electrodes that minimize the photoelectron loss while ensuring decent contact when biased with common probes. The LSMO layer remains as common bottom electrode and can be contacted via wire bonding at the sample edges. Figure 5.6 shows the resulting structures of seven stripes, where each consists of 1152 individual $50 \times 50 \mu\text{m}$ devices (mask name: *Maske-Spektroskopie*). To set sufficient devices in defined states, the stripes are separated into the top and bottom half to apply different electrical treatment. The biasing is automated via an automatic probe station (MPI TS2000 probe system equipped with a Keithley 4200A SCS, 4225-PMU and two 4225-RPMs), which allows applying defined pulse sequences at high frequencies and stepping through individual devices automatically.

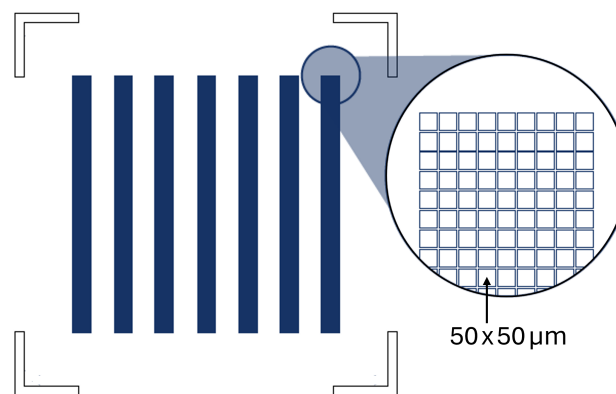


Figure 5.6: Layout of the array-type samples, consisting of several stripes of many individual $50 \times 50 \mu\text{m}$ devices. Each device is individually set into a defined state. HAXPES measurements are performed with the beam footprint covering extended area of devices, set to the same state. Adapted from [136].

6 Electrical Characterization

Parts of this chapter have previously been published in:

J. Knabe, F. Berg, K. T. Goss, U. Boettger, and R. Dittmann. “Dual-Mode Operation of Epitaxial $\text{Hf}_{0.5}\text{Zr}_{0.5}\text{O}_2$: Ferroelectric and Filamentary-Type Resistive Switching”. *physica status solidi (a)* 221.22 (2023), p. 2300409.

6.1 Ferroelectricity

Device structures of epitaxial $\text{Hf}_{0.5}\text{Zr}_{0.5}\text{O}_2$ on $\text{La}_{0.8}\text{Sr}_{0.2}\text{MnO}_3$ (20 nm) are prepared on SrTiO_3 substrates (see Section 4). The ferroelectricity of the HZO is verified through dynamic hysteresis measurements when applicable. Polarization evolution with field cycling is shown in Figure 6.1a. At the three different measurements, various characteristics can be demonstrated exemplarily. The data sets in white and blue correspond to different devices of the same 8 nm HZO sample, while the green data is measured on a 7 nm HZO sample. Within extracted hysteresis loops along the field cycling duration (Figure 6.1b,c), distinct variations that can be observed, are the magnitude of the initial leakage current (LC) and its evolution with field cycling. Further, the prominence of the ferroelectric switching current peak and with that the P_r evolution upon field cycling. Lastly, the fatigue behavior under continuous field cycling is examined, highlighting both the onset and nature of the degradation in ferroelectric switching performance.

First, the different characteristics regarding LC are discussed. The initial LC becomes obvious from the overestimated polarization (blue), or the connected current-voltage (I-V) measurement in Figure 6.1b (white) and 6.1c (green) for 10^0 cycles, with an elevated current tail at voltages above the coercive voltage. In functioning devices, the LC drops upon field cycling, which can be identified by the suppressed current tail at e.g. 10^4 and 10^1 cycles in Figure 6.1b and 6.1c, respectively. The resulting P-V loops show a pronounced hysteresis that allows for accurate P_r determination of here 15-20 $\mu\text{C cm}^{-2}$. The I-V and P-V characteristics corresponding to the blue field cycling data are not shown, as a persistent elevated leakage current (LC) is present throughout the measurement sequence. Although a reduction in LC is implied by the observed decrease in

P_r , the LC remains at a comparatively high level during the entire cycling process. With the onset of fatigue, the LC increases again, occurring rapidly for the blue dataset and more gradually for the white. This behavior identifies LC increase as the dominating degradation mechanism in these devices. Notable, after 10^7 cycles, the LC magnitude in white is comparable to its first cycle. The green measurement exhibits a consistently low LC throughout continuous field cycling.

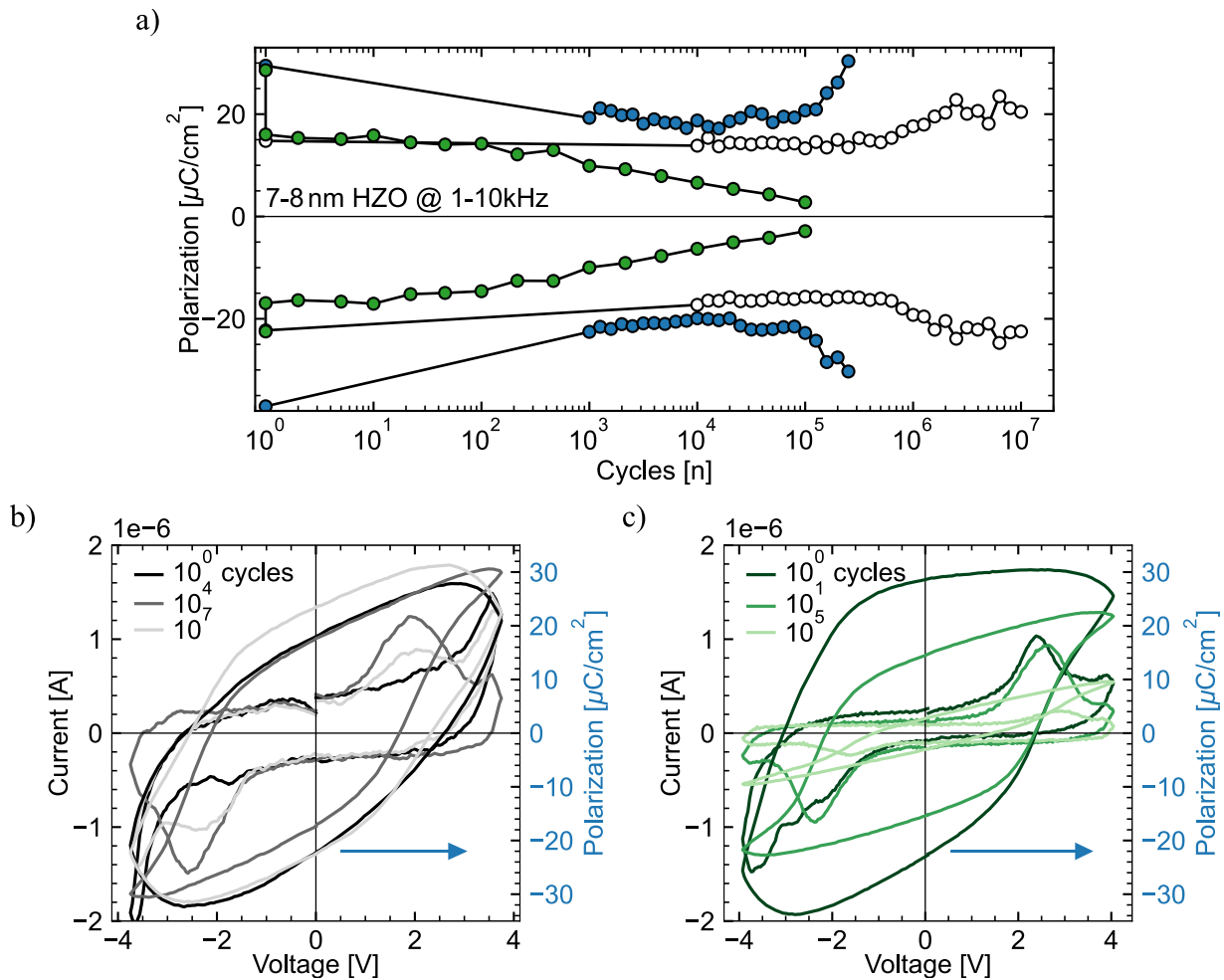


Figure 6.1: a) Different exemplary polarization evolution and fatigue behavior for continuous field cycling. White and blue are different devices on the same nm HZO sample, green is measured on a 7 nm HZO sample. White is recorded at 10 kHz, all other measurements are performed at 1 kHz. b) From the white data extracted I-V and P-V loops. c) From green data extracted I-V and P-V loops. To improve the data representation, noise was removed by smoothing all I-V measurements.

The evolution of the true ferroelectric switching, disregarding the LC, can be evaluated from the switching peak in the I-V loops. A key difference between the two exemplary samples here is that in green there is already a ferroelectric response visible in the very first cycle, while in white the I-V loop consists of only LC. In both cases, the switching becomes more pronounced after the first cycle, thus resulting in an increase of P_r . A decrease in the switching current upon fatigue is evident

for both samples, with only the green device demonstrating a closed P-V loop. The magnitude of P_r reduction seems significantly more severe for green ($15 \mu\text{C cm}^{-2}$ down to $< 5 \mu\text{C cm}^{-2}$). This can be partly assigned to the simultaneously arising LC for white that creates the impression of a higher P_r . Nevertheless, the gradual closure of the hysteresis loop is the predominant degradation mechanism for the green sample.

Overall, it can be concluded that the rise of parasitic leakage current or the reduction in polarization are the predominant factors influencing fatigue behavior. The magnitude of LC may vary between samples and devices.

Finally, it should be noted that the field cycling in white was recorded at a higher frequency of 10 kHz. This puts the cycling endurance of $< 10^7$ into perspective. Nonetheless, even when correcting the endurance by one order of magnitude, to match the other measurements, an endurance of $> 10^6$ cycles at 1 kHz can be achieved in selected devices. This comparison demonstrates, how seemingly remarkable endurance values can be readily achieved through increased cycling frequency, highlighting the necessity of careful consideration when comparing endurance data across different experimental conditions.

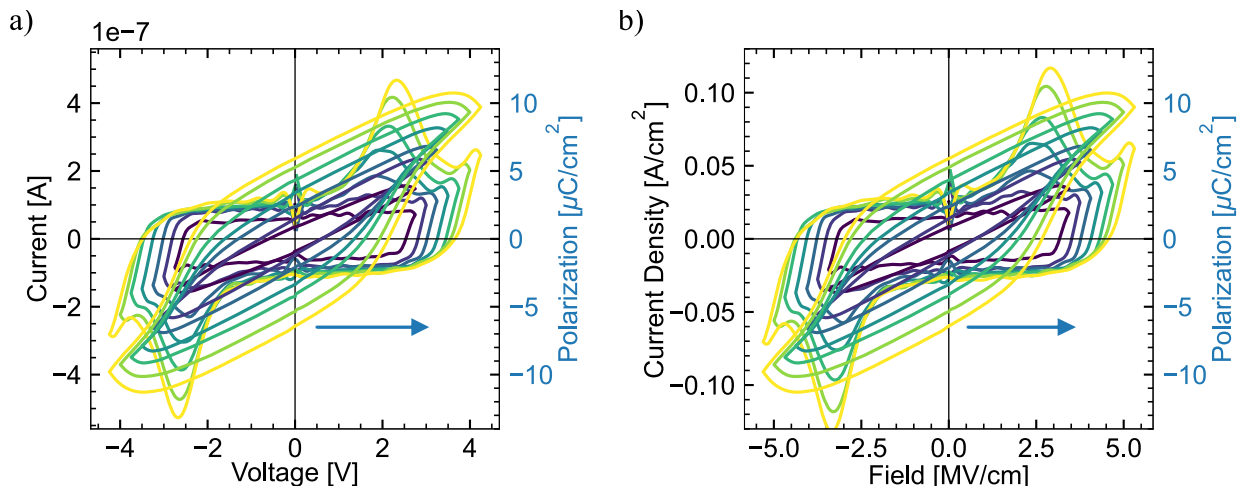


Figure 6.2: Ferroelectric switching of 8 nm HZO for increasing bias applied. As I-V and P-V loops in a) and as current density over applied field in b). Some conditioning was applied at every new bias before the displayed measurements.

Exemplary hystereses of 8 nm HZO are shown in Figure 6.2, demonstrating the evolution of polarization and coercive voltage (or coercive field) with an increasing bias applied. The corresponding switching current is displayed as an I-V curve in Figure 6.2a and as current density over the applied field in 6.2b. The hysteresis and I-V curve clearly demonstrate ferroelectricity, with a remanent polarization of up to $7-20 \mu\text{C cm}^{-2}$ and coercive voltages of $\pm 2 \text{ V}$ ($2.5 \text{ MV}/\text{cm}$) to 2.6 V ($3.4 \text{ MV}/\text{cm}$). The comparatively low P_r , relative to the previous fatigue measurements, can be attributed to the extended biasing the device is subjected to. Since the proportion of switched domains increases with the applied electric field, several hysteresis loops are measured at each voltage before acquiring the shown hysteresis curve. This process inherently introduces fatigue, potentially resulting in a

superimposed reduction in polarization. Despite this, a gradual increase in P_r , accompanied by a slight shift in E_c is still clearly noticeable, as expected due to the involvement of more and more switching domains with a higher E_c .

Piezoresponse Force Microscopy

In addition to the macroscopic characterization of ferroelectricity via current response, as shown previously, the microscopic ferroelectric behavior can be examined using piezoresponse force microscopy (PFM). This technique employs a conductive tip in contact with the sample surface within an atomic force microscopy (AFM) setup to probe the local piezoelectric response. An applied AC bias induces the converse piezoelectric effect, causing a localized mechanical deformation of the ferroelectric material. This deformation is detected through the deflection of the cantilever. Further details on the methodology can be found in [137, 138]. Measurements were performed by Oxford Instruments Asylum Research in the course of a workshop on their Vero AFM using an Au-coated tip (AD-2.8-AS, Adama Innovations).

Figure 6.3a shows the topography of a representative HZO surface, partially covered by a Pt top electrode (upper right). Figure 6.3b displays the corresponding phase response of the same region. This overview highlights an inherent preferential polarization orientation and reveals larger domain sizes beneath the Pt top electrode compared to the uncovered HZO film. Figures 6.3c and 6.3d provide magnified measurements of a Pt-covered region. A comparison between the topography and phase response, visualized by the overlay in Figure 6.3e, indicates that areas exhibiting the minority polarization coincide with regions of reduced height. However, not all lower-height areas correlate with the minority polarization direction. Figure 6.3f shows a phase profile extracted along the red line in Figure 6.3d. The measured phase contrast between majority and minority regions is approximately 180° , with minimal variation observed within individual domains. This strongly suggests that the contrast arises predominantly from out-of-plane piezoelectric responses, with negligible influence from surface topography or in-plane domain orientations. The domain sizes of the minority regions range from 20 to 150 nm.

Figures 6.3g and 6.3h present close-up views of the topography and phase response on the HZO surface. Here, the overlay of topography and phase in Figure 6.3i shows no obvious correlation between surface height and the presence of minority polarization domains. The extracted phase profile in Figure 6.3j reveals a phase difference of approximately 180° . Deviating phase differences $\leq 100^\circ$ can be attributed to very small domains where the spatial resolution limit approached. The domain sizes in this region lie within diameters of 10-50 nm.

The switching spectroscopy mode of PFM (SS-PFM) allows extracting local switching characteristics of ferroelectrics. In this mode, an AC signal is superimposed onto a series of DC voltage pulses with increasing and decreasing amplitudes up to ± 8 V. The resulting deformation amplitude and phase can be recorded either during the application of the DC bias (on-field) or in the intervals between pulses (off-field). Figure 6.4 shows the SS-PFM measurement taken on the HZO surface with off-field (Figure 6.4a and 6.4b) and on-field (Figure 6.4c and 6.4d). From the off-field response, a phase difference of 180° and coercive fields of -4 V and $+2$ V can be extracted.

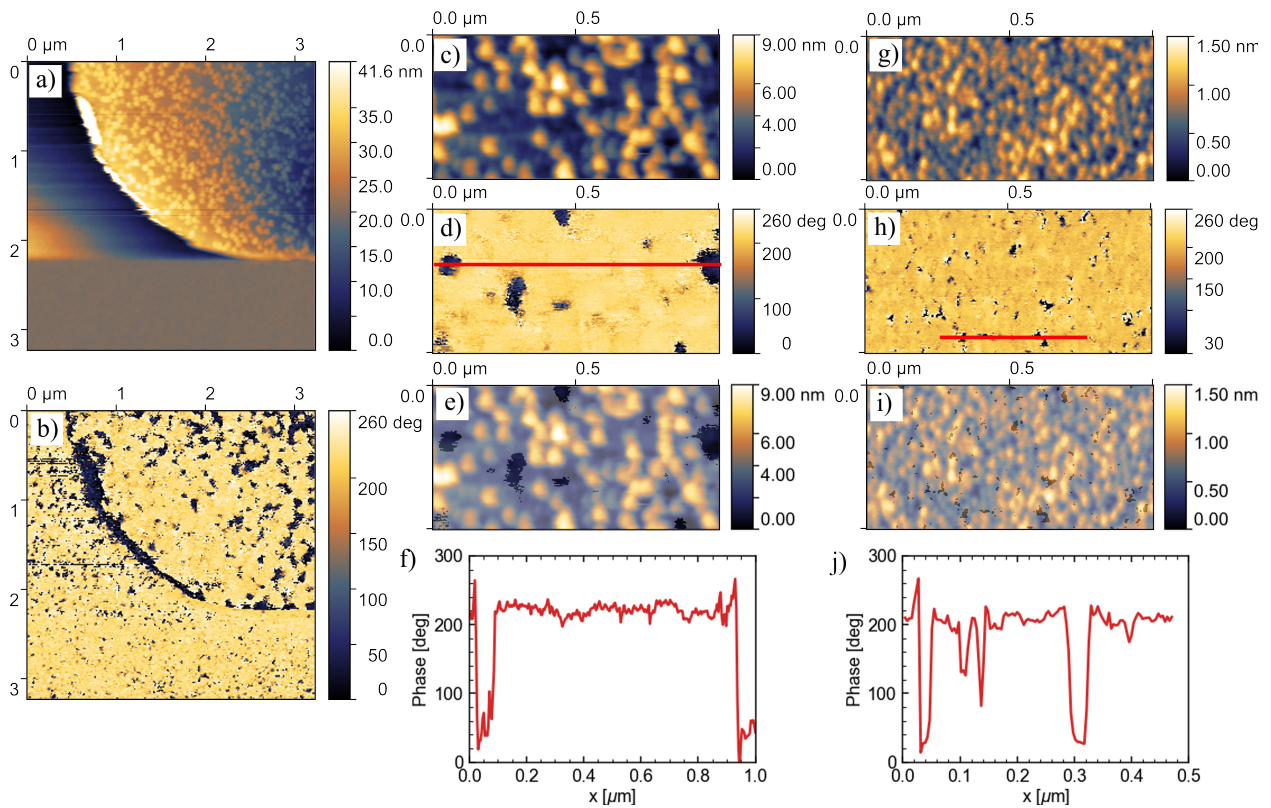


Figure 6.3: PFM measurements performed with an Oxford Instruments Asylum Research Vero AFM using an Au coated tip (AD-2.8-AS, Adama Innovations). a) Topography of the HZO, partly covered with a Pt top electrode. b) Phase scan of the region shown in a). A difference in domain sizes of the bare HZO and the Pt covered area becomes obvious. c) Magnified topography and phase d) of the Pt TE on HZO. e) Overlay of topography and phase on the Pt TE. f) Line profile of the phase, extracted from the red line in d). g) Magnified topography and h) phase of the bare HZO. i) Overlay of topography and phase on HZO. j) Line profile of the phase, extracted from the red line in h).

The piezoelectric coefficient along the direction of the applied bias is described as d_{33} [pm V^{-1}]. It can be determined from the crossing of the butterfly loop in Figure 6.4b, which is ideally (no imprint) located at 0 V bias. Here, it is slightly shifted to negative bias and lies approximately at 2 pm. Given the applied drive amplitude of 2 V during the measurement, the effective d_{33} can be estimated as approximately $|1 \text{ pm V}^{-1}|$.

In PFM, phase measurements provide only relative information on the phase difference, as the absolute phase is subject to an arbitrary offset. To address this limitation and at least determine the direction of phase change, a BiFeO_3 reference sample is utilized. SS-PFM measurements are performed on BiFeO_3 using identical experimental conditions to those used for HZO (see Figure A.4 in the appendix). A comparison of the off-field phase hysteresis (Figure A.4a) reveals an opposite switching direction, indicating that the two materials exhibit reversed deformation directions under identical measurement conditions. With the well-established positive d_{33} coefficient of BiFeO_3

[139, 140], this observation suggests a negative piezoelectric coefficient of -1 pm V^{-1} for HZO.

So far, there are limited studies on the piezoelectric properties of HfO_2 -based materials. However, it is generally accepted that their piezoelectric coefficients are significantly lower than those of conventional ferroelectrics. While theoretical studies have predicted a negative piezoresponse [141, 142], experimental findings have reported positive [22, 28, 143], negative [142, 144], or even coexisting positive and negative d_{33} values [145]. This discrepancy has recently been addressed by Lu et al., who reported a gradual transition from positive to negative d_{33} with increasing field cycling in polycrystalline HZO [131]. They attribute this evolution to the transformation of a weakly polar orthorhombic phase with positive d_{33} ($+3 \text{ pm V}^{-1}$) into a well-developed polar o-phase with negative d_{33} (-2 pm V^{-1}). This is consistent with the value of -1 pm V^{-1} determined here. The epitaxial character of the HZO in this work suggests an already well-developed polar phase, as evident from the absence of the wake-up effect, which is typically observed in polycrystalline HfO_2 -based films and (partly) associated with a field-induced phase change (see Section 2.4).

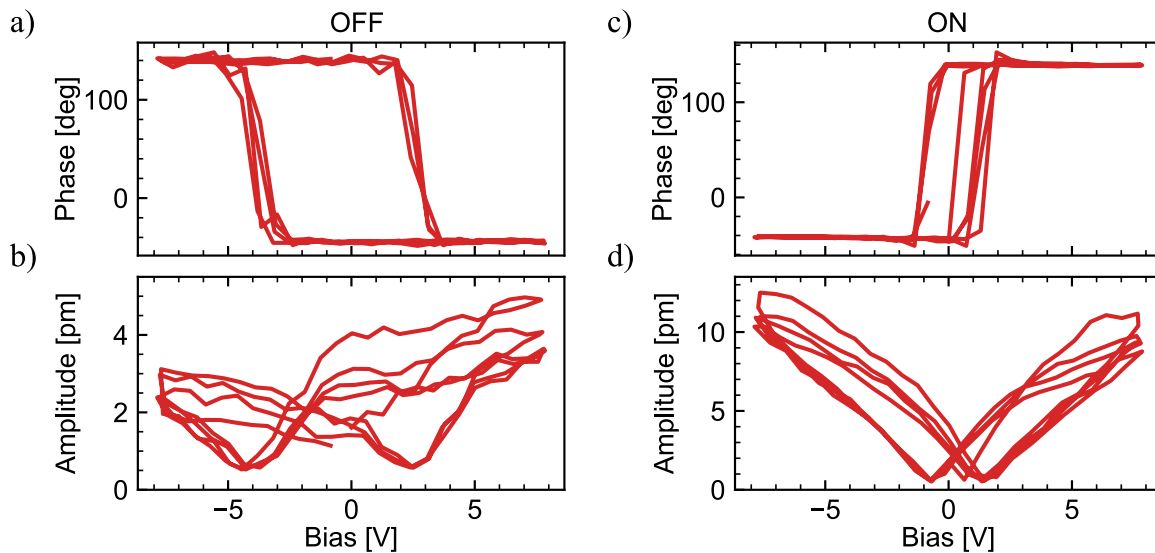


Figure 6.4: Switching spectroscopy measurements performed on the HZO surface of Figure 6.3 with a drive amplitude of 2.0 V. a) Phase and b) amplitude in OFF-field configuration. c) Phase and d) amplitude in ON-field configuration, shown for the sake of completion.

6.2 Resistive Switching

Resistive switching in HfO₂-based materials has been extensively studied over the past decade, primarily driven by its potential for use in non-volatile memory technologies. Among these materials, amorphous HfO₂ is well established due to its compatibility with standard CMOS processes, scalability and the relative ease of integration into device architectures [12, 146–148]. The switching mechanism is generally attributed to the formation and rupture of conductive filaments, which are mediated by oxygen vacancies, see Section 2.2.

In contrast, comparatively fewer studies have investigated resistive switching behavior in crystalline HfO₂-based films [11, 149, 150]. The switching in poly- and especially single-crystalline systems may slightly differ from those in amorphous counterparts, involving a higher variability and enhanced degradation due to more complex defect structures, such as grain boundaries [124, 128, 151, 152].

This chapter presents resistive switching measurements performed on crystalline Hf_{0.5}Zr_{0.5}O₂ (HZO) thin films deposited by pulsed laser deposition. The aim is to evaluate the switching behavior, including key characteristics such as SET/RESET voltages, variability and retention.

LSMO/HZO/Pt devices

Capacitor structures, as shown in Figure 6.5a, are fabricated according to Sections 4 and 5. The LSMO bottom electrode is always maintained at 20 nm, while the HZO layer thickness and device size vary as individually specified.

Figure 6.5b shows an exemplary I-V characteristic of an 8 nm HZO 100 μm² device. The resistive switching behavior is measured for 20 consecutive cycles, demonstrating the cycle-to-cycle variability of SET, RESET and both resistance states.

During resistive switching measurements, no external current compliance is applied and no electroforming step is performed prior to the I-V characterization. The LSMO bottom electrode provides an intrinsic series resistance, which effectively limits the current flow during filament formation and prevents an irreversible device breakdown. The absence of electroforming is discussed at a later point, in Section 6.3.

The device shows a gradual current increase with an abrupt SET to the LRS at negative voltages, demonstrating *counter eight-wise* switching, as expected from the Schottky barrier between the HZO and Pt top electrode (see Section 2.2). The SET voltage shows a significant spread at -2 V of up to ±0.7 V. The RESET is found at +1.4 V, varying up to ±0.5 V and further showing differing abrupt to slightly gradual behavior for different cycles. The SET cycle-to-cycle variability shows no clear trend with increasing cycle number (yellow to black), while the RESET seems to become more abrupt and stable. Contrary to the switching voltages, the HRS and LRS remain relatively stable between cycles, except for the LRS at positive polarity, which is impacted by the RESET variability. The cycle-to-cycle variations of the switching voltages and resistance states within one device generally result from the stochasticity of the oxygen vacancy generation and recombination during each cycle [58, 59, 153]. Resulting ON/OFF ratios are found in the range of 1.5-2 orders of magnitude, depending on the HZO thickness and device area.

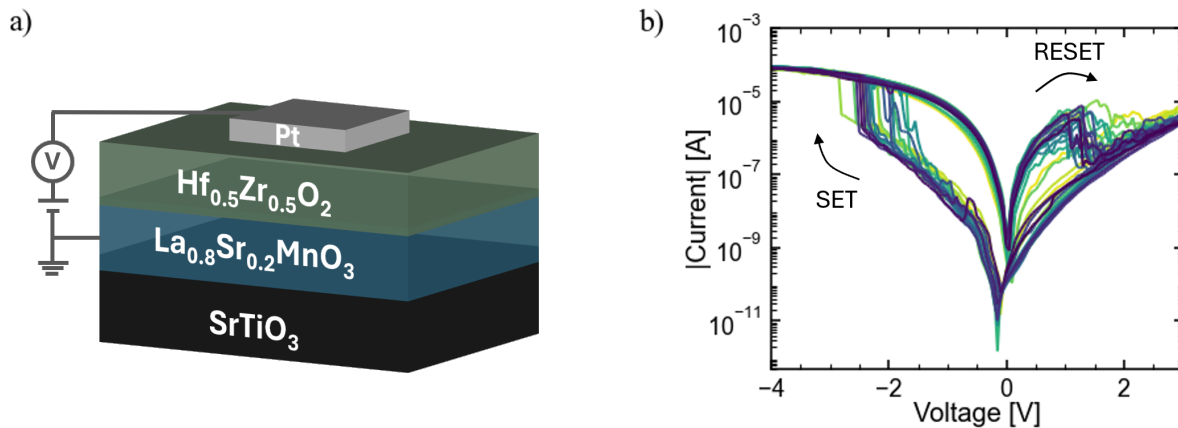


Figure 6.5: a) Capacitor structure used for resistive switching. The voltage is applied to a square Pt top Electrode, while the LSMO serves as bottom electrode and is grounded. b) Resistive switching in a STO/LSMO/HZO(8 nm), $100 \mu\text{m}^2$ device. Measured are 20 consecutive cycles, from yellow to black. The switching direction is indicated by the arrows.

Retention characteristics of the LRS were evaluated by programming the device into the LRS and subsequently monitoring the read current at a bias of -0.2 V over an extended duration, Figure 6.6a. The current remained stable with negligible variation for up to approximately 24 hours, indicating robust short- to mid-term retention. No signs of degradation were observed within this time frame, suggesting good intrinsic stability of the conductive filament under ambient conditions.

To assess the nature of the resistive switching mechanism in the investigated devices, the current levels in both the HRS and LRS were measured at a fixed read voltage of -0.5 V across devices with varying areas, ranging from $50 \mu\text{m}^2$ to $10000 \mu\text{m}^2$. The LRS current remains independent of the device area, consistent with the formation of localized conductive filaments as expected for the filamentary-type resistive switching. In contrast, the HRS current exhibits an approximately linear dependence on device area, which becomes clear by the alignment with the ideal slope of 1 shown by the dashed, grey line in Figure 6.6b. This behavior supports the interpretation that, while the LRS is dominated by localized conduction paths, the HRS is determined by more uniform, area-dependent leakage through the HZO layer.

Figure 6.7a shows a comparison between a measured I-V characteristic and a simulation based on the JART VCM v1 model, which is a compact model describing filamentary switching behavior governed by the valence change mechanism. The simulation successfully reproduces key features of the experimental data, including the abrupt SET transition and the more gradual RESET behavior, along with the corresponding switching voltages. In general, the negative voltage branch of the I-V curve shows excellent agreement between simulation and experiment. However, noticeable deviations appear in the positive voltage branch. These discrepancies are likely attributed to differences in the material interfaces that influence the high resistance state (HRS), as well as the migration of oxygen vacancies across the LSMO/HZO interface, which is an effect not accounted for in the simulation model.

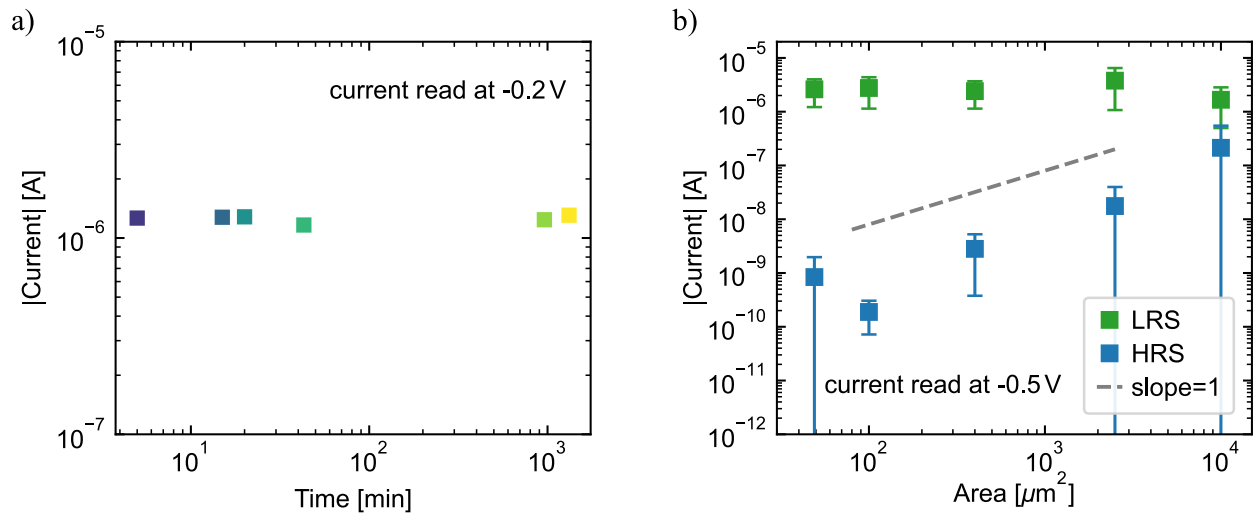


Figure 6.6: a) Retention measurement of the LRS at a read voltage of -0.2 V. The LRS current remains stable over a duration of approximately 24 h, demonstrating negligible drift or degradation. b) Area dependence of the read current in the HRS (blue) and LRS (green), measured at -0.5 V for device areas ranging from $50 \mu\text{m}^2$ to $10000 \mu\text{m}^2$. The HRS current scales approximately linearly with area, consistent with uniform leakage through the HZO. The LRS current is independent of the device area, indicating conduction through a localized filament. The dashed grey line represents an ideal linear scaling (slope = 1) for area-dependent behavior. Reprinted and modified with permission from [154].

The used model is part of the Juelich-Aachen Resistive Switching Toolbox (JART). Initial switching parameters were taken from literature values of Pt/HfO₂/Hf/Pt devices [155] and subsequently adjusted to reflect the device geometry and experimental data. The resulting set of parameters is summarized in the table in Figure 6.7b. Notably, a reduced oxygen vacancy concentration N was used to describe the experimental data to account for the expected lower oxygen vacancy concentration, resulting from the fabrication process (Section 4), the use of Pt and an oxide as electrodes, and the absence of an irreversible electroforming step. Further details on the simulation framework can be found in [155, 156].

To investigate the potential for multi-level switching in this material system, I-V measurements were performed under varying current compliance (cc) conditions, as shown in Figure 6.8a. While multiple resistance states are commonly adjusted via the RESET voltage [157, 158], to eliminate the impact of the cc delay time, this is avoided here due to the higher non-uniformity of the RESET behavior in comparison to the SET behavior (see Figure 6.5b).

The compliance was step-wise reduced down to 0.02 mA, below which reliable SET transitions could no longer be achieved. At the lowest applied compliance, increased variability in the switching behavior becomes already evident, particularly in the SET and RESET voltages as well as in the resulting LRS. Distinct resistance levels emerge predominantly in the negative voltage branch, suggesting at least a certain degree of control over filament formation under limited current conditions.

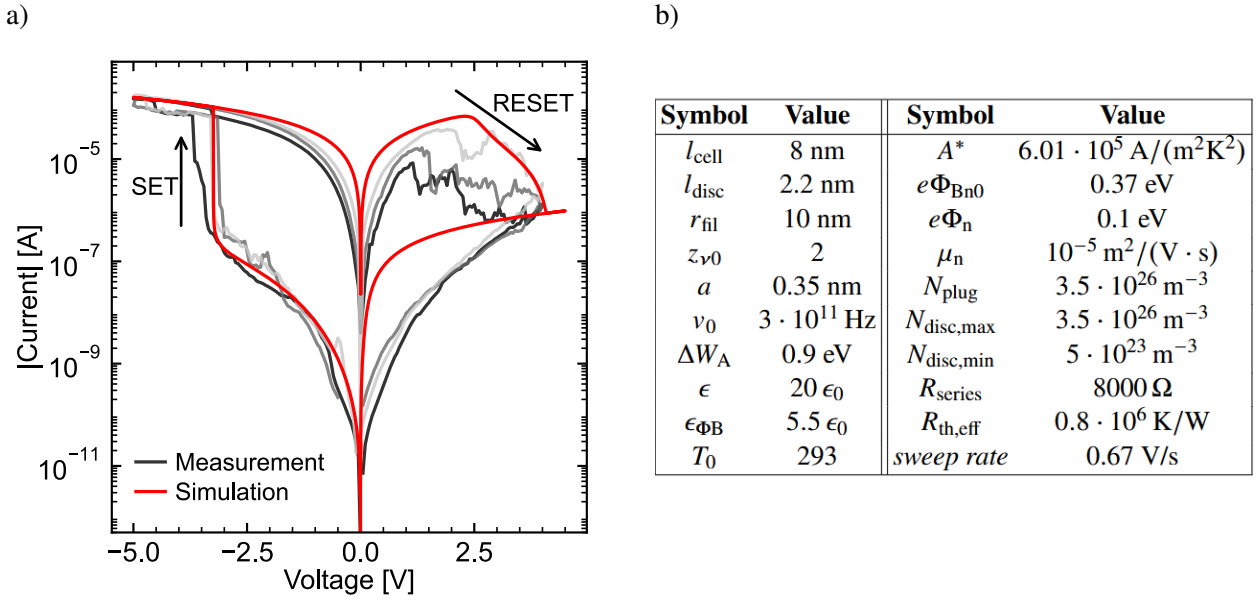


Figure 6.7: a) Comparison of experimental and simulated I-V characteristics using the JART VCM v1 compact model [155, 156]. The simulation reproduces especially the negative voltage branch, including the HRS, LRS, and the abrupt SET. Reprinted and modified with permission from [154]. b) Simulation parameters used in the JART VCM v1 model, adapted from literature values and adjusted to match the geometry and I-V characteristic of the LSMO/HZO/Pt devices [155, 156]. Reprinted with permission from [154].

While this result demonstrates the basic feasibility of cc-controlled resistance tuning in a limited range for LRS and HRS, the resolution and stability of multiple states remain inferior compared to multi-level switching in other (amorphous) HfO_2 -based systems [62, 158], thus representing merely a proof of concept within the LSMO/HZO/Pt system.

It should be noted that in smaller devices $\leq 100 \mu\text{m}^2$ and in samples exhibiting higher initial resistivity, the resistive switching behavior occasionally deviates from that of larger or more conductive structures, in a way that is shown in Figure 6.8b. The SET transition becomes more gradual, while the RESET process is suppressed or vanishes almost completely. This deviating behavior can be attributed to the limited amount of available conductive pathways and oxygen vacancies in smaller or more insulating devices, resulting in unstable or incomplete filament formation [159]. The resulting transient behavior might instead be attributed to an area-dependent switching, where the HZO acts as tunnel barrier that is modulated by the non-localized migration of oxygen vacancies within the HZO and possibly between the LSMO and HZO, instead of an individual conductive path forming through the HZO. Similar behavior has been reported for example for HfO_x , WO_x and CeO_2 [159–161].

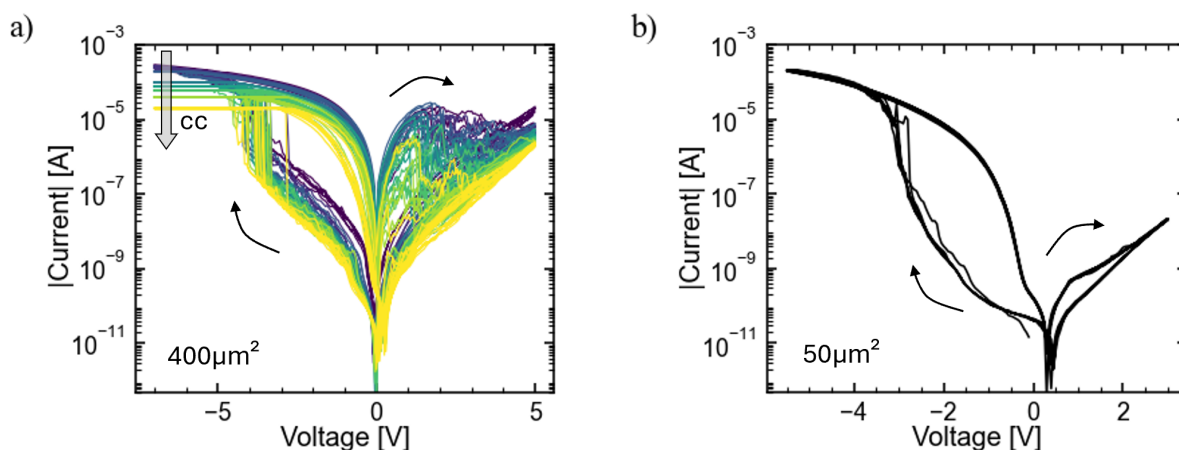


Figure 6.8: a) I-V characteristics measured with decreasing current compliance (cc) applied. Distinct LRS and HRS resistance levels emerge in the negative voltage branch, down to 0.02 mA, below which the SET is no longer reliably achieved. b) Exemplary I-V characteristics of a devices at the lower limit of investigated device sizes ($50 \mu\text{m}^2$), showing a gradual SET and a largely suppressed RESET.

LSMO/HZO/Ti/Pt devices

Introducing bi-layer systems by interfacing the switching oxide with an oxygen-exchange metal layer is a common approach in VCM switching. An additional metal layer serves as a source of oxygen vacancies, which can improve the resistive switching performance by enabling better control over the oxygen stoichiometry within the switching oxide [12, 162, 163]. In contact with HfO_2 , a Ti layer has been shown to scavenge oxygen, leading to the formation of a thin interfacial TiO_x layer. This layer introduces additional oxygen vacancies, which has been reported to improve switching performance by reducing variability in the SET and RESET, as well as in the resulting resistance states [164, 165].

Figure 6.9a shows the switching characteristic of the LSMO/HZO system with a Ti/Pt top electrode, as depicted in the inset. The consistent *counter eight-wise* switching direction suggests that the introduction of Ti did not alter the location of the active switching interface. It implies that the filament modulation does not occur at the LSMO/HZO interface, which could have been assumed, due to the supply of oxygen vacancies from the TiO_x layer as observed for the Pt/ HfO_2 / TiO_x /Ti/Pt system [62, 165]. Furthermore, a switching of the formed TiO_x layer is also not consistent with the switching direction in Figure 6.9a, since in that case applying a negative bias at the Pt would cause an increase of the TiO_x layer thickness or oxidation state, increasing the resistance instead of switching to the LRS, as observed here. Instead, the gradual switching behavior that scales with the device area, as evident from Figure 6.9b, may be attributed to area-dependent switching enabled by the increased oxygen deficiency introduced into the HZO. Qualitatively similar area-dependent, switching of the same polarity and without electroforming has been observed before in HfO_x -based bilayer systems, utilizing TiO_x or Al_2O_3 as oxygen reservoir [160, 166].

The involvement of the whole device area during switching, instead of a single filament, reduces the switching variability by eliminating its stochasticity. However, also the ON/OFF-ratio is reduced,

as the Joule heating is suppressed, and the HZO becomes generally more conductive when n-type doped by an increased oxygen deficiency [12].

In conclusion, while the incorporation of a Ti oxygen exchange layer improved resistive switching performance by reducing variability, the resulting decrease in overall device resistance is incompatible with the measurement of ferroelectric switching in this system (see Section 6.3 for a discussion of requirements).

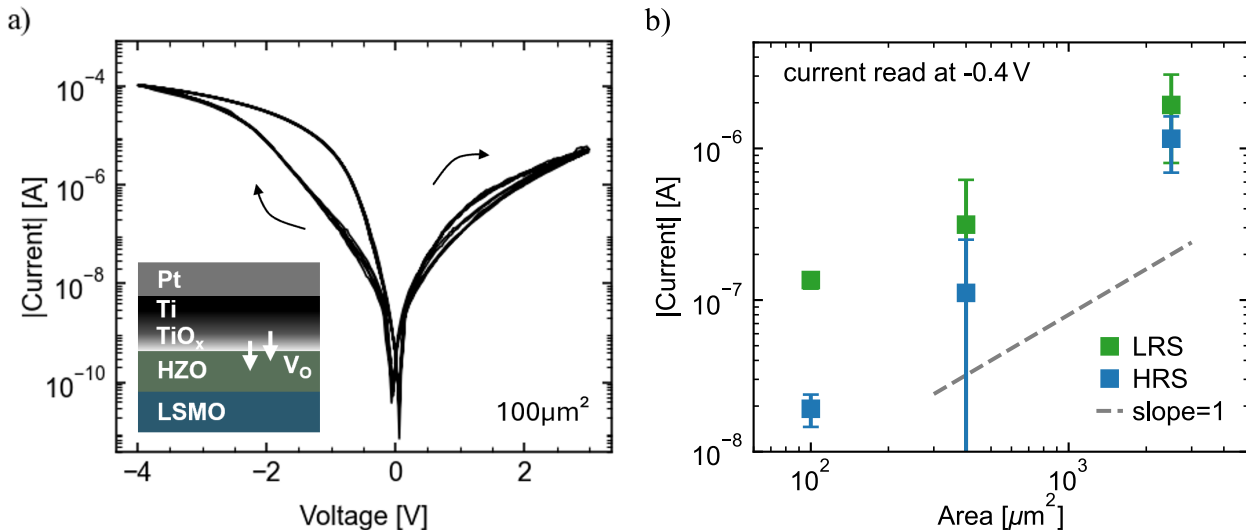


Figure 6.9: a) I-V characteristics of the LSMO/HZO system with a Ti/Pt top electrode. The inset shows a schematic of the device structure. b) Area dependence of the read current in the HRS (blue) and LRS (green), measured at -0.4 V for device areas ranging from $100\mu\text{m}^2$ to $2500\mu\text{m}^2$. The HRS and LRS currents scale approximately linearly with the device area. The dashed grey line represents an ideal linear, area-dependent scaling (slope = 1).

6.3 Dual-Mode Switching

The preceding chapters have shown that both ferroelectric and filamentary-type resistive switching can occur in the LSMO/HZO/Pt system. Notably, resistive switching was achieved without the need for electroforming, which is commonly required in oxide-based systems. This absence of electroforming is a key condition for enabling subsequent ferroelectric switching within the same device, as it prevents a soft breakdown and the associated irreversible reduction in resistance. A RESET to an HRS comparable to the pristine resistance is expected to allow the voltage to drop across the entire device area, thereby facilitating ferroelectric switching rather than confining the voltage drop to the residual filament and the active electrode.

The intrinsic current-limiting behavior of the LSMO bottom electrode is another important factor supporting fully reversible filamentary switching. In contrast to external current compliance, which can exhibit a response delay allowing current overshoots that may cause irreversible device changes [167, 168], the LSMO series resistance provides an effective built-in compliance. This helps to suppress excessive current flow and associated Joule heating.

Having these prerequisites fulfilled, a hysteresis loop measured at 1 kHz, Figure 6.10a, is followed by three consecutive resistive switching cycles measured with quasi-static voltage sweeps, shown in Figure 6.10d. The device is kept in the HRS after the third cycle is completed. The HRS shows the same resistance as in the pristine state within reasonable cycle-to-cycle variability. It should especially be noted that the device is not subjected to a deviating, strong RESET procedure to prepare the device for following ferroelectric switching. This property to return to the quasi-pristine state after resistive switching sets this work apart from other reports of ferroelectric and filamentary-type switching in one device [37, 169].

Starting immediately from the HRS after the third resistive switching cycle, the subsequent ferroelectric hysteresis is shown in red in Figure 6.10b, measured identically to the pristine one. The red loop demonstrates a transition period of the device, where an increased leakage current is superimposed to the still clearly visible ferroelectric switching, obvious from the switching current peaks despite the deformed hysteresis loop. The leakage current slightly exceeds the set current of 10^{-6} A, which shows as an applied current compliance. Subsequent continuous ferroelectric cycling reduces the leakage current progressively. The resulting hysteresis in blue in Figure 6.10b is identical to the pristine one, prior to any filamentary-type resistive switching.

In the same way, the device is subjected to another sequence of three quasi-static resistive switching cycles, shown in Figure 6.10e. Changing the biasing to a frequency of 1 kHz, again addresses the ferroelectric switching, and the hysteresis in green in Figure 6.10c is obtained. The direct comparison of all three ferroelectric polarization and I-V loops clearly demonstrates that the intermediate filamentary switching had no impact on the polarization and coercive field of the device.

The smooth transition between both switching mechanisms, along with the comparable voltage ranges for SET/RESET and coercive switching, could suggest that the observed resistance changes stem from the polarization reversal. However, despite the apparent similarity of the resistive switching behavior to filamentary-type VCM switching, the following section presents compelling evidence that strongly opposes a ferroelectric origin of the resistance states.

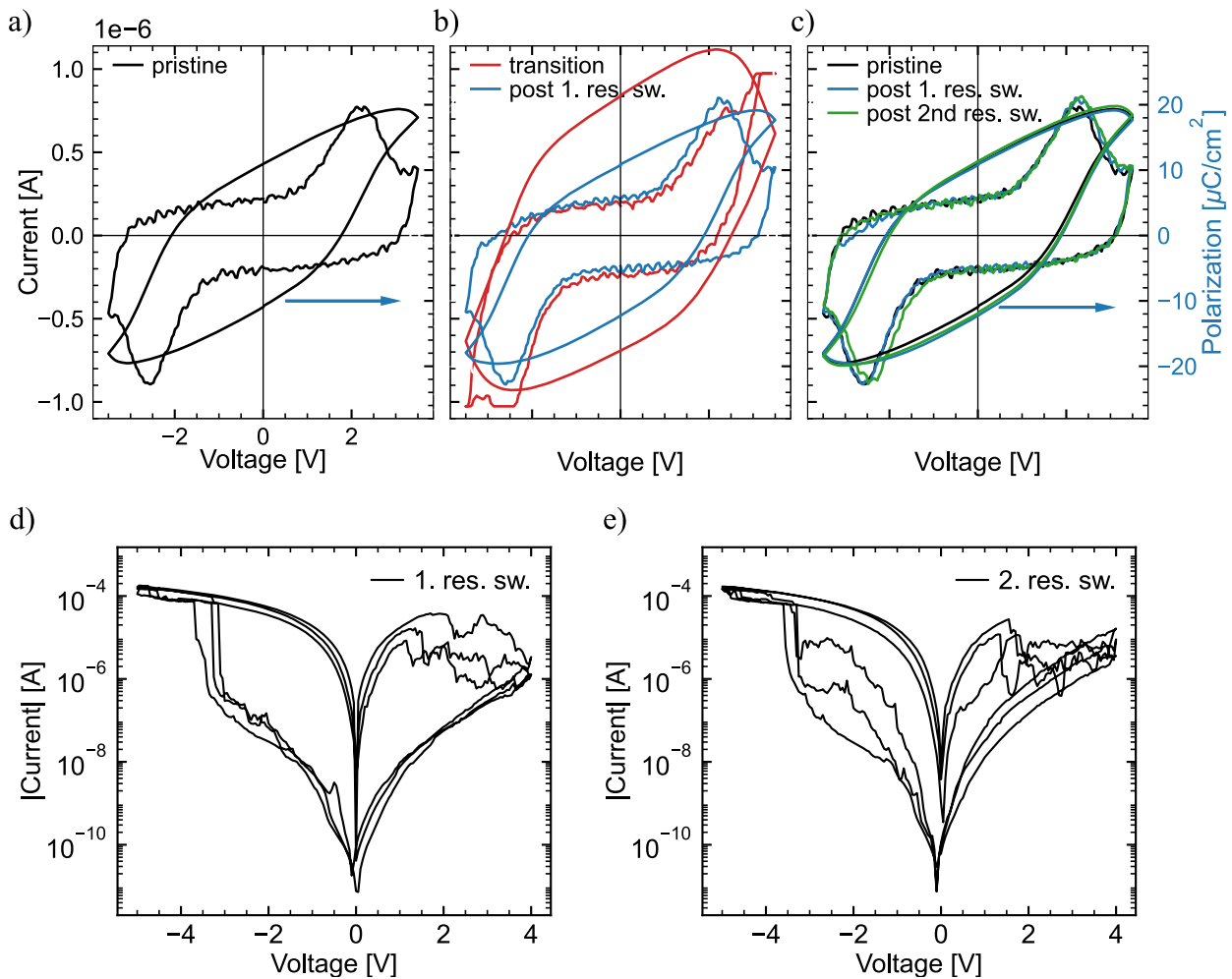


Figure 6.10: Ferroelectric hysteresis and I-V curve of the same device measured at 1 kHz a) in its pristine state, prior to any resistive switching, b) a transition period (red) right after the resistive switching in d) and final hysteresis after the transition (blue). c) Overlay of the ferroelectric switching in the pristine state (black) and after one (blue) and two (green) sets of three consecutive cycles of resistive switching. d) Three cycles of resistive switching applied after the pristine hysteresis in a), measured with quasi-static voltage sweeps. e) Three cycles of resistive switching applied after the hysteresis in b). a)-d) Adapted with permission from [154].

If the resistance change were driven by a ferroelectric polarization-related mechanism, it would involve the entire device area and the resulting current levels would be expected to scale accordingly with device size. As demonstrated in Figure 6.6b and discussed in Section 6.2, the resistive switching of the LSMO/HZO/Pt stack is found independent of the device area, in line with the localized filamentary-type switching.

Moreover, the SET and RESET voltages associated with resistive switching consistently exhibit an asymmetry of approximately 1.5 V. In contrast, the coercive voltages are symmetric, indicating a mismatch between the two phenomena. While an overall shift in switching voltages could be attributed to the differing biasing conditions (1 kHz versus quasi-static), the observed asymmetry cannot be explained by this factor. This further supports the conclusion that the ferroelectric hysteresis and the resistance change originate from different mechanisms. Although polarization-modulated resistance changes of similar magnitude have been reported in literature [170], polarization switching as the origin of the resistance change can be clearly excluded here.

It is proposed that the interchangeable operation of both ferroelectric and filamentary-type resistive switching is generally possible, provided the conductive filament is sufficiently dissolved during the RESET. This allows the voltage pulsed during ferroelectric switching to drop across the entire device area. This is usually (intentionally) avoided in filamentary switching because confining the modulation of the device resistance to the small disc region between filament remainder and active electrode bears several advantages, such as lower switching voltage, faster switching, and potentially reduced variability by suppressing the formation of filaments at varying locations [12, 171].

As previously discussed, the absence of electroforming, which is typically associated with irreversible modifications to the oxide, and the passive current compliance provided by the LSMO, which suppresses excessive Joule heating, are critical factors enabling complete filament deconstruction. It should be noted that in this context, a "complete deconstruction" refers to the restoration of the pristine device resistance. This does not exclude the possibility that a residual concentration of oxygen vacancies may remain locally accumulated.

It was shown that oxygen deficiency and a reduced HfO₂ thickness can lower the forming voltage, approaching the SET voltage [172, 173]. The deposition conditions of the HZO are not expected to introduce sub-stoichiometry, (see Section 4). Instead, it was demonstrated that the deposition of HZO onto LSMO introduced a slight reduction of the LSMO (see Section 4 and Figure 4.4). Following this, the LSMO bottom electrode may serve as a reservoir for oxygen vacancies, supplying them under appropriate bias to support the filament formation without the need for a high-voltage electroforming step that would irreversibly generate vacancies within the HZO layer. Conversely, during the RESET process, vacancies could be stored back in the LSMO, enabling the recovery of a resistance state comparable to the pristine state. Indeed, vacancy migration across a La_{0.67}Sr_{0.33}MnO₃/Hf_{0.5}Zr_{0.5}O₂ interface has been demonstrated at similar voltage and time scales as those employed in this work, although these findings were obtained under ultra-high vacuum conditions, which may enhance oxygen vacancy dynamics by promoting oxygen removal [35].

Even with a sufficient supply of oxygen vacancies into the HZO layer, the formation of a conductive filament still requires their alignment along a continuous path. As shown by the conductive AFM

measurements of a pristine HZO film in Section 4 and Figure 4.5, inherent variations in local conductivity are present. These variations are likely associated with grain or phase boundaries, which have been reported to enhance defect and oxygen vacancy mobility [124, 127, 128]. Such regions of locally increased conductivity can serve as preferential sites for filament formation, eliminating the need for a soft dielectric breakdown to establish a conductive path.

During the RESET process, filament dissolution initiates at the Pt electrode. The less abrupt nature of the RESET transition, compared to the SET, can be attributed to the formation of an oxygen vacancy gradient that opposes the applied positive bias [174, 175]. Additionally, the inherently higher oxygen affinity of Hf and Zr relative to Mn promotes filament dissolution and supports the back-migration of oxygen vacancies into the LSMO layer.

A comparison of the HRS with the ferroelectric switching current in Figure 6.10a and 6.10d shows that the HRS current remains below the ferroelectric switching current up to approximately 3.5 V. The higher frequency of ferroelectric switching further reduces electrical stress on the device compared to the quasi-static I–V sweeps used for resistive switching. This helps suppress leakage currents and prevents unintentional SET events, which could otherwise obscure the ferroelectric response. Nonetheless, a transition phase is occasionally observed immediately after resistive switching, shown in red in Figure 6.10b. This phase is characterized by an elevated leakage current superimposed on the ferroelectric switching, likely resulting from an incomplete RESET. However, the presence of clearly defined ferroelectric switching at voltages comparable to those of the pristine state suggests that this leakage arises from a residual increase in oxygen vacancy concentration within the HZO, rather than from an incompletely dissolved filament. In the latter case, the voltage drop across the whole device area would be diminished, not allowing equally pronounced ferroelectric switching as in the pristine state. The application of additional switching cycles, to recover a hysteresis loop resembling that of the pristine state, likely facilitates the redistribution of oxygen vacancies and their re-incorporation into the LSMO layer. From the final hysteresis loops in Figure 6.10c, it can be assumed that the pristine oxygen vacancy concentration in HZO is fully restored.

Redistribution of vacancies during ferroelectric switching is a known phenomenon, particularly during the wake-up process in polycrystalline HfO₂-based ferroelectrics, where it is typically accompanied by a phase transition from the t- to o-phase and an associated increase in polarization [32, 36]. Here, such effects can be ruled out, as the hysteresis loops following resistive switching and the transition phase closely resemble those measured in the pristine state. Although no significant impact is observed here, the additional cycling required to reduce leakage currents could, in general, contribute to ferroelectric fatigue, manifesting as a reduction in polarization and oxygen vacancy generation.

The unchanged hysteresis loops observed after resistive switching confirm that the two switching mechanisms do not interfere with one another, provided the device is switched into the HRS prior to ferroelectric operation. This specifically demonstrates that the oxygen vacancy migration associated with filament formation and dissolution does not compromise the ferroelectric properties of the HZO layer. Conversely, a conductive path formed by oxygen vacancies can be deliberately induced within the ferroelectrically switching HZO by applying higher voltages and quasi-static

sweeps, as opposed to the high-frequency (1 kHz) voltage pulses used during ferroelectric switching. Therefore, polarization switching and resistive switching can be regarded as independent phenomena coexisting within the same device.

It can be concluded, that an initial concentration of oxygen vacancies in the HZO and LSMO, combined with their mobility across the interface and the presence of inherent preferential conductivity paths within the HZO, enables immediate filamentary-type VCM switching without electroforming and the recovery of the pristine resistance in the HRS, finally allowing the dual-mode operation of LSMO/HZO/Pt devices.

In order to gain a deeper understanding of the coexistence of these two switching mechanisms, a more detailed investigation of oxygen vacancy migration and accumulation, both qualitatively and quantitatively, is required. This will be the focus of the following chapters.

7 Spectromicroscopic Analysis of the Switching Phenomena

Parts of this chapter have previously been published in:

J. Knabe, K. Goss, Y.-P. Liu, E. Golias, A. Zakharov, I. Cojocariu, M. Jugovac, A. Locatelli, T. O. Menteş, D. Céolin, A. Gutsche, D. Gogoi, M. L. Weber, R. Timm, R. Dittmann, "Oxygen Vacancy Dynamics in Different Switching Modes of $\text{Hf}_{0.5}\text{Zr}_{0.5}\text{O}_2$ ", *ACS Nano* 2025 19 (32), 29405-29415

To further understand the dual-mode operation of LSMO/HZO/Pt devices that was demonstrated in the previous chapter, it is especially elusive to investigate the oxygen vacancy migration and accumulation during both switching mechanisms in a qualitative and quantitative manner. This is described in the following, utilizing spectroscopic and microscopic techniques based on synchrotron radiation.

7.1 Photoemission Electron Microscopy - Filamentary Switching

Detection of the highly localized filaments responsible for the resistance change via their electrochemical footprint requires spatially resolved spectroscopy. In order to achieve this, XPEEM experiments were performed at the MAXPEEM beamline at MAX IV synchrotron Lund, Sweden and the Nanospectroscopy beamline at Elettra synchrotron laboratory, Trieste, Italy. The instrument used at both beamlines is the *SPELEEM III* from *Elmitec GmbH, Germany*. Details about the instruments and beamlines can be found in [113] and [114].

7.1.1 Stability under radiation

Prior to conducting switching experiments, it is essential to verify whether the sample undergoes any changes upon irradiation under UHV conditions within the chamber. In order to assess this, the Hf 4*f* core-level spectrum of a device that is covered by the graphene top electrode is continuously measured for approximately 30 minutes, with an integration time of 5 s per measurement. The evolution of the spectrum over this time period is shown in Figure 7.1a. No clear spectral changes are observed, and especially no indication of a reduction in the form of an emerging suboxide at lower binding energies is detected.

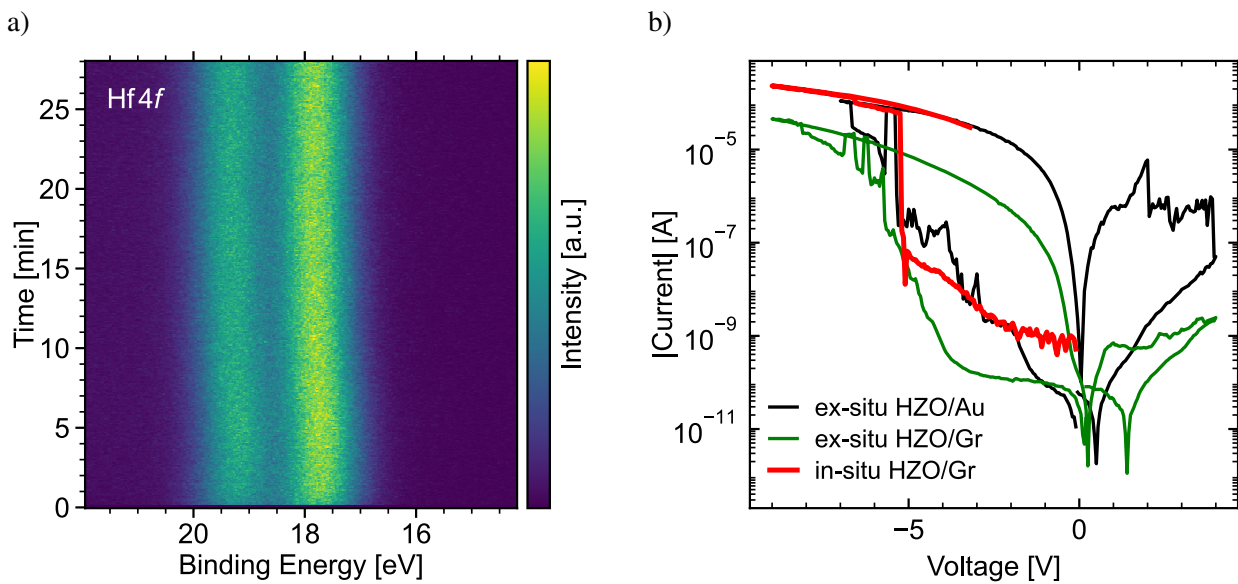


Figure 7.1: a) Repeated measurement of the Hf 4*f* doublet over an extended time period. b) Comparison of resistive switching curves of LSMO/HZO in different setups and with different top electrodes. The devices with graphene top electrode are in the XPEEM geometry and with Au top electrode in the delamination geometry (Section 5.1.1). The *in-situ* switching was performed to set the device in Figure 7.2a into the LRS prior to the shown XPEEM measurement. Adapted with permission from [134].

7.1.2 Filament & Reduced Structures

The electro-chemical structure of the filaments in the STO/LSMO/HZO material system is to be investigated. In this system, the active interface, specifically, the Schottky barrier, is situated at the top, thereby enabling surface-sensitive XPEEM measurements to detect changes effectively. The selection of graphene as a photoelectron-transparent top electrode has been shown to enhance the signal yield from the underlying oxide layer when compared to conventional materials such as Pt or Au, which are commonly used in memristive devices [176]. Au leads from the device side leading to the sample periphery establish electric contact between the graphene top electrode and the XPEEM sample holder for *in-situ* biasing. The device fabrication and geometry are described in detail in Section 5.1.1 and in [133]. The device is mounted inside the XPEEM chamber and

switched into the LRS to establish a conductive filament. The corresponding switching curve, along with comparable *ex-situ* switching data, is shown in Figure 7.1b, where resistive switching across different experimental setups and top electrodes is compared. Devices with a graphene top electrode are measured in the XPEEM geometry, as previously described. The *in-situ* switching curve refers to the device shown in Figure 7.2a when set into the LRS inside the UHV chamber prior to the XPEEM measurement. The *ex-situ* switching curve with graphene refers to an equivalent device, while the curve with Au top electrode refers to an exemplary device of the delamination geometry (Section 5.1.1). The observed variations in current levels within the LRS and HRS can be attributed to differences in the setup used for biasing. The *ex-situ* switching with graphene electrode i.e., was conducted on the XPEEM sample holder with a portable setup, while the *in-situ* switching involved various additional connections. All samples exhibit a comparable HZO thickness of approximately 8 nm.

XPEEM image stacks were acquired at a photon energy of 200 meV and at increasing kinetic energies with a step size of 100 meV for core-level spectra. Figure 7.2a and 7.2b show the Hf 4*f* measurement of a device in the LRS at the absolute and qualitative binding energies indicated by the inset in the bottom left. The two different binding energies are selected to highlight the observed deviations from the generally stoichiometric HZO surface. The presence of contrast features in the images can serve as an indication of a generally higher local photoelectron emission, or local electro-chemical deviations that are directly correlated to the binding energy chosen for the extracted image.

Figure 7.2a provides an examination of the higher binding energy side of the Hf 4*f*_{7/2} peak. Bright, spotty structures appear within the device area and are distributed in a nonuniform manner. For reference, Figure A.5 presents XPEEM Hf 4*f* measurements of two equivalent devices, measured in the pristine state. The images are extracted at the same relative positions of the Hf 4*f* spectrum as in Figure 7.2a. They do not exhibit similar spotty structures, thereby confirming that such structures emerge as a result of the bias applied to switch into the LRS. The presence of darker regions that appear in the LRS, as well as the pristine devices, can be attributed to contamination resulting from the graphene transfer. This contamination is likely to be remaining polymer residues.

The zoom-in in Figure 7.2b is extracted at the lower binding energy edge of the Hf 4*f*_{7/2} peak. A contrast feature is revealed at the bottom right corner of the device that exhibits an increased intensity in that binding energy region. The approximately elliptical spot can be estimated at 160x100 nm in diameter, which can serve as an upper estimation of the actual filament diameter. This estimation is based on the assumption that the graphene layer on top of the HZO might broaden the appearance of the filament and the limited lateral resolution of the instrument, where the microscope resolution is reported at a minimum of about 20 nm. Considering the FWHM (full width at half maximum) of the spot intensity, a size of 95x55 nm in diameter is identified. An asymmetry of the filament, as it is found here, could potentially be attributed to the contribution of an adjacent subfilament to the conduction, as has been previously documented in SrTiO₃ [60, 177].

Core-level spectra are extracted from the image stacks using the *IGOR Pro* software. A reference spectrum is extracted from a region close to the features to exclude shifts of the spectra that can occur due to the X-ray beam alignment within the field of view of the measurement. The Hf 4*f* doublets in

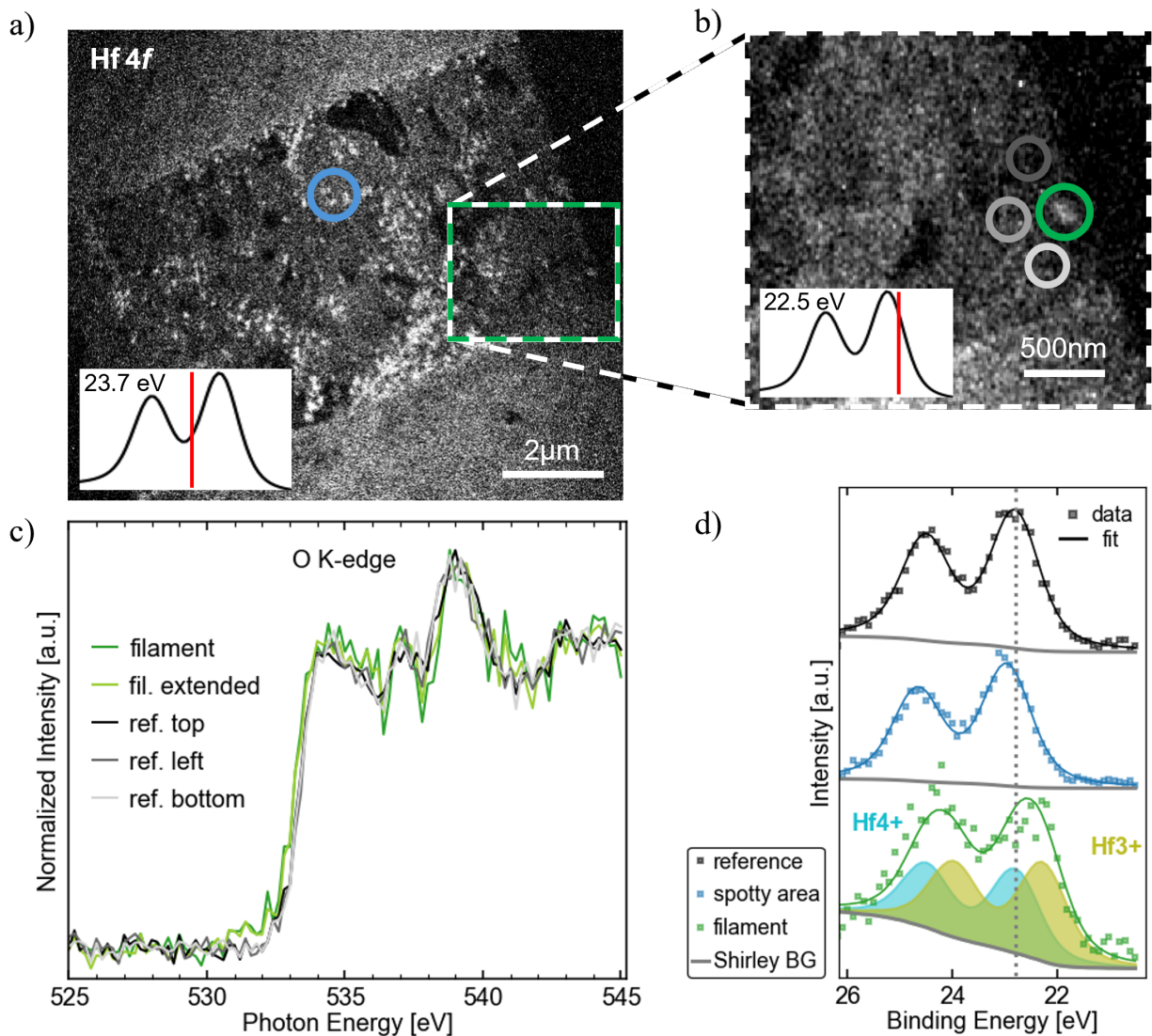


Figure 7.2: a) XPEEM Hf 4f image of a device in the LRS acquired at 200 eV photon energy. Image extracted at 23.7 eV binding energy. The inset in the bottom left shows the relative position of the extracted image. The blue circle highlights the area from which following spectra are extracted. b) Zoom-in on the filament region. Image extracted at 22.5 eV binding energy. The green and grey circles highlight the filament and reference regions, respectively. c) O K-edge of the filament spot, extracted in a narrow and extended region, and several references around the filament (grey). d) Hf 4f data (squares) and envelope of fit components (line) extracted from the different marked regions in a) and b). The spectra are fitted with a Shirley background and Voigt doublets. The filament spectrum is shifted and widened, justifying a suboxide doublet. Adapted with permission from [134].

Figure 7.2d are fitted utilizing a Shirley background and Voigt profiles, using the software *KolXPD*. The branching ratio was fixed according to the spin-orbit splitting, and the peak separation was set to 1.71 eV. Since the filament spectrum is clearly broadened towards lower binding energies

compared to the reference, the introduction of a suboxide doublet is justified. Consequently, the peak position of the Hf^{4+} component is fixed at the reference position. The Hf 4f spectrum of the spotty region in Figure 7.2d does not show a change in shape. Its position was not fixed for the fit, accounting for a rigid shift of the spectrum. A shift of about 0.2 eV to higher binding energies is revealed. The peak shape and FWHM were kept constant for all fits.

Filament

The spectrum of the filament spot is significantly broadened and shifted to lower binding energies, corresponding to an additional Hf^{3+} suboxide doublet. It makes up 54% of the total Hf 4f peak; in comparison, no suboxide is found in the reference spectrum. The oxygen vacancy density in the filament $N_{V_0} \left[\frac{1}{\text{m}^3} \right]$ can be calculated with the densities ρ and molar masses M of HZO and the Avogadro constant N_A :

$$N_O = \frac{\frac{\rho_{\text{HfO}_2} + \rho_{\text{ZrO}_2}}{2}}{\frac{M_{\text{Hf}} + M_{\text{Zr}}}{2} + 2M_O} \cdot N_A \cdot 2 \quad ; \quad N_{V_0} = N_O \cdot \frac{\#V_O [\%]}{100} \quad (7.1)$$

It results that the measured suboxide contribution in the filament corresponds to an oxygen vacancy concentration of 13.5%, assuming charge neutrality and an equal suboxide contribution from the Zr. Following Equation 2.3, the oxygen vacancy concentration equals an oxygen vacancy density of $75 \cdot 10^{26} \text{m}^{-3}$. Due to the surface sensitivity of XPEEM, this density can only be assumed for the top interface of the HZO. Given the poor signal-to-noise ratio in the filament spectrum, the fitting and subsequently calculated vacancy density may exhibit a significant degree of error.

It was not possible to measure a device in the HRS to identify the degree of filament dissolution. In all attempts, a destructive discharge in the XPEEM instrument prevented repeated measurements of the same device. This issue is further discussed in Section 5.1.1.

In order to gain further confirmation on the filament properties, absorption spectra of the same region are measured. Figure 7.2c shows the O K-edge spectra of the filament and several references. Due to the small feature size, extracted spectra are highly sensitive to the precise choice of the selected region. In an attempt to improve the significance of deduced conclusions, a filament spectrum is extracted from a smaller region (dark green) and additionally from a slightly extended region (light green). Furthermore, several reference regions around the filament are included to exclude systematic shifts across the field of view as an origin of small deviations of the filament spectra. All spectra are background corrected by a linear fit of the pre-edge and normalized by a second-order polynomial to the post-edge using the software *Athena*. Due to the short data range, it is not possible to determine an unambiguous trend of the post-edge for normalization. Subtle changes in the normalization to the post-edge line are found to alter the resulting peak intensities severely, consequently preventing quantitative interpretation of the peak intensities. Nevertheless, a consistent qualitative difference between both filament regions and all references can be identified. A small shift of the absorption edge to lower energies, together with an emerging pre-edge feature, is visible for the filament. Furthermore, a change in the e_g peak shape seems likely between

filament and references. There, disregarding the absolute intensities, the filament region appears to have a relatively higher shoulder on the higher energy side. As described in Section 3.6, a shift to lower energies as well as changes in the peak shape can be explained by oxygen loss and the related additional electrons. The exact origin of changes in the peak shape is complex to determine, especially considering the poor signal-to-noise ratio of the measurement.

Cho et al. found a flattening together with a shift in the absorption edge when comparing $\text{HfO}_{1.8}$ with HfO_2 , very well resembling the changes in Figure 7.2c [178]. The structural change from tetragonal ZrO_2 over mixed-phase HZO to monoclinic HfO_2 was also found to severely impact the absorption edge position and e_g peak shape. The additional crystal field splitting of the monoclinic compared to the tetragonal phase was also found to cause e_g peak broadening up to the emergence of a second peak. This was accompanied by a shift of the absorption edge to higher energies, which in disagreement with the findings here, renders oxygen loss more probable than a phase change [109].

In summary, the O K-edge spectra support electro-chemical changes of the HZO at the filament site. Due to the insufficient resolution and energy range, the origin of said changes can only be assumed. Most likely, as expected from the Hf 4f spectrum, a local reduction is responsible for the observed changes. Also, a phase change at the filament site, possibly in response to the heat development during filamentary switching, can not be fully excluded.

XPEEM investigations were extended further to simpler device architectures of the delamination geometry (Section 5.1.1). This was done to underscore the representability of the findings on graphene top electrodes. Devices of STO/LSMO/HZO/Au were prepared and switched into the low resistive state *ex-situ*. The Au top electrodes were subsequently delaminated *in-situ*, thereby preventing filament re-oxidation and enabling access to the bare oxide surface for XPEEM measurements. Navigation after top electrode removal is possible via workfunction contrast due to Au residuals and possible variations in surface contamination, see Section 5.1.1. The measurement was conducted at the Nanospectroscopy beamline at Elettra synchrotron laboratory, Trieste, Italy. The Hf 4f measurement in Figure 7.3a reveals a circular feature with reduced intensity at higher binding energies in comparison with the surrounding region. Figure 7.3b shows the spectra of the feature-core and a reference, as marked in Figure 7.3a. A broadening of the filament spectrum clearly indicates a suboxide contribution comparable to the prior *in-situ* findings with graphene top electrode (Figure 7.2c). The spectra are fitted using CasaXPS and GL(30) doublets with a Shirley background. The Hf^{4+} position, as well as spin-orbit splitting and peak shape, are fixed. The deduced filament diameter of approximately 100 nm and the vacancy oxygen concentration of 14.5% support the prior findings on the graphene device geometry, thereby further validating the universality of the *operando* device geometry.

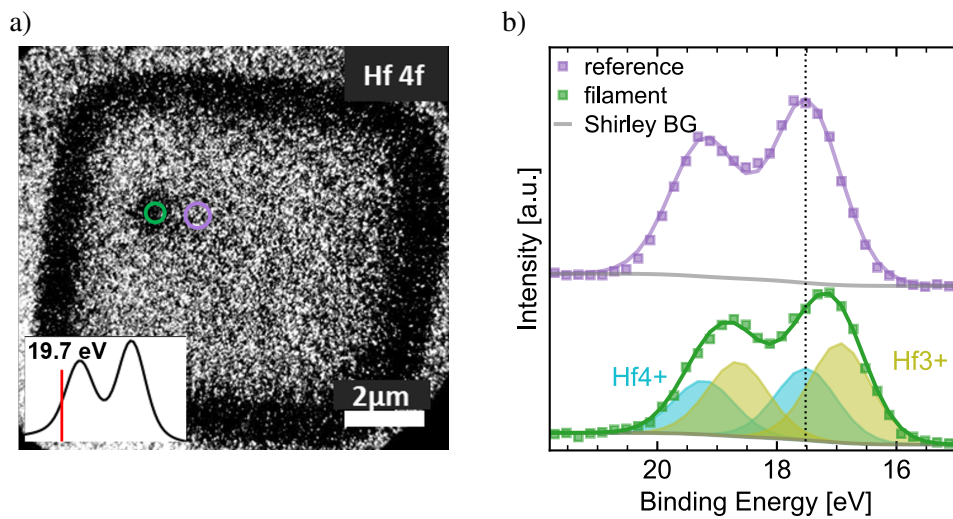


Figure 7.3: a) XPEEM Hf 4*f* image of a delamination device in the LRS acquired at 200 eV photon energy. Image extracted at 19.7 eV binding energy. The inset in the bottom left shows the relative position of the extracted images in a) and b). The circles highlight the areas from which following spectra are extracted. b) XPEEM Hf 4*f* raw data (squares) and envelope of fit components (line) extracted from the different regions in a) in comparison with a reference region obtained in the vicinity. The spectra are fitted with a Shirley background and GL(30) doublets. The filament spectrum is shifted and widened, justifying an additional suboxide doublet. Adapted with permission from [134].

Filament - Discussion

From the XPEEM investigations, an approximate filament diameter of around 100 nm was determined by the extent of a strongly reduced region in the Hf 4*f* spectrum (Figure 7.2b and 7.3a). The spectral analysis of the region revealed a significant contribution from the Hf³⁺ suboxide, which was utilized to estimate the concentration of oxygen vacancies within the material. Taking into account the average of measurements obtained from both the graphene and the delaminated device geometry (Figure 7.2c and 7.3b), an oxygen vacancy concentration of approximately 14% was calculated. These results are consistent with the order of magnitude found in previous studies on amorphous Ta₂O₅, where filament diameters of about 120 nm and an oxygen vacancy concentration of 20% were reported in a similar experiment [17]. The similarity in these values suggests that, despite differences in material systems and structural ordering, the characteristic size and defect densities of filaments may exhibit comparable scales under certain experimental conditions.

It is important to note that there is a limited number of experimental reports specifically addressing filament formation and properties in HfO₂, particularly in its crystalline form. Some of the available studies will be discussed in the following.

For instance, C-AFM and transmission electron microscopy (TEM) were employed to investigate filament characteristics in polycrystalline HfO₂/TiN. The findings revealed filament diameters ranging between 20 nm and 100 nm, along with indications of oxygen deficiencies reaching up to 55% [179, 180]. However, it should be noted that the switching behavior and filament properties

observed in these studies are not directly comparable to those of this work, which were obtained under standard filamentary switching protocols. In particular, the switching was induced locally by the C-AFM tip, resulting in significantly different electrical field distribution, series resistance, and additional surface or interface effects arising due to the exposed switching oxide.

In the case of amorphous HfO_2 , the formation of sub-10 nm filaments has been observed in Hf/a-HfO_2 with C-AFM tomography after top electrode removal. The devices were embedded within a 1T1R cell architecture, exhibiting notably low switching voltages of $<\pm 1$ V and a current compliance of $50 \mu\text{A}$, effectively preventing current overshoots due to the current-limiting role of the transistor in series [181].

Furthermore, metallic filaments with diameters ranging between 5 nm and 15 nm have been observed directly in amorphous HfO_2 via TEM [182, 183]. Significantly smaller degrees of reduction in the switching oxide were reported in $\text{a-ZrO}_x/\text{Ta}$ via XPEEM measurements [184]. However, it should be noted that the extent of reduction was likely underestimated due to the limited spatial resolution, which may not fully capture localized nanoscale features. Deshmukh et al. utilized Scanning Thermal Microscopy (SThM) to further explore filaments in a-HfO_2 on TiN with either TiN or graphene (single and double-layer) serving as the top electrode material. Their approach provided only indirect evidence of filament dimensions by mapping localized thermal hot spots under steady-state bias conditions. The observed hot spots were >120 nm, which corresponding simulations assigned to actual filament diameters of less than 20 nm. Despite the indirect nature of the measurement, the study also found minimal differences in the hot spot diameters between devices with TiN and those with graphene top electrodes. This observation further emphasizes the viability of graphene as a representative top electrode material for filamentary switching investigations [185].

Several simulation studies have been conducted to determine the characteristic filament size and oxygen vacancy concentration in both HfO_2 and ZrO_2 [62, 186, 187]. A significant discrepancy becomes apparent when comparing these theoretical findings with the experimental results discussed previously, where well-pronounced reductions of the oxide and even near-metallic states were observed within the filaments.

It is important to recognize that due to substantial differences in experimental setups, material systems, and electrical treatment, a straightforward comparison of the simulation outcomes with the experimental studies mentioned before is challenging and of limited reliability. Consequently, rather than attempting a direct comparison between experimental results, an assessment of this work's experimental results in the context of the existing simulation studies is provided in the following discussion.

The filament diameter determined in this work, based on XPEEM analysis, appears to be consistent with simulations. Specifically, Cueppers et al. assumed a filament diameter of 90 nm for a fitting of experimental switching data on $\text{Pt/HfO}_2/\text{TiO}_x/\text{Ti}/\text{Pt}$, while Bengel et al. used diameters in the range of 50-70 nm for $\text{Pt/ZrO}_x/\text{Ta}/\text{Pt}$. The close agreement suggests a general consistency between experimental findings and theoretical predictions [62, 186, 187].

The oxygen deficiency obtained from the suboxide contributions in the Hf core-level spectra (see Figure 7.2 and 7.3) can be translated into an average approximate oxygen vacancy concentration of

$78 \cdot 10^{26} \text{m}^{-3}$. This value represents an estimation of the disc region at the HZO surface. Notably, this concentration is of the same order of magnitude as those reported in the simulation studies, where $20 \cdot 10^{26} \text{m}^{-3}$ was found for the $\text{HfO}_2/\text{TiO}_x$ system and $140 - 160 \cdot 10^{26} \text{m}^{-3}$ for ZrO_x/Ta . Differences in the current compliance and higher switching voltages required for LSMO/HZO devices are likely to promote enhanced oxygen vacancy generation, thereby leading to higher concentrations than reported for the $\text{HfO}_2/\text{TiO}_x$ system. The Ta oxygen exchange layer in the ZrO_x/Ta system provides an additional source of vacancies by forming an interfacial TaO_x layer, therefore contributing to a higher vacancy density.

Ultimately, it must be emphasized that variations in filament size and conductivity are intrinsic characteristics of filamentary-type resistive switching. The variations determine device-to-device and cycle-to-cycle variability encountered in resistive switching devices [60]. Therefore, it is unrealistic to expect the definition of a definitive filament size or composition, and a significant degree of statistical spread must always be considered for filamentary switching phenomena.

Reduced Structures

The spotty structures in Figure 7.2a show a rigid shift of the Hf 4f spectrum to higher binding energies. The proposed interpretation of this observation is also a reduction of the HZO, but significantly weaker than in the filament, below the threshold of a Hf^{3+} component emerging. The oxygen vacancies serve as *n*-type dopants in the HZO, shifting the Fermi level towards the conduction band, which is observed as an increase in binding energy of the core-level electrons, as described in Section 3.5. Similar behavior has been observed before, for example, in $\text{Ta}_2\text{O}_{5-x}$ and other transition metal oxides [17, 103, 188]. The core-level shift, resembling oxygen vacancy-induced doping, is found in structures across the whole device area. This observation highlights the critical role that oxygen vacancies play in modulating the local electronic properties of the material, even in regions that are not directly involved in filament formation. The origin of these locally reduced structures is proposed to stem from intrinsic structural defects that possess a lowered formation energy for oxygen vacancies. Notably, features such as o-/o-phase grain boundaries, residual paraelectric m-/o-phase boundaries, or t-/o-phase interfaces are known to facilitate vacancy formation [124–126]. Although from XRD characterization, no significant monoclinic phase fraction is observed in the LSMO/HZO system with an 8 nm HZO layer, as it was used here (Figure 4.3). This absence of detectable monoclinic content could plausibly be attributed to the limited coherence length associated with nanoscale phase fractions, rendering them undetectable by conventional XRD. Furthermore, surface topography investigations revealed no micrometer-scale features on the HZO surface that could influence the XPEEM measurements (Section 4).

The conductivity variations within pristine HZO that were identified via C-AFM in Figure 4.5 support inherent structural variations as an origin of preferential oxygen vacancy paths. The lateral dimensions of the regions that showed an elevated conductivity are comparable to both the filaments and the substructures that can be identified within the reduced regions (Figure 7.2b).

Further supporting the proposed structural origins of local electronic variations, the PFM measure-

ments of HZO, as discussed in Section 6.1, confirm a similar size range as the reduced structures. Specifically, domain sizes between 10 nm and 150 nm were observed, with the larger domains found when measured through a top electrode. Previous reports in the literature have documented grain and domain sizes of ferroelectric HZO thin films that are similarly within this range [129–131]. It can be assumed that the filament responsible for resistive switching formed at one of such preferential conductivity paths that emerge along structural defects. This finding highlights the complex interplay between structural, ferroelectric, and electronic properties in nanoscale ferroelectric oxide systems.

During resistive switching, Joule heating accelerates the vacancy migration, and a substantial reduction occurs when switching into the LRS [57]. This distinguishes the filament responsible for the switching from other preferential current paths, which remain comparably weakly reduced. The abundance of potential preferential paths highlights the inherent cycle-to-cycle variability of filamentary-type resistive switching [60, 177].

7.1.3 Shifts Near Needle Contact & Other Observations

When investigating the conductive filaments responsible for resistive switching, a particular focus was placed on delamination-type devices. Their comparatively simpler structure results in significantly fewer artifacts unrelated to the switching process, facilitating a more direct analysis. In the following, additional findings are presented that, despite not directly identifying a filament, provide further insights into the system.

Figure 7.4a shows a delamination sample that was switched with -8 V and +5 V and kept in the LRS for XPEEM investigation (MAXPEEM, MAXIV, Lund). This Hf 4*f* image shows a clearly visible remaining artifact from contacting the device with a needle. The scratch is primarily undesirable, as it introduces topographical irregularities that can distort the XPEEM measurements. Additionally, its presence indicates damage to the Au top electrode during the biasing process, potentially exposing the oxide surface to air and promoting the re-oxidation of an already-formed filament. However, it also presents an advantage, as it increases the likelihood of detecting electro-chemical changes associated with localized switching at or near the affected area. Colored circles highlight several regions of interest, from which the Hf 4*f* spectra in Figure 7.4b are extracted. The spectra are normalized to the maximum, and an offset is subtracted.

The most straightforward feature to analyze is the purple region. This area appears brighter at higher binding energies, and its spectrum exhibits a small, rigid shift toward higher binding energies compared to the reference in blue. It is reasonable to assume that this corresponds to a similar phenomenon as the spotty structures previously observed in the graphene *operando* device (Figure 7.2a).

The red and green regions correspond to the scratch. Both appear dark at higher binding energies, but the zoom-in at lower binding energies reveals sub-structures within. The spectra for both regions exhibit a shift toward lower binding energies, with the center of the scratch (green) showing a more pronounced shift than the edge (red). No broadening compared to the reference is visible,

excluding a sufficiently high oxygen vacancy concentration to cause the emergence of a suboxide. Previously, rigid peak shifts were interpreted by doping via oxygen vacancies below the threshold for suboxide formation. Following this, the observed reduction in binding energy would indicate a decrease in oxygen vacancy concentration. However, it appears unintuitive that the red and green regions are in equilibrium locally more oxidized than the general device area, which is represented by the reference spectrum in blue and found at higher binding energies.

An explanation can be found in Lackner et al., who investigated ZrO_2 with XPS, finding a binding energy difference between monoclinic and tetragonal films [189]. The tetragonal film was found at higher binding energies despite both films showing only the Zr^{4+} state and no suboxide. This is explained by the stabilization of the tetragonal phase via oxygen vacancies rather than by a change in the bandgap. Following the same mechanism as described before, n-type doping by positively charged oxygen vacancies shifts the Fermi level closer to the conduction band, resulting in higher binding energies of the measured core-level.

This finding offers a possible explanation for the core-level shifts related to the scratch in Figure 7.4a. Filamentary switching is closely tied with Joule heating, which could possibly enable a local phase change from tetragonal/orthorhombic to monoclinic HZO in its vicinity. It is further plausible that also the filament itself re-oxidizes into the monoclinic phase if oxygen can be provided (e.g., by the damaged top electrode) and, therefore, does not show a suboxide in the center of the spot but rather a rigid shift to lower binding energies, which is tied to oxidation beyond the reference. An emerging monoclinic phase upon filamentary switching has indeed been found before by Zhang et al. They identified a monoclinic shell around the conductive Hf_6O filament in the LRS of Pt/a- HfO_2 /Pt device via high-resolution transmission electron microscopy [183]. They found that Joule heating during the SET induced a crystallization of a- HfO_2 into m- HfO_2 surrounding the filament, which then turned into t- HfO_2 when the filament ruptured during the RESET. An immediate comparison to their results can not be drawn here since the purely metallic electrodes and the different biasing (electroforming and current compliance) definitely impact the switching. Further, the oxygen vacancy dynamics are clearly different in the amorphous switching layer compared to the already fully crystalline thin film investigated here. The findings regarding filament stoichiometry in Section 7.1.2 also do not support a near-metallic filament. Nevertheless, this study provides a good foundation to consider a phase change towards the monoclinic phase as a potentially relevant process taking place during filamentary switching.

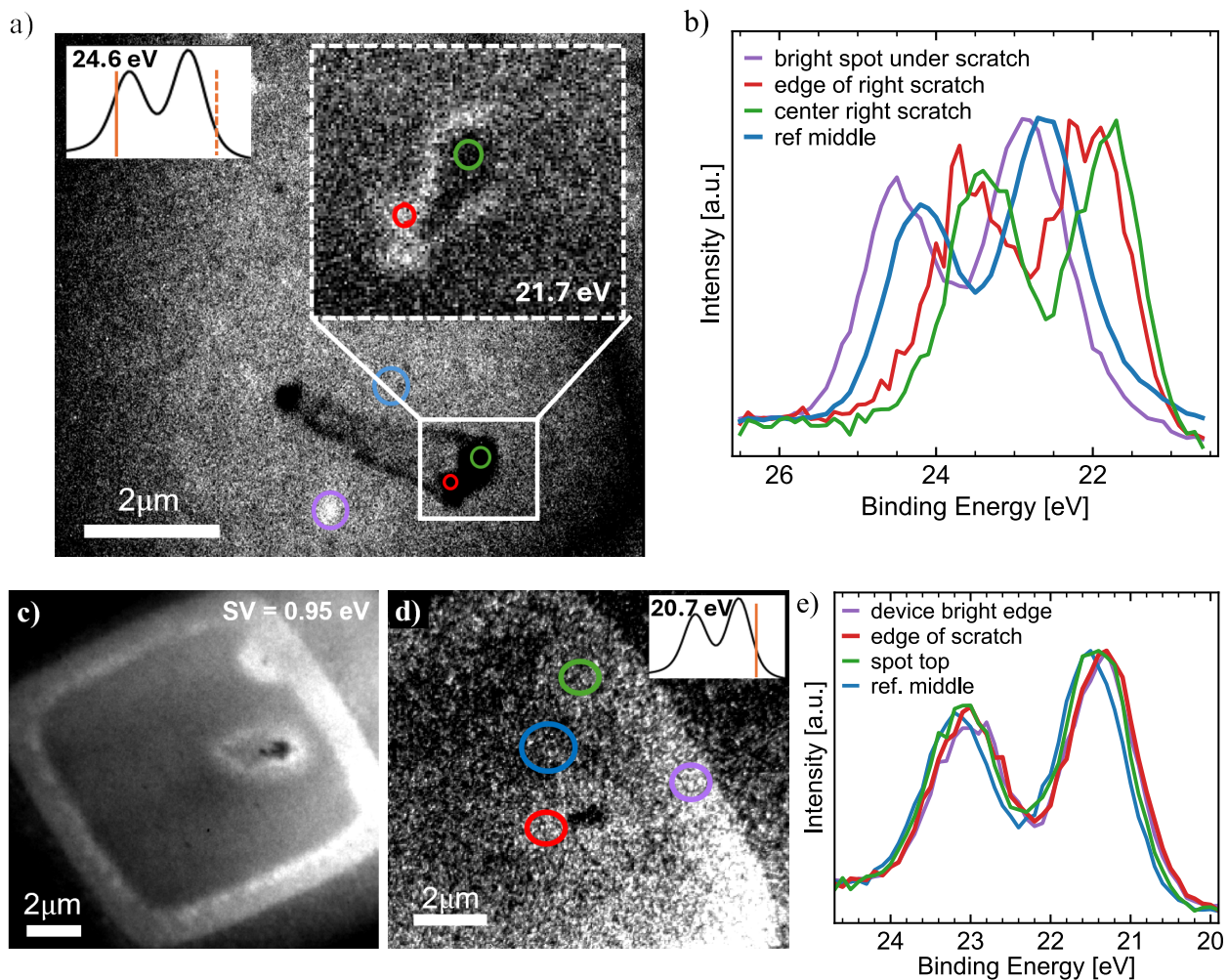


Figure 7.4: a) XPEEM Hf 4f image of a delamination device in the LRS revealing several features. A zoom-in of part of the scratch reveals a sub-structure. Regions from which spectra are extracted are marked with colored circles. The image was taken at a binding energy of 24.6 eV and the zoom-in at 21.7 eV. b) Hf 4f spectra of the regions marked in a). A background is subtracted, and data is normalized to the respective peak maximum. The right side is cut off due to the right shift. c) Image of work function scan of another delamination device in the LRS, taken at a start voltage of 0.95 eV. Due to the higher sensitivity of the photoelectron threshold to various effects, including chemical and topological differences, the image gives an improved overview of the device. d) Hf 4f image of the top right of the device in c), extracted at 20.7 eV. Colored circles mark the regions of interest, from which spectra are extracted. e) Hf 4f spectra of the regions marked in d). The background is subtracted, and the data is normalized to the respective peak maximum.

An alternative explanation for the observations, without invoking a phase change, is to reconsider the assumption that the general device surface is fully oxidized. Since the device was switched into the LRS by applying a negative voltage to the top electrode, this could have led to the non-localized attraction of a small concentration of oxygen vacancies to the surface, remaining insufficient for

a suboxide formation, similar to observations that will be discussed at a later point for HAXPES experiments.

If the reference spectrum corresponds to a slightly reduced state, then local oxidation at the switching site (red and green) becomes plausible. This could be facilitated by the heat generated during switching and the availability of oxygen through the damaged electrode. Opposing this interpretation is the fact that the observed shifts are significantly more pronounced than those in the HAXPES experiments. More importantly, the spotty reduced structures have already been identified as intrinsic preferential oxygen vacancy pathways, which become visible in XPEEM measurements (Figure 7.2a). It is therefore unlikely that a slight reduction could occur in such a homogeneous manner that no signatures of the inherent conductivity variations of HZO become visible. Consequently, a phase transition seems to be the more plausible explanation. It should nevertheless be noted that PEEM measurements exhibit inherent challenges regarding topographical effects, which can distort the spectra. However, this scenario appears less likely due to the absence of directional "shadows" cast from the feature, showing as reduced intensity.

Another exemplary delamination device, Figure 7.4c-e was switched with -6 V and +3 V and additionally with -10 V and +5 V with the intention to create a more severely altered switching area, willingly risking potential damage to the device. The device is then kept in the LRS for XPEEM investigation (Nanospectroscopy, Elettra, Trieste). As features are not well resolved in the Hf 4f measurement, Figure 7.4c shows the workfunction scan as an overview. The work function measurement, despite exhibiting contrast in the photoelectron threshold, is not employed for further analysis. This is decided based on the higher sensitivity of the photoelectron threshold to multiple factors, including chemical, electrical, and topological variations, making their disentanglement even more challenging than for the core-level spectra and, therefore, unfeasible.

The Hf 4f scan is evaluated at the top-right of the device, where two features can be seen. The colored circles in Figure 7.4d highlight regions of interest from which spectra are extracted. The key takeaway from this device is that, despite the more intense biasing, core-level shifts between the different features and the reference are generally less pronounced. One can further argue that the differences observed in Figure 7.4e are too minor to allow for a meaningful interpretation. This is likely due to the non-ideal preservation of the oxidation state in the LRS. As previously discussed, some degree of damage to the top electrode at the contact point is also likely in this case. This is particularly evident given that the very dark spot in the Hf 4f measurement exhibits a significantly reduced intensity, which likely results from contamination on the surface. Also noteworthy is the bright edge surrounding the device, observed in both the work function and Hf 4f measurements. This feature was consistently found in devices subjected to repeated switching cycles under high bias. A similar degradation of the device edge has been found in connection with a soft breakdown of the HZO by Long et al. [169]. A possible explanation is the alteration of the HZO/Au contact due to heat generation at the contact point and edges, where the field distribution differs. This is further supported by the spectra of those two regions behaving similarly with respect to the reference (red and purple in Figure 7.4e). The right shift beyond the reference spectrum in blue also suggests the possibility of a phase transition toward the monoclinic phase as a consequence of heat development. However, this effect is likely less pronounced than in Figure 7.4b, due to the

less localized impact by additional involvement of the device edge.

Another distinct feature (green), located outside the needle contact spot, nearly resembles the reference spectrum. Although the observed difference is minor, the spectrum appears slightly broadened, with a more shallow valley between the $7/2$ and $5/2$ peaks. This subtle deviation may indicate the presence of a small suboxide contribution from a former or very weak filament, which has likely undergone a certain extent of re-oxidation due to its proximity to the altered device edge.

In conclusion, the re-oxidation of switching-related changes on the oxide surface appears to be a crucial problem with delamination devices despite the *in-situ* top electrode delamination. This can originate from the extended time between switching and XPEEM measurement or the exposure of the oxide surface to air, due to damage to the Au top electrode. A trade-off arises between the careful treatment of the device to limit any damage, risking a filament at the lower resolution limit, and, on the other side, extensive biasing to maximize the potential electro-chemical changes in the HZO, which can cause damage, inhibiting the proper identification of such changes.

The findings of Figure 7.4 suggest that the needle impact and Joule heating-related damages should rather be avoided, as they render the filament identification near impossible, either by their overshadowing appearance or by facilitating the filament re-oxidation. A careful treatment, with the increased risk of no identifiable filament but also significantly fewer artifacts, should be preferred for future XPEEM experiments on delamination samples.

Regarding the emergence of monoclinic HZO in the filament vicinity, further evidence is required. Since the monoclinic phase of HfO_2 is the stable bulk phase, investigations by nano-XRD could be conducted on simpler *ex-situ* samples in future work.

7.1.4 SrO_x Segregation

A device of the graphene top electrode geometry was irreversibly switched to the LRS during XPEEM investigations. The corresponding I-V curve is shown in Figure 7.5c. During the Hf $4f$ measurement of the LRS, additionally, an arc severely damaged the sample, producing a thin layer of Au across the whole field of view. Consequently, the signal was dampened too much to identify variations in the Hf $4f$ image. Nevertheless, several obvious spots appeared that stood out bright in the Sr $3d$ measurement, see Figure 7.5b. The spectrum extracted exemplarily from the rightmost spot reveals a clear Sr $3d$ signature (Figure 7.5d), with the line shape resembling an oxide. The measurement of Hf $4f$ in the pristine state of the device, shown in Figure 7.5a, does not reveal any feature that could disclose the locations of the later appearing bright spots. Further measurements of Ti $3d$ and Mn $2p$ did not show any contrast, clearly identifying the spots as SrO_x . A hole in the HZO, through which the underlying LSMO bottom electrode is accessed, can be excluded. Considering that the SrO_x features were caused by the switching, involving especially much current flow due to the irreversibly lowered resistance, this leads to the assumption that the involved Joule heating caused the segregation to the surface.

Similar observations have been made during electroforming in crystalline STO, showing SrO protrusions near the filament site scaling with the applied current compliance [190, 191]. Further, SrO segregation was seen on LSMO under ultra-high-vacuum conditions [192].

Observing similar behavior on the HZO surface, through the HZO film, can be seen as an indication of the severe local temperature involved, in accordance with the permanent damage to the device. SrO_x features on a device's surface were not seen repeatedly in XPEEM investigations. Consequently, it can not be seen as a common failure mechanism of the LSMO/HZO material system. Nevertheless, it could motivate the use of a current compliance during the switching to limit the heat development, even if the LSMO usually serves as a sufficient series resistance during the general resistive switching operation.

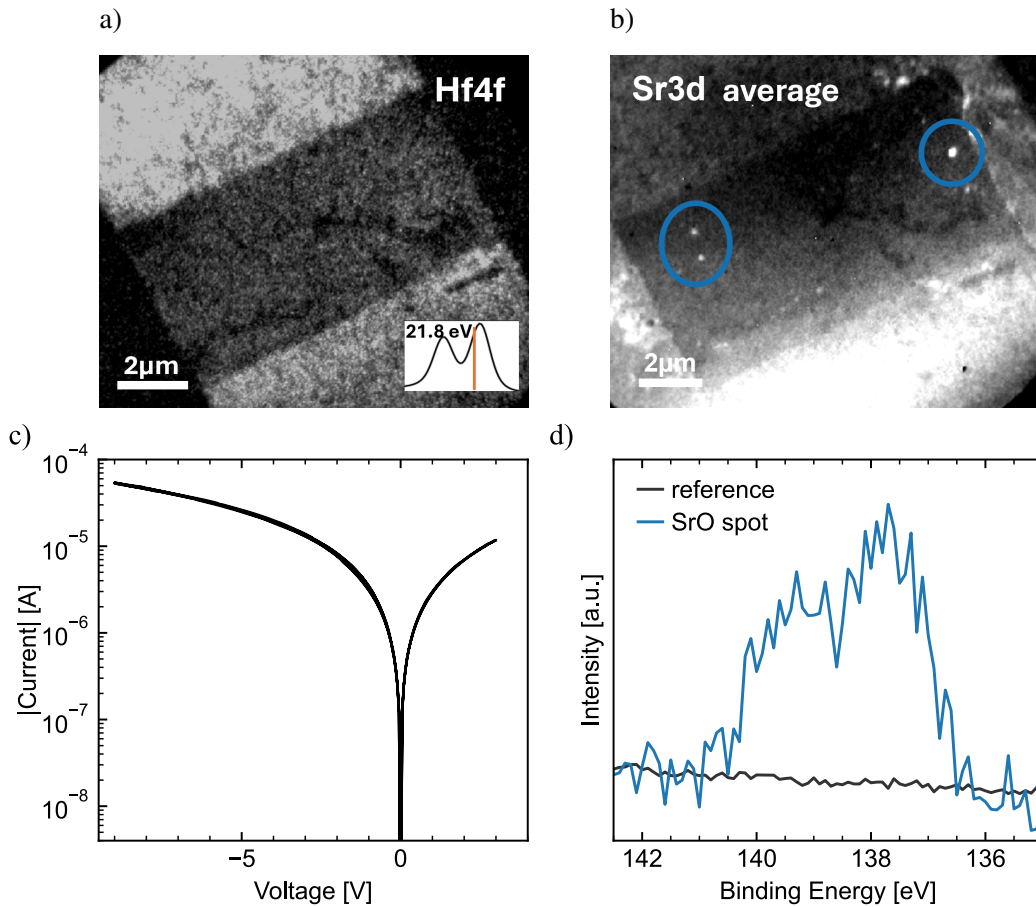


Figure 7.5: a) XPEEM Hf $4f$ image of a device in the pristine state, acquired at 200 eV photon energy. b) XPEEM Sr $3d$ image of a device in the LRS, acquired at 200 eV photon energy. The image is averaged over all binding energies. The blue circle highlights the newly appeared spots. c) Switching curve of the device into the LRS. d) XPEEM Sr $3d$ raw data extracted from the rightmost spot in b), in comparison with a reference obtained in the vicinity. The filament spectrum is of oxide-shape, justifying the interpretation as SrO_x segregation.

7.2 Hard X-Ray Photoelectron Spectroscopy - Ferroelectric Switching

To examine the dynamics of oxygen vacancies associated with the ferroelectric switching behavior of HZO, angle-dependent Hard X-ray Photoelectron Spectroscopy (HAXPES) measurements were carried out, specifically targeting the Hf $3d$ and Mn $2p$ core levels. The experiments were conducted at the GALAXIES beamline of the SOLEIL synchrotron radiation facility in France [104]. A photon energy of 6 keV was employed for all measurements, combined with a photon bandwidth of 0.8 eV and an analyzer pass energy of 200 eV. The incoming X-rays were horizontally polarized and aligned colinearly with the axis of the analyzer lens. Under these experimental conditions, the total energy resolution achieved was 0.814 eV. To probe different depths to extract qualitative information regarding both the top and bottom interfaces of the HZO layer, as well as within the LSMO bottom electrode, the photoelectron take-off angle was systematically varied between 20°, 45°, and 60° relative to the sample surface.

The devices investigated in this study share the common material system that is composed of STO/LSMO/HZO, featuring an ultra-thin Pt top electrode. Although HAXPES provides a substantially larger probing depth compared to soft X-ray techniques, minimizing the thickness of the noble metal top electrode remains essential to ensure sufficient signal from the buried ferroelectric and electrode layers. An elongated device shape is chosen to maximize the device area probed by the incident X-ray beam. Details regarding the sample fabrication and device geometry can be found in Section 5.2.1.

The *operando* experiment design by *in-situ* ferroelectric switching provides significant advantage by enabling repeated measurements on the same device in different states, effectively eliminating device-to-device variability. The switching is performed using a noble metal top electrode and at a switching frequency of 1 kHz, as commonly employed in the standard operation of ferroelectric capacitors. As such, the conditions are highly representative of typical device operation, in contrast to alternative techniques such as PFM or C-AFM, where switching is locally induced through a biased scanning probe tip. An additional advantage of the *operando* design is the minimized delay between electrical switching and spectroscopic characterization. Because the HAXPES measurement is performed immediately following the electrical bias, the influence of time-dependent phenomena, such as oxygen vacancy drift due to the depolarizing field within the device, can be considered negligible. This ensures that the observed electro-chemical changes are directly linked to the ferroelectric switching, not superimposed by relaxation or degradation effects.

Measurements were conducted on the same device under several electrical states: its pristine condition, both polarization orientations, and a fatigued state induced by $>10^6$ switching cycles. The polarization switching of the devices was performed *in-situ*, and the devices remained electrically grounded throughout the HAXPES acquisition to prevent charging effects. A comparison between *in-situ* and *ex-situ* current responses following a standard PUND (Positive-Up Negative-Down) pulse sequence is presented in Figure 7.6. Due to the necessity of matching the device size with the spatial footprint of the incident X-ray beam, the devices were fabricated with a significantly larger

area than typical test structures. While this enhances the signal-to-noise ratio in photoemission, it also leads to increased leakage currents, which can obscure the ferroelectric contributions to the measured current. Consequently, a dynamic hysteresis measurement is insufficient to conclusively demonstrate ferroelectric switching in these devices. Moreover, the applied voltage was intentionally kept below a maximized ferroelectric response to minimize the risk of unintended resistive switching of the devices, which is increasingly likely for larger devices. This leads to weakly pronounced, incomplete switching current peaks during ferroelectric switching. Nevertheless, when analyzing the current transients associated with the PUND sequence, a clear distinction can still be observed between switching and non-switching pulses in the *ex-situ* measurements. In contrast, the *in-situ* switching response exhibits a higher baseline noise and a more subtle difference between switching and non-switching pulses, visible at approximately $0.5 \cdot 10^{-4}$ s, despite the higher applied voltage.

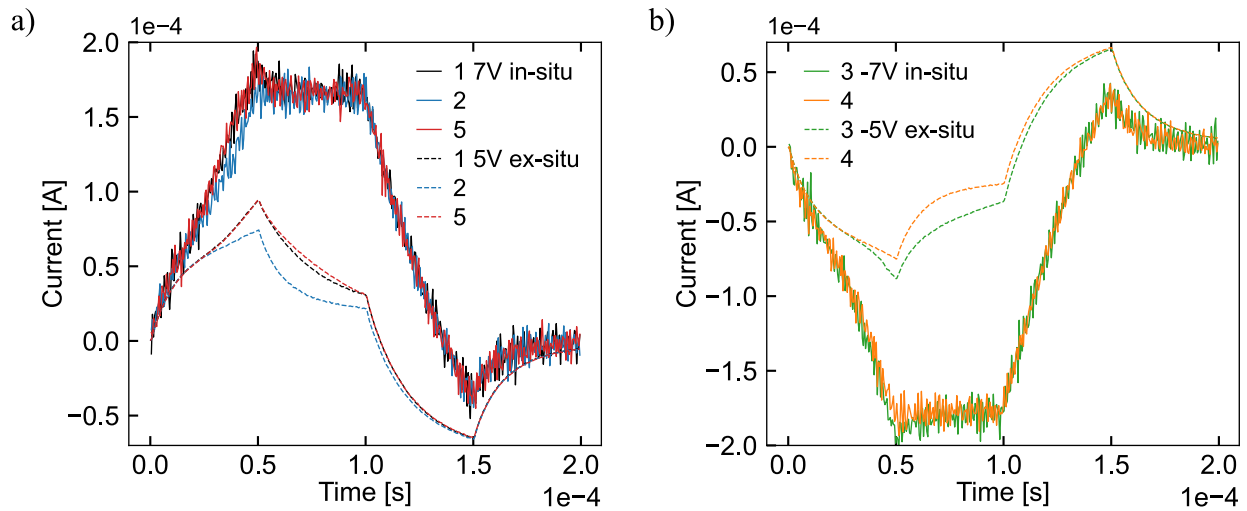


Figure 7.6: Ferroelectric PUND measurements of STO/LSMO/HZO/Pt *operando* devices. a) Comparison of the switching (1 & 5) and non-switching (2) current response *in-situ* and *ex-situ*, at +7V and +5V applied, respectively. b) Comparison of the switching (3) and non-switching (4) current response *in-* and *ex-situ*, at -7V and -5V applied. Reprinted with permission from [134].

The differences between *in-* and *ex-situ* switching behavior can largely be attributed to the extensive additional connections and wiring required for *in-situ* addressing of the devices in the HAXPES chamber. Electrical connections from the device pads to the sample holder are established via wire bonding, and further connections are involved to enable electrical biasing via the external ferroelectric tester. This additional wiring, while necessary, introduces parasitic resistances and capacitances that can distort the high-frequency I-V response of the system, also justifying the need for increased driving voltages during *in-situ* switching.

Despite being less pronounced, the presence of ferroelectric switching can still be confirmed by the characteristic difference between switching and non-switching pulses of the PUND measurement (see Section 6.1 for details).

7.2.1 Stability under radiation

To validate that the HAXPES measurement process itself does not induce any radiation-related changes in the sample, repeated Mn $2p$ spectra were acquired. This spectrum is chosen due to the relatively higher susceptibility of LSMO to reduction compared to HZO and improved visibility of valence changes in the Mn associated with its mixed-valence character [123]. Figure 7.7 presents a comparison between the initial Mn $2p$ spectrum and a subsequent spectrum acquired after a continuous exposure period of 1 hour and 40 minutes. Both spectra were normalized, and a linear background subtraction was applied. No significant variations are observed, particularly no indications of spectral shifts or peak asymmetry that would suggest a chemical reduction due to radiation-induced damage. These findings confirm the stability of the sample under the applied HAXPES measurement conditions and support the reliability of the data presented throughout this study.

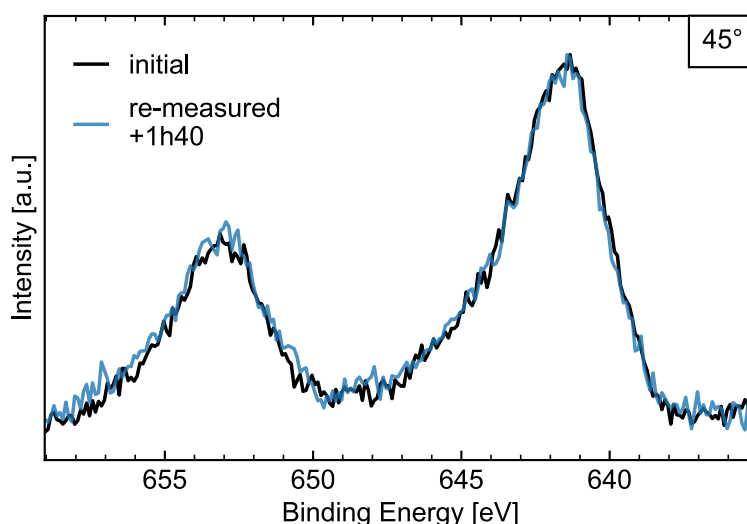


Figure 7.7: Mn $2p$ core-level spectrum, measured repeatedly. The comparison of the initial spectrum with the repeated measurement after 1 h 40 min demonstrates no alternation of the core-level spectra due to the hard X-rays. Spectra were normalized, and a linear background was subtracted. Reprinted with permission from [134].

7.2.2 Hf $3d$ vacancy profile

All Hf $3d_{5/2}$ spectra were analyzed using the *KolXPD* fitting software. A Shirley-type background was subtracted from each spectrum, and the photoemission peaks were modeled using Voigt profiles. The peak shape and full width at half maximum (FWHM) were held constant for all spectra recorded at the same take-off angle to maintain consistency across different states. In cases where a suboxide component was justified, a corresponding peak was included in the fit, and its

energy separation from the main Hf^{4+} oxide peak was fixed at 0.83 eV. As a reference point for energy calibration, the Pt $4f_{7/2}$ core-level peak from the top electrode was recorded in every device state and at each take-off angle. The peak was modeled using a Donjach–Sunjich line shape and corrected to a binding energy of 71 eV to align the binding energies of all measured spectra.

Figure 7.8a shows an overlay of all measurements of the Hf $3d_{5/2}$ peaks for all four device states at a take-off angle of 20° , which corresponds to the shallowest probing depth. Depending on the state of the device, differences in peak positions can be observed, as highlighted in the zoom-in of the peak maximum.

In Figure 7.8b-d the detailed measurements of the Hf $3d_{5/2}$ peak are displayed. Each figure corresponds to one take-off angle at which the device is measured in all states. Shown is the measurement as squares and the peak fit as a line. For visual reference, the peak position of the pristine state is indicated in each plot by a dashed grey line

From the zoom-in in Figure 7.8a it becomes clear that the fatigued state is not only shifted to lower binding energies, similar to the P_{down} state in purple, but also broadened to align with the other states on the higher binding energy side, suggesting the presence of an additional spectral component. This is confirmed by the peak fitting of all Hf $3d_{5/2}$ peaks, where the fatigued state cannot be adequately described using a single symmetric Voigt function. Instead, inclusion of a second component associated with Hf^{3+} suboxide provides a good agreement of the fit with the measurement, as seen in Figures 7.8b–d.

The spectra corresponding to the other states do not exhibit sufficient asymmetry or broadening to justify the inclusion of a suboxide component; the measurements can be well described using only the symmetric Voigt peak attributed to the stoichiometric Hf^{4+} oxide.

To enable a quantitative evaluation of the observed binding energy shifts, the fitted peak positions extracted from Figure 7.8 are summarized for each device state and take-off angle in Figure 7.9, labeled as device #1. The complete measurement set was repeated for a second, equivalent device #2. The results obtained from both devices exhibit consistent trends, thereby confirming that the observed binding energy shifts, although subtle, are representative and reproducible features of the LSMO/HZO system under equivalent electrical treatment. The plotted data are arranged such that the information depth within the HZO layer decreases from left to right, corresponding to take-off angles of 60° , 45° , and 20° , respectively. In the case of the fatigue state, the peak position of the Hf^{4+} component is used.

Consistent with the interpretation proposed for the reduced HZO regions identified in the XPEEM experiments and described in Section 3.5, the rigid shifts observed in the Hf $3d_{5/2}$ binding energy are attributed to changes in the local electronic structure caused by oxygen vacancy accumulation. Specifically, the introduction of oxygen vacancies leads to n-type doping, which shifts the Fermi level upward with respect to the core levels. In photoemission, this translates to an apparent increase in core-level binding energy, which can be interpreted as a weak oxidation (lower vacancy concentration) or reduction (higher vacancy concentration) of the HZO material. The origin of the oxidation and reduction, leading to the shifts, is assigned to the applied voltage during ferroelectric switching. Application of a positive voltage to the Pt top electrode switches the device into the

P_{down} polarization state, while a negative voltage induces the P_{up} state. The polarization reversal is accompanied by oxygen vacancy migration, leading to shifts in the core-level spectra depending on the polarization and fatigue state of the device. A detailed discussion of the specific observations and their implications will be discussed in the following.

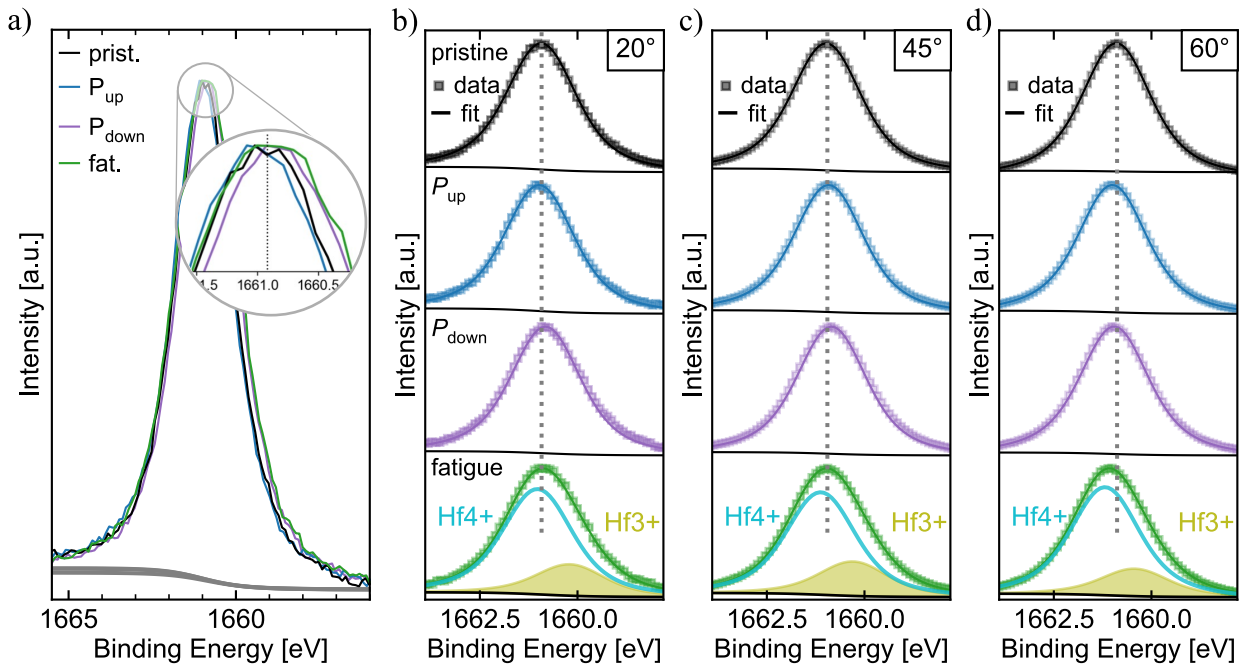


Figure 7.8: a) Overlay of HAXPES Hf $3d_{5/2}$ core-level spectra at 20° take-off angle, showing the measured data and Shirley background. The zoom-in of the peak maxima highlights subtle shifts depending on the device state. The grey dashed line marks the peak maximum of the pristine state. b) Hf $3d_{5/2}$ core-level spectra: Measurement (squares) and envelope of the corresponding fit (line) for all measured states at $\Theta = 20^\circ$. c) $\Theta = 45^\circ$ d) $\Theta = 60^\circ$. The grey dashed line marks the peak maximum of the pristine state to visualize peak shifts. The $\Theta = 60^\circ$ angle has the highest average information depth, while 20° corresponds to the lowest information depth. Adapted with permission from [134].

From the general behavior, a trend can be observed that binding energies tend to increase towards the more bulk-sensitive measurements. This is highlighted by the grey arrow in Figure 7.9. The pristine state in black clearly deviates from this trend, decreasing from 45° to 60° . This can be understood by oxygen migration from LSMO into the HZO at the bottom interface in the pristine state. This transfer is consistent with the difference in free energy gain between HZO and MnO and was already discussed in Section 4.

Following the pristine condition, exposure of the devices to repeated electrical field cycling leads to the emergence of a binding energy gradient across the HZO layer. This gradient becomes increasingly pronounced with continuous switching cycles, as it is most evident in the fatigued state. Notably, the fatigued spectra also exhibit the largest overall shift in binding energy toward

higher values, indicating a significant alteration in the local electronic structure. The observed binding energy gradient suggests a spatially non-uniform distribution of oxygen vacancies, with preferential accumulation near the interface between the HZO and the underlying LSMO electrode. This behavior is indicative of extensive vacancy pinning and with that, domain pinning at the bottom interface, which could be associated with the formation of a so-called "dead layer", a region with suppressed ferroelectricity [32, 193, 194]. Such interfacial effects are well known in ferroelectric thin films and can critically influence both switching dynamics and long-term device reliability. Given that ferroelectric fatigue is often attributed to oxygen vacancy generation and migration, the inhomogeneous reduction resembled by the gradient through the HZO thickness likely reflects a superposition of two effects: First, an increased overall concentration of oxygen vacancies, and second, a preferential localization of those vacancies near the bottom interface. Support for this interpretation is provided by the presence of a Hf^{3+} suboxide component in the fatigued $\text{Hf } 3d_{5/2}$ spectra (see Figure 7.8b–d). Although it should be noted that the suboxide contributions amount to approximately 17%, 25% and 23% for decreasing information depth, not resembling a similar gradient throughout the HZO thickness. Since only one device was measured in the fatigue state, it can not be confirmed whether the suboxide contributions follow a different trend than the peak shifts. Consequently, it is assumed that the contributions are approximately equal within reasonable measurement and peak fit accuracy.

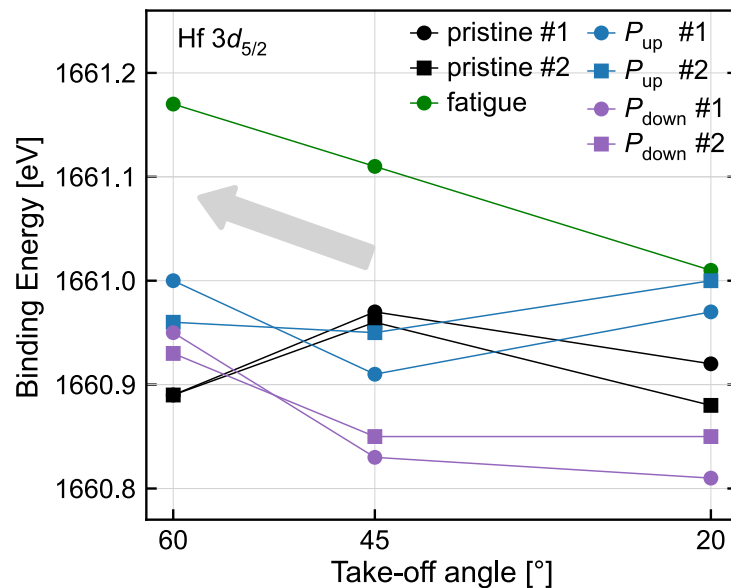


Figure 7.9: Binding energy positions of the fitted $\text{Hf } 3d_{5/2}$ peak for two equivalent devices (device #1 and device #2), measured independently in the pristine, P_{up} , P_{down} and fatigued state at three take-off angles. The average information depth decreases from left ($\Theta = 60^\circ$) to right (20°). Adapted with permission from [134].

Depending on the polarization direction, a shift of the HZO core levels can be found, resembling the migration of oxygen vacancies driven by polarization switching. A direct comparison of the

two polarization directions shows a clear difference in binding energy of about 0.15 eV at the most surface-sensitive take-off angle of 20°. This energy shift systematically diminishes towards the bottom interface. The consistently higher binding energies observed for the Hf 3d_{5/2} peak in the P_{up} state, relative to the P_{down} state, point to an increased level of n -type doping induced by oxygen vacancies. This is in agreement with the direction of applied voltage during switching, where a negative bias on the top Pt electrode (resulting in the P_{up} state) promotes the migration of oxygen vacancies into and toward the upper region of the HZO film. The observation that this difference diminishes toward the buried HZO/LSMO interface suggests a compensating mechanism, such as oxygen migration from and to the LSMO bottom electrode and/or the previously discussed possibility of a pinned layer near the LSMO interface.

The change in charge carrier concentration n due to the polarization reversal and continuous field cycling can be roughly estimated from:

$$n = N_C e^{\frac{E_F - E_C}{kT}}; \quad \Delta E_F = kT \ln\left(\frac{n_2}{n_1}\right); \quad \frac{n_2}{n_1} = e^{\frac{\Delta E_B}{kT}} \quad (7.2)$$

Where N_C is the density of states in the conduction band, E_F the Fermi energy, and E_C the conduction band edge. As discussed before, the shift in binding energies of the Hf 3d core-level originates from n -type doping, moving E_F closer to the conduction band minimum, therefore, increasing the binding energy. Consequently, a change in E_F can be approximated by the observed shift in the binding energy ($\Delta E_F \approx \Delta E_B$). At room temperature ($kT \approx 0.025$ eV), it follows that the switch from P_{down} to P_{up} (+0.15 eV at the surface, Figure 7.9) equals an increase in charge carrier concentration by a factor of $4 \cdot 10^2$. At the LSMO/HZO interface, the reduction from pristine to ferroelectric switching is an increase by a factor of $1.6 \cdot 10^1$, and the reduction from pristine to fatigue an increase by a factor of $1.1 \cdot 10^5$. Assuming that the increase in charge carriers solely originates from double positively charged oxygen vacancies, this can be translated to an increase by a factor of $2 \cdot 10^2$ between polarization directions at the surface and of $5.5 \cdot 10^4$ at the LSMO interface between pristine and fatigued. As expected, these changes are in significantly smaller orders of magnitude than the vacancy concentration of $78 \cdot 10^{26} \text{m}^{-3}$ resulting from the suboxide found in the filament region of resistive switching (Section 7.1.2).

7.2.3 Mn 2p vacancy profile

Complementary analysis was performed on the Mn 2p core-level spectra originating from the underlying LSMO bottom electrode. Due to the attenuation of signal with decreasing take-off angle, only the measurements conducted at 45° and 60°, Figures 7.10a and 7.10b, respectively, provided an adequate signal-to-noise ratio for interpretation. This is consistent with the limited information depth and surface sensitivity at 20°, which primarily probes the overlying HZO layer.

Across the different states, only minor deviations from the pristine condition are observed in the Mn 2p spectra. These subtle changes are highlighted by the dashed reference line, which indicates the peak maximum of the pristine state. Variations in the Mn 2p peak position can be interpreted in

terms of changes in the Mn^{4+} to Mn^{3+} ratio, providing insight into valence changes of the LSMO. Although rigid shifts, such as those seen in the Hf core-level, could in principle be superimposed on valence changes, they are not considered here. This is due to noticeable differences in peak shape, leaving a valence change as the more obvious interpretation. The interpretation of additional rigid shifts would further be extremely challenging, considering the inherent mixed-valence character of the Mn $2p$ peak.

A shape change in the Mn $2p$ peak maximum toward higher binding energies is indicative of a relative increase in the Mn^{4+} valence state, whereas a change toward lower binding energies corresponds to a higher fraction of Mn^{3+} [195]. At the intermediate take-off angle of 45° , the P_{up} state exhibits a clear change to higher binding energies relative to the pristine reference. In contrast, the P_{down} state reveals only a marginal, if any, change in the same direction and only for $\Theta = 45^\circ$. This behavior resembles an oxidation of the LSMO in the P_{up} state as the counterpart to the reduction identified in the Hf $3d$ spectra. At the more bulk-sensitive take-off angle of 60° , the magnitude of the difference in the P_{up} state is reduced, and the other states exhibit negligible changes with respect to the pristine state. The reduced effect at this larger angle suggests that the HZO-induced chemical modifications in the LSMO are primarily localized at the interface region, with minimal impact on the bulk LSMO.

Interestingly, the fatigued state closely resembles the pristine state. This observation implies that, despite the increased oxygen vacancy concentration and the emergence of a Hf^{3+} suboxide phase within the HZO layer under repeated field cycling, no substantial increase in the Mn^{3+} fraction occurs in the LSMO electrode. Instead, a minor change toward higher binding energies may be present in the fatigued state at $\Theta = 45^\circ$, similar to the P_{down} state.

Difference spectra of the Mn $2p$ measurements in Figure 7.10a and 7.10b with respect to the pristine state are shown in Figure 7.10c and 7.10d, respectively, to verify the aforementioned observations. All spectra are normalized to the maximum, and a linear background is subtracted. The pristine state spectrum is shown directly; all other spectra are shown with the pristine spectrum subtracted, to highlight the differences.

At 45° , all spectra show a similar deviation, consistent across the Mn $2p_{1/2}$ and Mn $2p_{3/2}$ peaks, only varying in magnitude between the different states. Considering the signal-to-noise ratio, a clearly higher intensity at higher binding energies and therefore, higher relative Mn^{4+} than in the pristine state is visible for the P_{up} state and to a smaller extent also for the P_{down} state, confirming the observations found before. At 60° , the differences to the pristine state are less coherent across the spin-orbit splitting. Nevertheless, an intensity reduction at lower binding energy, which resembles a relative reduction of Mn^{3+} , seems likely.

Overall, the trends observed in the Mn $2p$ core-level spectra suggest that the LSMO bottom electrode exhibits a saturated reduction already in the as-fabricated pristine state. Subsequent electrical treatment, including both the application of positive bias associated with the P_{down} state and extended field-cycling leading to fatigue, does not result in substantial deviations from this initial state. This invariance in the Mn core-level supports a limited influence of the vacancies in HZO on the LSMO. The data point toward a restriction to the interfacial region, with minimal penetration

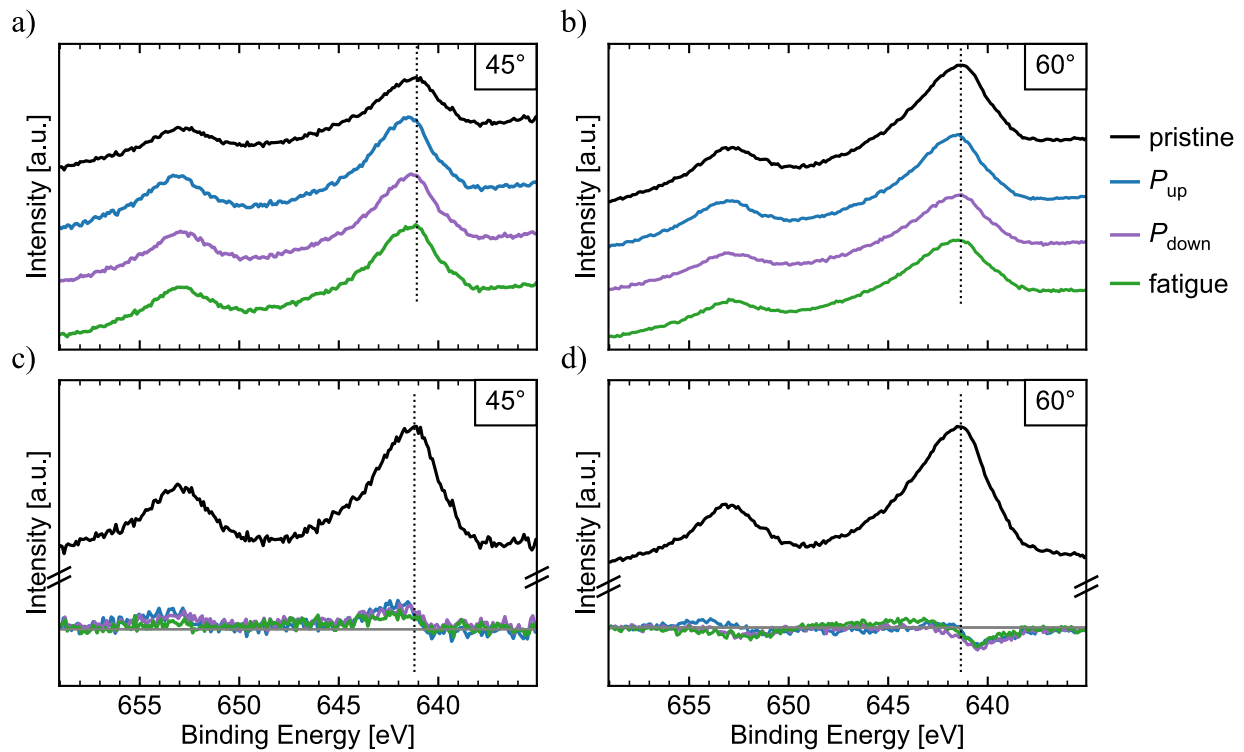


Figure 7.10: HAXPES Mn $2p$ spectra measured in the four different states, at a) $\Theta=45^\circ$ and b) 60° (highest information depth). As a guide to the eye, the dashed line indicates the peak maximum of the pristine state in the respective graph. c) The pristine measurement is subtracted from the other states' spectra to highlight changes at $\Theta = 45^\circ$ and d) $\Theta = 60^\circ$. The dashed line indicates the pristine peak maximum as a guide to the eye. Adapted with permission from [134].

of vacancy-driven redox effects into the bulk of the LSMO bottom electrode.

The HAXPES data on Mn differences depending on the polarization state of the HZO is supplemented by an attempt to probe the same states via XAS on delamination-type samples. The measurements were performed during the XPEEM investigations at the Nanospectroscopy beamline, Elettra, Trieste, see Section 5.1.1 and 7.1.

Figure 7.11 shows the XAS measurement of two different devices that were switched into P_{down} and P_{up} polarization, *ex-situ*. The data is background corrected by a linear fit of the pre-edge and normalized by a polynomial fit to the post-edge using *Athena*. The different devices were found to exhibit a significantly different background, together with a short data range in the post-edge region. This leads to a challenging normalization, as evident from the deviations at the higher photon energy end.

The Mn L_3 -edge appears similar for both states, while the L_2 -edge shows a difference in peak position. A shift of the L-edges to higher energies is associated with a higher valence state of the Mn [196]. Consequently, the observed right shift of the P_{up} state is in line with the previous findings from the HAXPES measurement that indicated an oxidation of the LSMO in conjunction with the

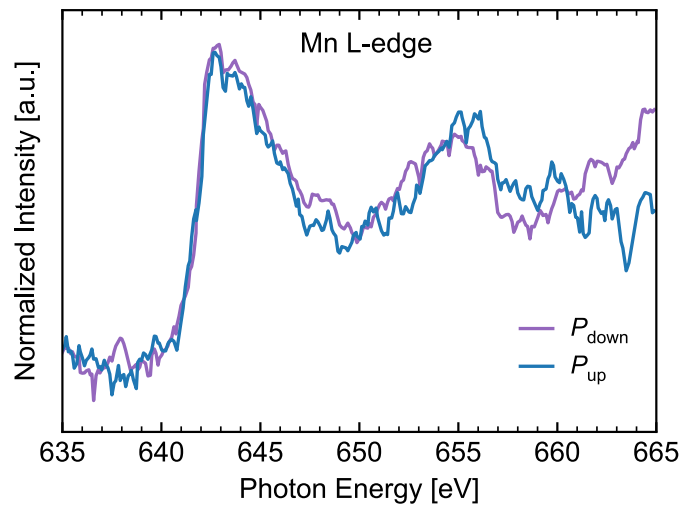


Figure 7.11: XAS measurement of the Mn L-edge of devices with delaminated top electrode, measured during the XPEEM investigations in Section 7.1. Two different devices were switched into opposite polarization direction, *ex-situ*. Spectra are normalized and background corrected with *Athena*.

reduction of HZO in the P_{up} state. However, it should be emphasized that the absence of a similar change in the L_3 -edge and the significant differences at high energies leave conclusions from the XAS data questionable. Among possible sources that could have impaired the measurement are the *ex-situ* experiment design, which imposes an extended time between switching and measurement. The impact of the depolarizing field could have possibly mitigated electro-chemical changes due to the polarization state. Furthermore, the XAS allows for a larger information depth. Subtle changes in the LSMO that are expected mostly at the interface with the HZO might not be detectable when much of the information stems from deeper regions of the LSMO.

Finally, the XAS measurement of both polarization directions possibly supports the HAXPES findings, although with quite limited significance.

7.2.4 Summary

The spectroscopic analysis of the ferroelectric switching-induced modifications in both HZO and LSMO indicates that, while oxygen exchange between the ferroelectric and the bottom electrode does occur, the majority of the generated oxygen vacancies remain confined within the HZO layer. These vacancies appear to accumulate preferentially near the bottom interface, as demonstrated by the observed binding energy gradient in the Hf $3d$ core-level spectra, Figure 7.9. These findings show partial agreement with prior studies, such as that by Nukala et al. [35], which identified oxygen-deficient re-ordering in $\text{La}_{0.67}\text{Sr}_{0.33}\text{MnO}_3$ adjacent to rhombohedral HZO under ferroelectric switching at 1 kHz. Notably, their observations differed under prolonged DC bias, which led to oxygen depletion across the entire LSMO layer. In contrast, the results of this work suggest that under realistic switching conditions, the oxygen vacancy redistribution remains localized and does not significantly penetrate into the bulk of the LSMO electrode, even in fatigued devices.

The findings support the interpretation that the inherent degradation of ferroelectric switching in the LSMO/HZO system is primarily driven by domain pinning, which can be attributed to charge trapping at oxygen vacancy sites [32, 125]. This mechanism differs from degradation pathways dominated by increased leakage currents or dielectric breakdown [193, 197]. While it can be expected that higher applied fields can partially reverse such degradation by promoting oxygen vacancy redistribution and de-trapping [198], these effects are likely temporary, given that the inhomogeneous distribution of vacancies seems intrinsically favored in the material system. Moreover, introducing a small fraction of the monoclinic phase has been shown to reduce domain pinning, albeit this can be expected at the expense of reduced ferroelectric performance [199].

The spectroscopic findings regarding ferroelectric switching are consistent with those reported by Hamouda et al., who observed an increase in oxygen vacancy concentration near the surface of TiN/HZO/TiN capacitors following electrical cycling, as revealed by XPEEM measurements [42]. However, a direct comparison of polarization-state-dependent vacancy distributions is not possible due to fundamental differences in experimental conditions. In particular, their longer (non-*operando*) timescales, during which the internal depolarizing field may induce significant vacancy redistribution, complicate the interpretation of the polarization effects.

Contrasting results have been reported for ferroelectric capacitors employing IrO₂ electrodes, where an oxygen-rich interface was identified in HZO using depth-sensitive spectroscopy [200]. This difference is likely attributable to the expectantly different metal–oxide interface between the systems, where polycrystalline HZO was sputtered onto a IrO₂ electrode, in contrast to the epitaxially grown LSMO/HZO heterostructure of this work. Furthermore, the difference in chemical behavior may be explained by the significantly lower oxidation potential of Ir compared to Mn, resulting in a reduced tendency for oxygen vacancy formation in the adjacent HZO [123].

A further comparison can be made with the work of Hill et al., who conducted angle-resolved HAXPES on epitaxial LSMO/HfO₂-based systems and reported polarization-dependent spectral variations. Their results similarly indicate an increased oxygen vacancy concentration in the HZO layer and a corresponding oxidation of the LSMO in the P_{up} state, whereas the P_{down} state remained spectroscopically similar to the pristine condition [43]. Despite this general agreement, an in-depth comparison remains limited due to critical differences in experimental methodology. Specifically, their use of PFM for electrical biasing and the corresponding presence of an exposed oxide surface, resulting in unscreened polarization charges and environmental adsorbates, both of which have been found to influence the core-level spectra.

7.2.5 Array-type Samples

In addition, *ex-situ* samples of the array-type layout (see Section 5.2.2) are investigated by HAXPES in different polarization and field cycling states, at the same take-off angles. The results are non-conclusive, but are nevertheless briefly described for the sake of completeness and demonstration of the experiment design.

Figure 7.12 demonstrates the ferroelectric switching of individual, exemplary devices within the

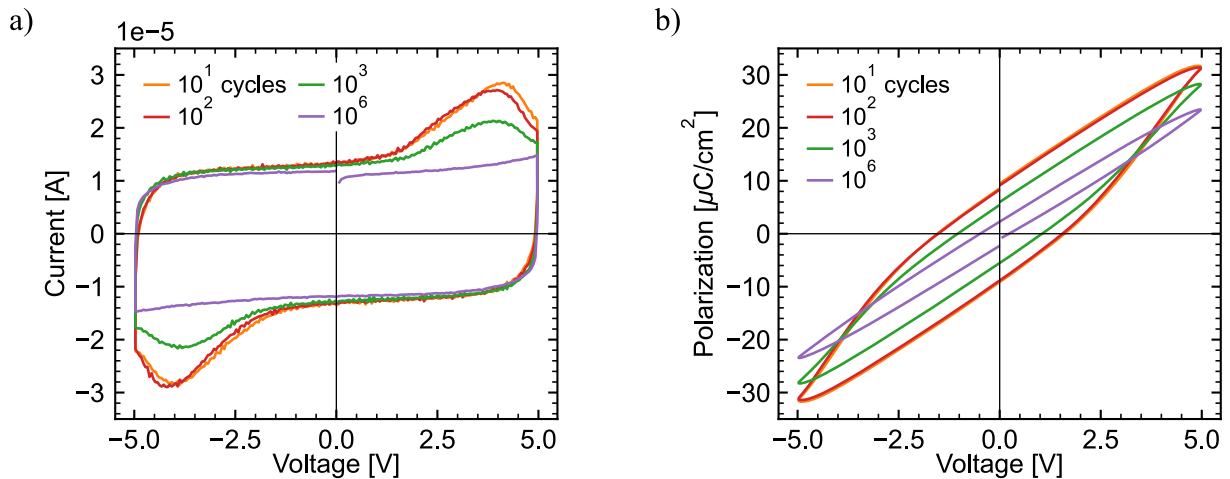


Figure 7.12: Ferroelectric switching of individual $2500 \mu\text{m}^2$ LSMO/HZO/Rh device within different investigated arrays. a) I-V and b) P-V loops measured after different extents of field cycling applied.

investigated arrays. Contrary to the *operando* devices, the smaller device size of here $2500 \mu\text{m}^2$ allows for hysteresis measurements, exhibiting the characteristic switching current peaks in Figure 7.12a and a hysteresis loop in Figure 7.12b. This further proves the feasibility of the ultra-thin Rh top electrodes that were used in this device geometry. The observed decrease of ferroelectric switching with increasing field cycling highlights the fatigue behavior, exhibiting no increase in leakage current and a vanished polarization at the latest 10^6 cycles.

Analogous to the analysis of the *operando* measurements, an overlay of the HAXPES Hf $3d_{5/2}$ core-level spectra at three different take-off angles is shown in Figure 7.13, 20° being the most surface sensitive measurement. All spectra are referenced to the rhodium Rh $3p_{3/2}$ peak of the top electrode, which is set to 497 eV, a linear background is subtracted where necessary. The field cycling of 10^1 cycles was done at ± 5 V, and that of 10^3 cycles at ± 6 V. The fatigued devices underwent 10^6 cycles at ± 5 V.

In Figure 7.13a, the only notable shift of the Hf $3d_{5/2}$ peak is for P_{up} and P_{down} after 10^1 cycles. The slight shift of P_{down} to higher binding energies and of P_{up} to lower binding energies matches the prior observations for the *operando* devices in Figure 7.9, where the same trend was observed. Considering the reduced comparability of the array-type results in comparison with the *operando* samples and the magnitude of the shift at 20° , suggests a too insignificant change. The measurements at 45° and 60° show major, unreasonable shifts in individual spectra despite the correction via the Rh $3p_{3/2}$ peak. This indicates complications during the measurement, limiting the validity of any conclusion drawn from spectra at these angles.

Overall, the array-type sample design did not produce viable results. A possible origin for the partial corruption of the spectra could be that the individual devices are floating in this geometry, opposed to the reliably grounded *operando* devices. A certain number of devices might additionally be connected to the bottom electrode via shortcuts, leading to alternating potentials across the beam footprint. Due to the geometry of the HAXPES setup, smaller detection angles are connected

to more vertical incoming x-rays and, therefore, a smaller beam footprint, possibly explaining the non-corrupted data at 20°.

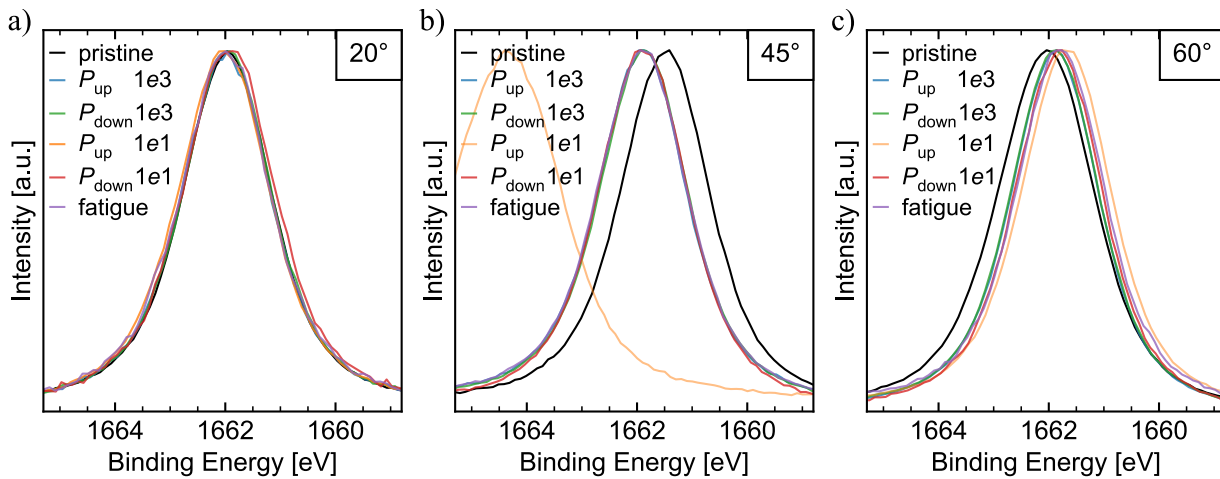


Figure 7.13: Overlay of HAXPES Hf $3d_{5/2}$ core-level spectra obtained from array-type samples in different polarization and cycling states. Taken at take-off angles of 20° in a), 45° in b) and 60° in c). A linear background is subtracted when necessary. A partial corruption of the data becomes obvious for 45° and likely for 60°, too.

In conclusion, *operando* sample design is strongly favoured for HAXPES investigations on ferroelectrics for multiple reasons. The very subtle shifts in the core-level spectra are easily overshadowed by, or confused with, device-to-device variability. Shifts might further be superimposed on ion re-migration due to the depolarizing field when devices are switched *ex-situ*, with extended time between switching and HAXPES measurement.

7.3 Dual-Mode Switching

The bipolar resistive switching and ferroelectric switching in the epitaxial LSMO/HZO system have been investigated by spectroscopical and microscopical methods. Both mechanisms involve oxygen reorganization; what distinguishes them is the biasing time scale and the spatial spread of the material region involved in the switching. Different experiment designs and device geometries were tailored to investigate the oxygen vacancy migration involved in the two switching mechanisms. XPEEM allowed to identify the filament site and spectroscopic footprint of filamentary VCM switching, which is induced by quasi-static biasing. Oxygen vacancy dynamics of ferroelectric switching upon an AC bias applied (kHz regime of voltage pulses) were identified via HAXPES. Small spectroscopic signatures of vacancy migration in the different polarization states, a reduction during fatigue, and an involvement of the LSMO were revealed.

Figure 7.14 summarizes the findings schematically. The determined oxygen vacancy distribution in the different states of both switching modes is illustrated by a color gradient in the LSMO and

HZO, where a more white region resembles a higher oxygen vacancy concentration. DC bias induces resistive switching by means of filamentary-type VCM switching. The generally stoichiometric HZO doesn't allow bulk vacancy movement or interface switching on DC time scales, as it was for example in $\text{La}_{0.67}\text{Sr}_{0.33}\text{MnO}_3/\text{r-HZO}$ or $\text{La}_{0.67}\text{Sr}_{0.33}\text{MnO}_3/\text{BaTiO}_3/\text{Pt}$ [35, 201]. Instead, accelerated by Joule heating [57], a localized path of oxygen vacancies forms along inherent structural variations of the HZO, such as phase or grain boundaries [8, 124, 202, 203]. The information depth of the XPEEM measurements does not allow access to the LSMO bottom electrode, preventing the detection of local chemical changes associated with the filament formation in the HZO. Nevertheless, a vacancy supply from the LSMO is strongly suspected, as sketched in Figure 7.14. Due to the stronger impact of the DC bias and the corresponding temperature development, a pronounced, local involvement of LSMO is expected.

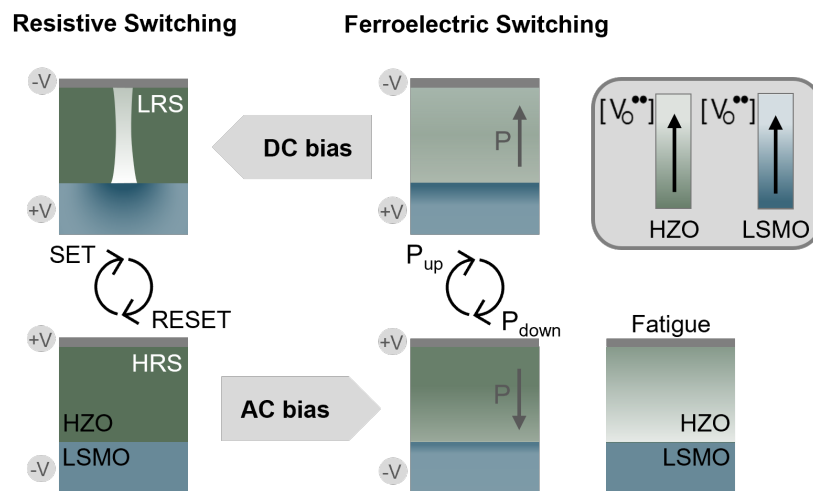


Figure 7.14: Schematic of the dual-mode operation and its electro-chemical implications for the different states in LSMO/HZO following the spectroscopic XPEEM and HAXPES investigations. The oxygen vacancy distribution and concentration in LSMO and HZO are indicated by the respective color gradient, where a whiter region resembles a higher oxygen vacancy concentration. Adapted with permission from [134].

During AC operation, HAXPES revealed small chemical changes associated with vacancy migration within the whole device area. Oxygen vacancies generally accumulate preferentially at the interface with the LSMO bottom electrode, which is joined by an overall reduction of the HZO upon field cycling. The vacancy distribution differs for the two polarization directions, resembling an attraction or repulsion due to the applied bias for switching, mostly confined to the top interface of HZO. This is joined by a complementary migration from and to the LSMO. However, the redistribution and vacancy generation are largely confined to the HZO, limiting the degradation during fatigue to the HZO.

Expectedly, the quantitative comparison of oxygen vacancies demonstrated significantly higher concentrations involved in filamentary switching than in ferroelectric switching. Between the polarization directions, an increase by a factor of $2 \cdot 10^2$ was found at the top interface. The

strongest change emerged at the bottom interface with a factor of $5.5 \cdot 10^4$ between the pristine and fatigued state. In contrast, the vacancy concentration in the filament was found to be $78 \cdot 10^{26} \text{m}^{-3}$.

Lastly, there were signs of potential local phase changes identified in response to filamentary switching. Intensely switched devices showed no clear sign of reduction at the probable point of impact, pointing towards a re-oxidation of the filament before the XPEEM measurement. Instead, localized spectral changes suggest the emergence of a monoclinic phase at the switching location or in close vicinity, likely induced by heat development during resistive switching. This could act as a permanent passivation of the former switching location, facilitating the restoration of the pristine device resistance in the HRS and impeding a re-formation at the same location. This mechanism would need to be investigated further, since the localized change to the non-polar monoclinic phase would ultimately corrupt the dual-mode operation by continuously reducing the ferroelectrically switchable area in the HZO.

8 Free-Standing $\text{Hf}_{0.5}\text{Zr}_{0.5}\text{O}_2$ Membranes

The experiments in this chapter were conducted by Lee-Kang Huang in the course of the master thesis *Phase stability and ferroelectric properties of epitaxial free-standing $\text{Hf}_{0.5}\text{Zr}_{0.5}\text{O}_2$ membranes*, RWTH, 2025.

Epitaxial growth of complex oxides requires substrates with closely matched lattice constants, crystal symmetries, and thermal expansion coefficients. These strict constraints limit the choice of materials and can result in challenges such as cation interdiffusion at high temperatures, high defect densities, formation of undesired phases, or high cost of suitable substrates. Furthermore, certain oxide materials may be metastable or chemically sensitive under standard growth conditions, making direct synthesis particularly challenging [204, 205].

To overcome these limitations, techniques have been developed that allow the detachment of epitaxially grown oxide films from their substrates. A possible fabrication path of such membranes is the chemical exfoliation, based on the use of a sacrificial buffer layer, that enables the release of thin oxide membranes, typically tens of nanometers thick, through selective etching of said sacrificial layer. This approach preserves the crystallinity of the membrane and permits its transfer onto a wide range of host substrates that are otherwise incompatible, including silicon, flexible polymers, or other oxide layers [205–207].

This opportunity is especially significant for the realization of device architectures where crystallinity, phase purity, and epitaxial orientation are essential but cannot be reliably achieved through conventional treatments such as post-annealing of amorphous films. The free-standing membranes can further be mechanically stretched, stacked in heterostructures with controlled twist angles, or used as platforms for subsequent epitaxial growth of other materials. By effectively decoupling the oxide film from its original substrate, this method unlocks novel material combinations and device configurations that are otherwise inaccessible through conventional epitaxial techniques. Consequently, the development of such free-standing oxide membranes presents potential for advancing functional oxide-based devices, particularly in the context of their integration with silicon technology, where often a strict thermal budget has to be maintained [207–209].

In the context of ferroelectricity, the material properties are closely linked to the presence of a polar phase. Especially in HfO_2 -based ferroelectrics, the stabilization of the metastable polar o-phase is heavily dependent on the exact conditions during growth or annealing, including the temperature

Substrate	Target	Laser fluence	Oxygen pressure	Temperature	Laser frequency	Cooling
STO	$\text{La}_{0.7}\text{Sr}_{0.3}\text{MnO}_3$	1.7 J/cm ²	0.24 mbar	750°C	5 Hz	-
STO/LSMO	HZO	1.5 J/cm ²	0.1 mbar	750, 800°C	2 Hz	200 mbar 10°C/min

Table 8.1: Growth parameters for pulsed laser deposition of STO/ $\text{La}_{0.7}\text{Sr}_{0.3}\text{MnO}_3$ /HZO heterostructures for membrane fabrication, grown in a different PLD system than in Section 4.

and cooling as well as the growth platform or chosen top electrode. All of which impose significant limitations when it comes to the compatibility with CMOS technologies or flexible electronics. The release of hafnia-based thin films from host substrates optimized for ferroelectric performance theoretically enables the integration with arbitrary substrates, including flexible and structurally dissimilar ones.

Zhong et al. have already demonstrated the fabrication of HZO membranes from the epitaxial STO/LSMO/HZO system. They found small phase changes after transfer onto SiO_2 and unchanged ferroelectric switching after bending on a flexible substrate [210]. Further, Shen et al. have achieved free-standing epitaxially grown HZO down to 1 nm thickness, retaining its ferroelectricity after transfer to a new substrate [122].

Here, the fabrication of free-standing HZO membranes is also demonstrated. Following the partly observed phase changes upon transfer in the literature, this is also investigated in this chapter, for a selection of established bottom electrode materials and several single-crystalline substrates of different lattice constants.

For the potential integration of the membranes into nanoelectronics or flexible devices, it is important to evaluate the stability limit of the ferroelectric phase in the membranes. This is evaluated by subjecting membranes to high temperatures on substrates with varying lattice constants. Further, the stability test upon bending is extended beyond the radius evaluated by Zhong et al. [210].

8.1 Fabrication

Epitaxial heterostructures of STO/ $\text{La}_{0.7}\text{Sr}_{0.3}\text{MnO}_3$ /HZO are grown by pulsed laser deposition as described in Section 4 and sketched in Figure 8.1a. As a different PLD system was used, the growth parameters were slightly adjusted, see Table 8.1. Further, it should be noted that the LSMO stoichiometry in this chapter is $\text{La}_{0.7}\text{Sr}_{0.3}\text{MnO}_3$ (LSMO30) in contrast to $\text{La}_{0.8}\text{Sr}_{0.2}\text{MnO}_3$ (LSMO20) which was used in all other experiments of this thesis.

A chemical wet etching technique is used to release the HZO thin film. In the course of that, the LSMO serves as a sacrificial layer between the substrate and the HZO, which can be chemically dissolved as illustrated in Figure 8.1b.

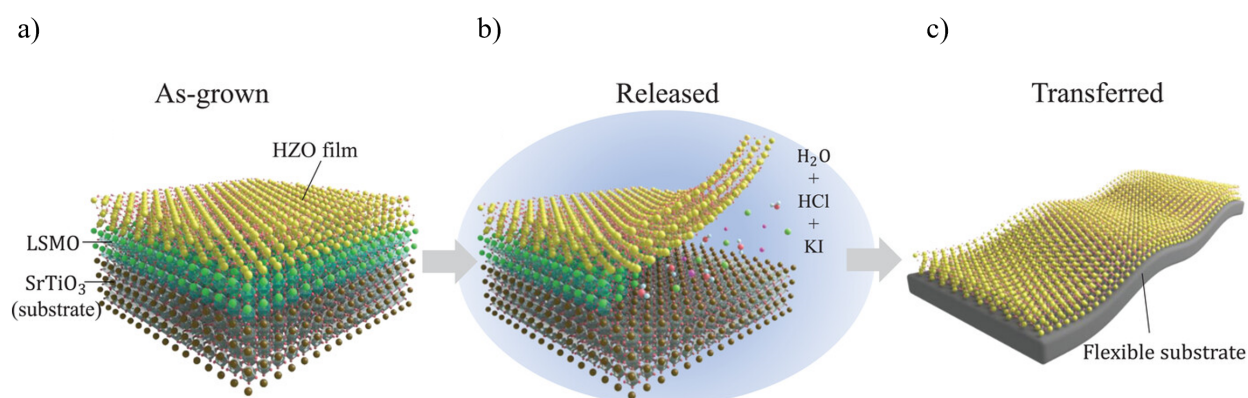
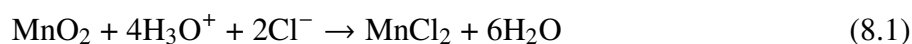


Figure 8.1: Schematic process flow to fabricate free-standing HZO films. a) HZO is epitaxially grown onto STO/LSMO. b) The LSMO layer is dissolved in a solution of HCl + KI + H_2O , releasing the HZO film. c) The free-standing film can be transferred onto various substrates, including flexible substrates. Reproduced with permission from [210].

First, a PPC (Polypropylene carbonate) layer is spin-coated onto the sample to later support the HZO thin film in its free-standing state. Subsequently, a significantly larger PDMS (Polydimethylsiloxane) gel stamp is attached to the sample for further support and improved handling. The LSMO layer is then etched from the exposed sides in a solution of hydrogen chloride (0.5 ml HCl, 37%), potassium iodine (0.5 mL KI), ascorbic acid (0.5 mL $C_6H_8O_6$) and 10 mL of deionised water, based on the following reaction:



reducing the insoluble Mn^{4+} and Mn^{3+} to soluble Mn^{2+} . The ascorbic acid was added to prevent oxidation of the solution. No damage to the STO or HZO was found on the time scales investigated. After 7-10 days, the LSMO is sufficiently dissolved to manually remove the STO substrate, while the HZO remains on the PDMS. Figure 8.2a shows a photo of an exemplary HZO membrane after the release step, on top of PDMS/PPC. It can be cleaned and subsequently attached to the new host substrate by manually applying pressure and carefully removing trapped air with a cleanroom swab. After heating the newly created stack up to $120^\circ C$ for 10 min on a hot plate, the adhesion of the PPC is weakened and the PDMS can be removed. Lastly, the PPC is dissolved in acetone, and the final sample is cleaned with isopropanol and dried. The former STO host substrate can generally be reused for future depositions. An exemplary HZO membrane transferred onto Nb:STO, with evaporated Pt top electrodes, is shown in Figure 8.2b. Several wrinkles that are introduced by the transfer process are visible across the whole film.

Details on the fabrication technique can be found in [207, 211, 212] and in the PhD Thesis of Marcus Wohlgemuth (to be published).

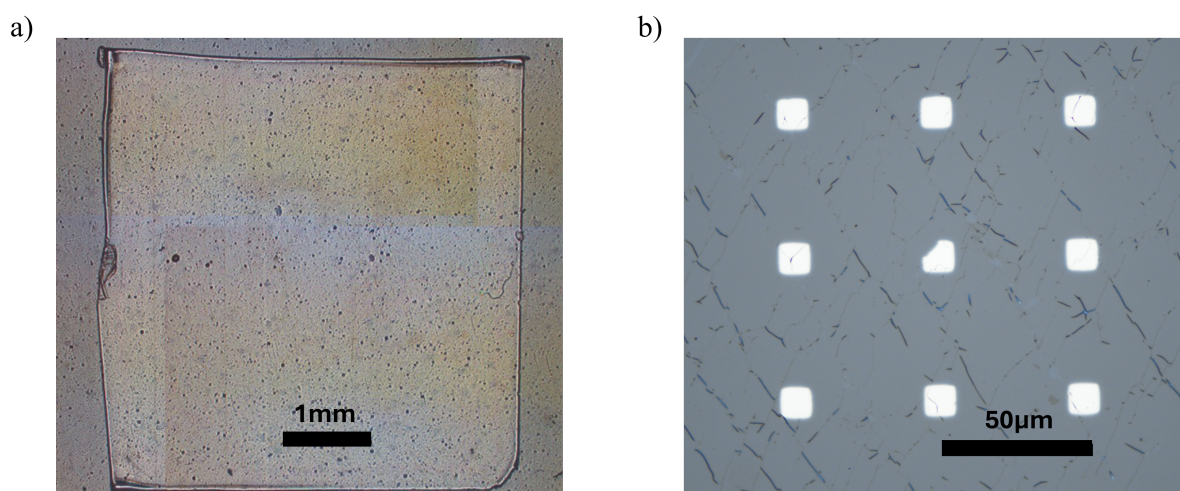


Figure 8.2: a) Image of an HZO membrane on PDMS/PPC. b) HZO membrane transferred onto Nb:SrTiO_3 with Pt top electrodes ($12 \times 12 \mu\text{m}$). Several wrinkles are visible.

8.2 Phase Stability

The structural stability of the epitaxial HZO thin films, with a focus on the ferroelectric orthorhombic phase, is examined in the context of potential integration with CMOS-compatible platforms and flexible electronic applications. First, the stability of the crystalline phase upon general release of the film and its subsequent transfer to a new host substrate is evaluated. Next, the influence of thermal treatment on membranes transferred onto substrates with varying lattice parameters is investigated to evaluate possible lattice adaptation and phase stability across a wide temperature range. Lastly, the robustness of the o-phase under mechanical deformation is examined via XRD measurements of a bent HZO membrane.

Transfer

Figure 8.3 shows representative cases of structural evolution observed upon releasing epitaxial HZO films and transferring them to different host substrates. In Figure 8.3a a 6 nm HZO film with negligible monoclinic phase content was transferred onto a TiN substrate. The XRD measurement both during the transfer stage (on PDMS) and post-transfer onto TiN closely resembles the as-grown film on LSMO; no phase change due to the transfer process can be detected. Contrary to some reports in the literature, the transfer does not induce a measurable shift in the o-phase peak position, indicating that $d_{o(111)}$ remains stable [210].

Deviating behavior is shown in Figure 8.3b, where a HZO film (9 nm) with predominant o-phase but additional monoclinic contribution underwent a phase change during transfer. After the release of the film, on PDMS, an increase in the monoclinic phase fraction is already evident, and this trend continues after transfer to TiN, ultimately resulting in approximately equal o- and m-phase contributions. From these two exemplary transfers, it becomes clear that the stability of the o-phase is not inherently dictated by the host substrate. Rather, the presence of an initial monoclinic

fraction appears to promote further transformation during the release and transfer processes, thus compromising the phase stability.

A third example is shown in Figure 8.3c, where an initially o-phase pure HZO film (comparable to the one in Figure 8.3a) is transferred onto Nb:SrTiO₃ (NSTO). Despite the absence of m-phase in the as-grown state, a pronounced monoclinic contribution emerges after transfer. This result suggests that the phase stability during transfer is not solely determined by the initial phase composition. Instead, some degree of stochastic behavior is inherent to the transfer process, likely attributable to manual handling during membrane fabrication. Consequently, these findings emphasize the need for careful control over processing conditions and reproducibility to maintain the original phase distribution in free-standing membranes.

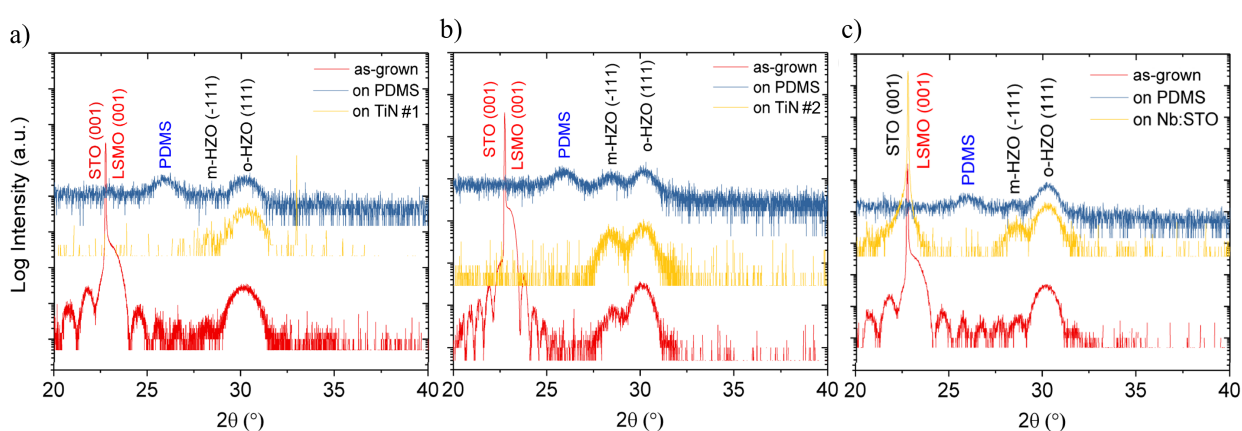


Figure 8.3: XRD analyses of as-grown HZO thin films and their transferred free-standing membranes. a) 6 nm HZO membrane transferred onto the TiN substrates. The HZO film was grown at 800°C on 10 nm LSMO. b) 9 nm transferred onto a TiN substrate. The HZO film is grown at 750°C on 20 nm LSMO substrate. c) 9 nm HZO membrane transferred onto an Nb:SrTiO₃ substrate. The HZO film was grown at 800°C on 10 nm LSMO.

HT-XRD (High-Temperature X-Ray Diffraction)

In the context of exploiting the versatility of the free-standing membranes, potential proceeding fabrication steps might expose the membranes to elevated temperatures. Therefore, it is essential to investigate whether HZO membranes can retain their phase stability at increasing temperatures and explore the stability limits, specifically on new host substrates. To assess the thermal stability of the crystalline phases under ambient conditions, membranes were transferred onto Si/SiO₂ and various single-crystalline substrates with differing lattice parameters. The selected substrates include LaAlO₃ (LAO, $a = 3.794 \text{ \AA}$), Nb-doped SrTiO₃ (NSTO, $a = 3.905 \text{ \AA}$), and DyScO₃ (DSO, $a = 3.945 \text{ \AA}$). These materials span a range of increasing lattice constants, as sketched in Figure 8.5a, particularly when compared to the original growth substrate, LSMO, with a bulk lattice parameter of 3.874 \AA . The samples are then slowly heated up to 850°C followed by cooling to room temperature, while continuously monitoring their structural evolution via *in-situ* XRD.

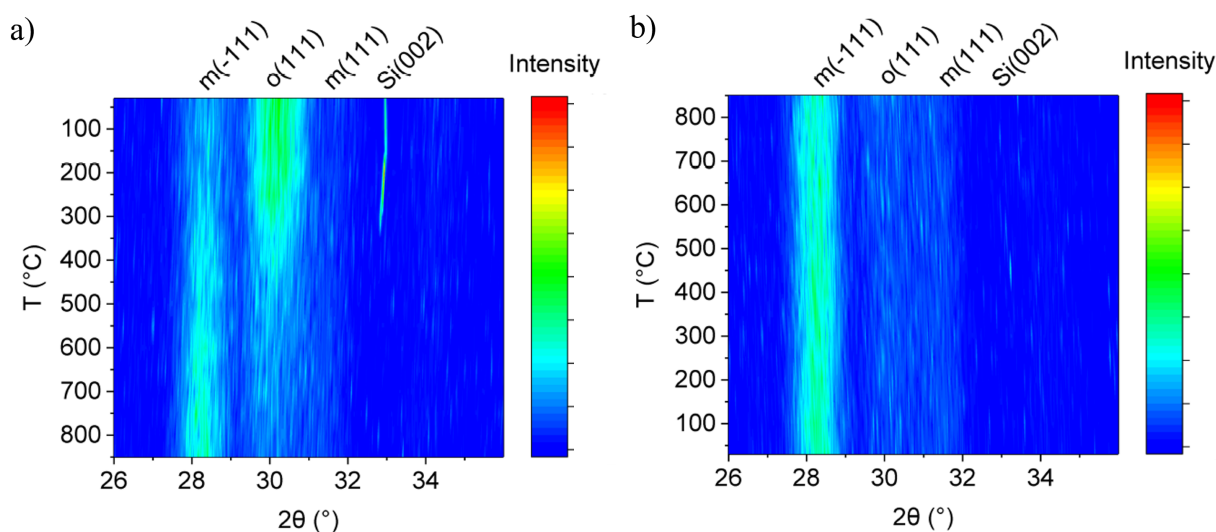


Figure 8.4: High temperature X-ray diffraction (HT-XRD) measurement of 8 nm HZO on a Si/SiO₂ substrate. a) *in-situ* heating of the sample up to 850°C. b) Subsequent cooling to room temperature.

The measurement on Si/SiO₂ is displayed as a heat-map resembling the detected intensity in Figure 8.4a for the heating phase and in Figure 8.4b for the cooling phase. Exemplary of the single crystalline substrates, Figure 8.5b and 8.5c show the HT-XRD maps of DSO for heating and cooling, respectively. Equivalent maps of all crystalline substrates together are provided in Figure A.7 in the appendix. At each temperature step, the o(111) and the m(-111) reflections of the HZO membrane are fitted using Gaussian peak profiles, and the intensities are normalized to the initial (maximum) o-phase intensity. The evolution of the normalized peak intensity of the o-phase for all substrates is summarized in Figure 8.6a for heating and in 8.6b for cooling.

Two general trends emerge when tracking the o-phase intensity during heating. Across all substrates, independent of the lattice constant and including Si/SiO₂, a consistent reduction in o-phase intensity by a comparable amount is observed between 250°C and 350°C. This behavior was not observed in the original STO/LSMO/HZO system [213]. In this temperature range, it is plausible that the reduction stems from the outgassing of residual polymers or solvents from the transfer process, which may promote enhanced contact between the membrane and the substrate. The absence of a matching increase in the m-phase signal in Figure 8.6c suggests that the observed loss of o-phase is not related to a structural relaxation via o- to m-phase transformation. Other effects, such as the introduction of some extent of misalignment, are more likely to be the origin of the intensity reduction.

Following this initial decline, the o-phase remains stable until approximately 700°C. Beyond this point, a second drop occurs. The o-phase diminishes with a similar steepness as before until the maximum temperature of 850°C is reached. Upon cooling, if an o-phase fraction remains, its intensity reduction slows down until around 600°C. In this elevated temperature range, it is most likely that a complete relaxation of the HZO membrane takes place. In the absence of clamping effects by the new host substrate or other means of stabilizing the o-phase, the HZO is expected

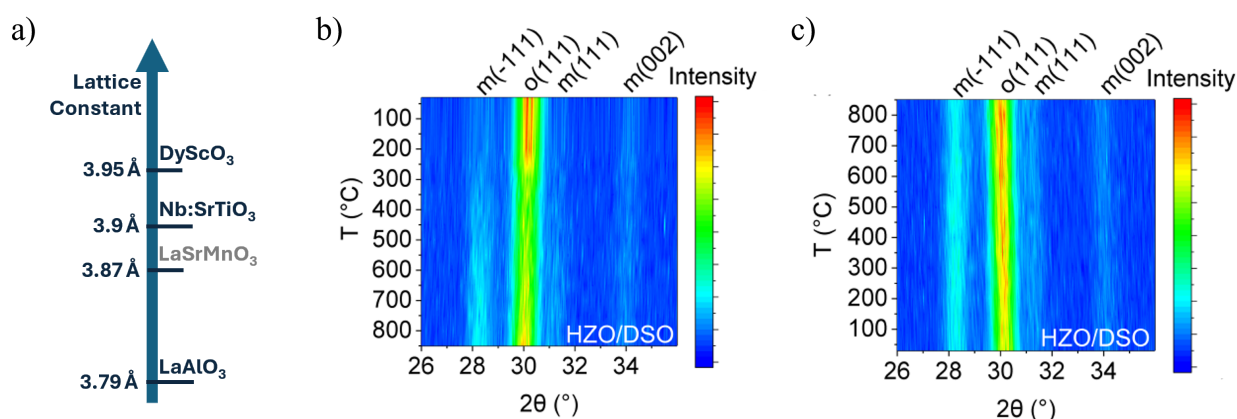


Figure 8.5: a) Spread of the lattice constants of the single-crystalline substrates selected for HT-XRD. HT-XRD measurement of 8 nm HZO on a DyScO₃ substrate. b) *In-situ* heating of the sample up to 850°C and c) subsequent cooling to room temperature.

to revert to its monoclinic bulk phase. Notably, the only exception from this second intensity drop of the o-phase is the membrane transferred onto DSO, maintaining greater o-phase stability during the entire HT-XRD cycle. This can easily be seen from the heat-maps in Figure 8.5, where the o-phase intensity remains nearly unperturbed from 250°C onwards. It is especially noteworthy that despite the differences in lattice constants among the crystalline substrates, their overall behavior closely resembles that of the membrane on Si/SiO₂. This already suggests that lattice mismatch alone is not the dominant factor influencing phase stability. However, it is important to highlight that DSO imposes the greatest tensile strain on the HZO membrane among the substrates tested. An interpretation of this observation is that a substantial tensile strain (estimated at 33% for HZO on DSO, compared to 28% on LAO and 32% on NSTO) may be required to preserve the o-phase in the absence of LSMO. This seems more probable than invoking an interface reconstruction between DSO and HZO similar to the LSMO/HZO interface, where an Mn to Hf/Zr substitution occurred, facilitated by differences in electronegativity (see Section 2.4).

An individual difference observed between the different substrates concerns the extent to which the m-phase develops due to the heating and cooling procedure. It stands out that among all samples, the membrane transferred onto NSTO exhibits the most pronounced monoclinic phase contribution. This sample also displayed a significant monoclinic component immediately after transfer (see Figure 8.3c), reinforcing the earlier conclusion that the presence of an initial monoclinic fraction compromises phase stability as it facilitates further phase change towards the m-phase.

Interestingly, the m-phase intensity is comparable for the membranes on DSO and LAO, despite the substantially different evolution of the o-phase in these two cases. Furthermore, no emergence of alternative monoclinic orientations is detected, as confirmed by the data presented in Figure A.7b. This supports the earlier interpretation that the decline in o-phase intensity cannot be solely attributed to phase transformation, leaving physical deformation and resulting intensity loss due to misalignment or the introduction of a tilt in the crystallites as the likely origin.

The evolution of the lattice constants with temperature can be derived from the peak positions

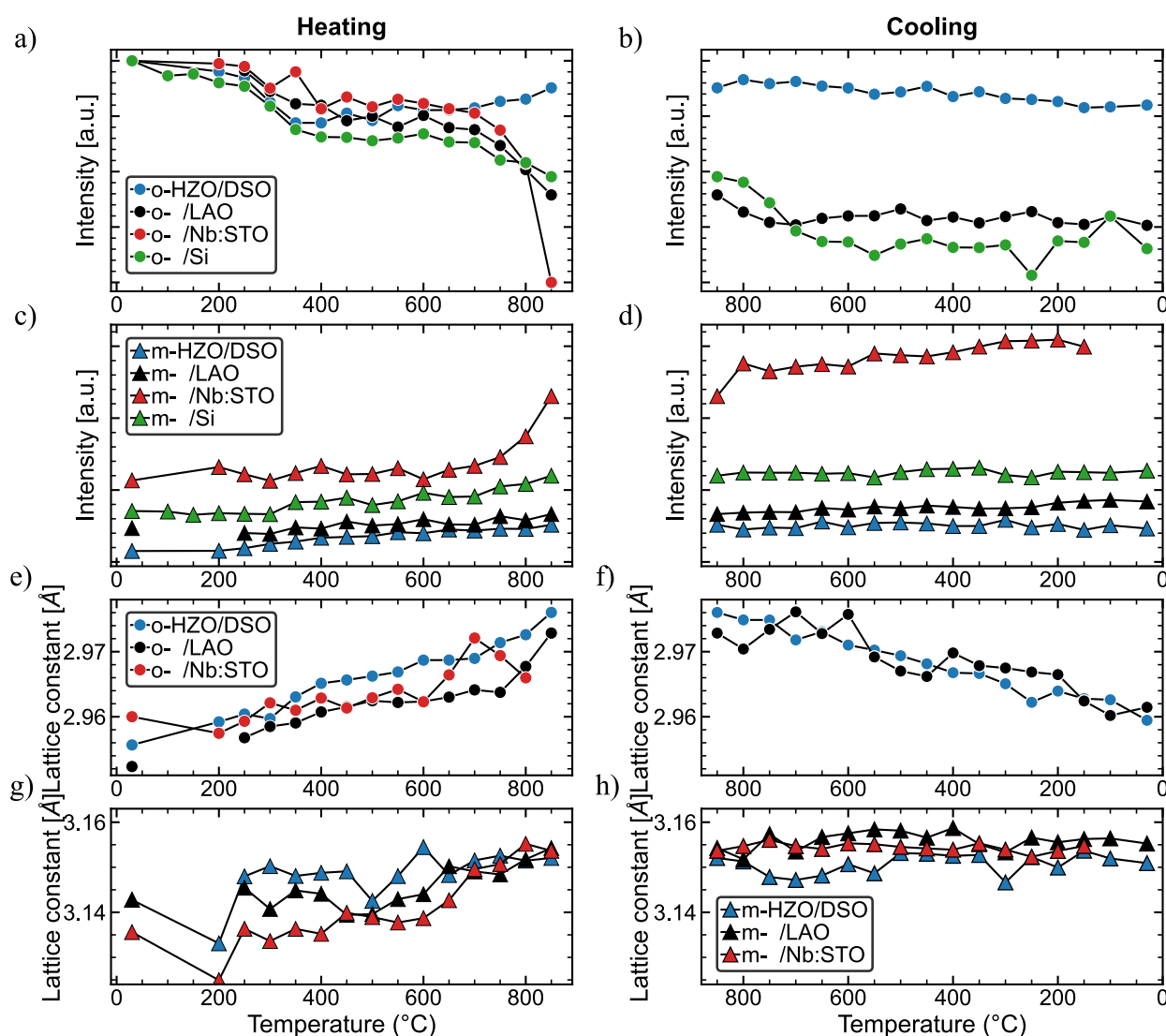


Figure 8.6: Intensity of the o(111) and m(-111) peaks of 10 nm HZO transferred onto DyScO_3 and LaAlO_3 , 9 nm on Nb:SrTiO_3 and 8 nm on Si/SiO_2 . For heating a) and cooling b) of the o-phase and heating c) and cooling d) of the m-phase. The intensity is normalized to the initial intensity of the o(111) peak. Evolution of the o(111) lattice constant on the single crystalline substrates for heating e) and cooling f). The o-phase fully disappears on Nb:SrTiO_3 , hence no data for the cooling. g) Evolution of the m(-111) lattice constant for heating and cooling h).

of the o(111) and m(-111) phase. Figures 8.6e and 8.6f display the temperature dependence of $d_{o(111)}$ during the heating and cooling cycles, respectively, for the single-crystalline substrates. The data reveal no systematic correlation between the substrate lattice constant and the o-phase lattice constant, contradicting the interpretation that the larger tensile strain of the DSO is responsible for the improved stability of the o-phase. This observation aligns with findings by Estandia et al., who reported no difference in $d_{o(111)}$ with the direct growth of HZO on different (LSMO buffered, though fully strained) substrates [29]. Similarly, their subsequent work showed that even

the insertion of an ultra-thin LSMO layer could stabilize the o-phase while having no impact on the strain [31]. Following this, the lack of a clear substrate-dependent effect on lattice spacing should not be interpreted as evidence for the absence of membrane–substrate interaction. Rather, it suggests that epitaxial stabilization may occur through mechanisms beyond strain transfer, such as interface reactions or crystallographic tilt, while showing the same in-plane lattice constants. An approximately linear increase in lattice spacing during heating and a corresponding decrease during cooling can be observed for $d_{o(111)}$, generally matching the expectation of a certain amount of reversible thermal expansion.

In contrast, the evolution of $d_{m(-111)}$ for heating and cooling in Figure 8.6g and 8.6h does not show the same behavior. While the m-phase extends by a similar magnitude upon heating, the increased lattice spacing remains largely unchanged during cooling. No significant difference is observable for the different substrates. Consequently, there seems to be a pre-existing tensile strain within the m-phase of the as-grown film, possibly imposed by the underlying LSMO or the generally dominating o-phase of the film. The monoclinic phase then relaxes irreversibly upon heating (cf. $d_{m(-111), \text{HfO}_2, \text{powder}} = 3.168 \text{ \AA}$) [214].

Bending

A HZO membrane (9 nm) is transferred onto a flexible substrate of Au on mica (muscovite, sheet silicate). This sample is mounted in a custom-built bending stage, designed for compatibility with XRD measurements under controlled bending conditions. The stage is schematically shown in Figure A.6. To account for deformation and following misalignment of the sample surface, each measurement was performed after careful realignment to the incident X-ray beam and the diffraction peak of the Au substrate. Nevertheless, a reduction in the intensity of the HZO o-phase peak was observed with increasing curvature of the membrane. For bending radii $\leq 4.4 \text{ mm}$, it became necessary to flatten the sample post-bending in order to perform the XRD measurement. The observed intensity loss is attributed to the decreasing effective sample area illuminated by the X-ray beam under bending conditions.

Figure 8.7 shows the evolution of the o-phase with decreasing bending radius. No discernible shift in peak position nor the appearance of additional reflections, particularly corresponding to the monoclinic phase, is detected. Further, the comparison of the unbent membrane and those measured after bending (and subsequent flattening) demonstrates that the intensity of the o-peak is fully recoverable. Overall, these findings indicate that ferroelectric HZO membranes possess a high degree of structural phase stability under mechanical deformation, leaving the membranes well-suited for connected applications. It should be noted, though, that ferroelectric measurements could not be performed on the Au/mica system either before or after bending. This is most likely due to the mechanical softness of the substrate configuration, which resulted in immediate damage to the device upon electrical probing with a needle.

In literature, several studies reported on flexible ferroelectric HfO_2 -based systems. However, the majority of these works focus on direct deposition onto flexible substrates, which inherently limits the resulting films to polycrystalline morphology. There, stable ferroelectric switching has been

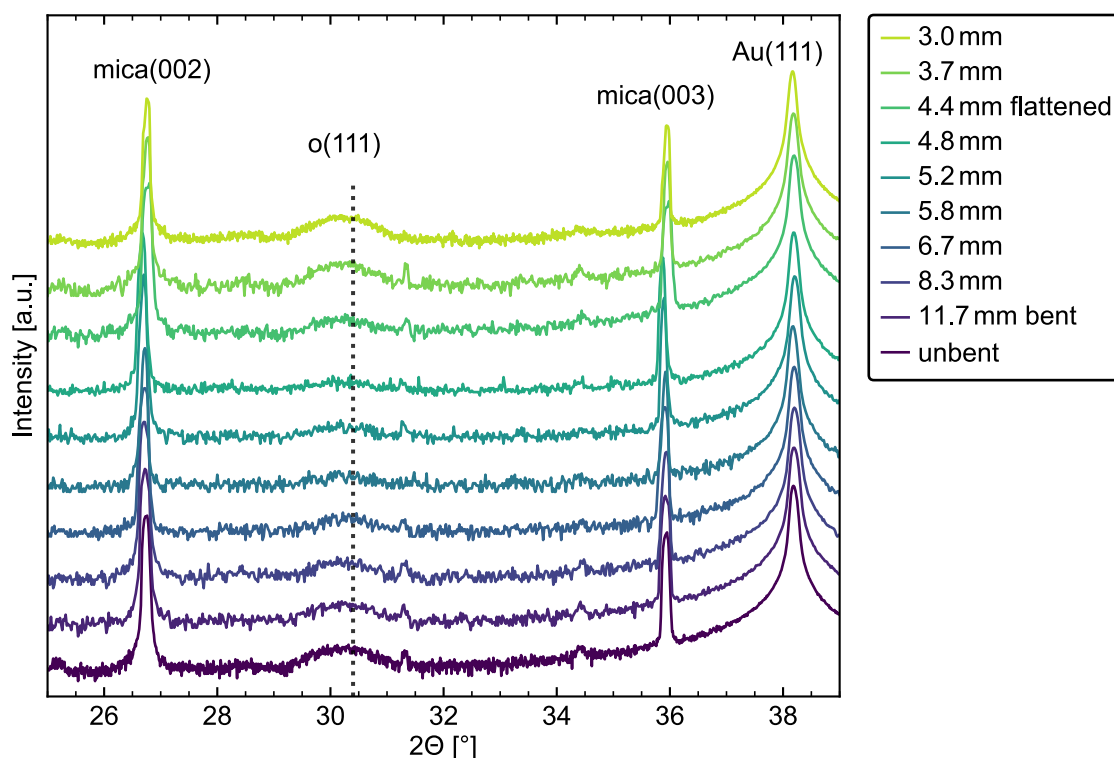


Figure 8.7: *In-situ* XRD measurements of a 9 nm HZO membrane on Au/mica bent to the different indicated radii. The measurements ≤ 4.4 mm correspond to the membrane in flat state, after bending to the respective radius.

demonstrated under bending radii of about 2–8 mm [215–219]. Regarding free-standing epitaxial HZO, Zhong et al. have reported stable hysteresis loops down to a bending radius of 10 mm [210]. Consequently, this work extends this benchmark, demonstrating a bending radius of 3 mm without the emergence of monoclinic contributions or permanent degradation in peak intensity. Nevertheless, the electrical validation of ferroelectric switching after mechanical deformation remains to be realized, especially with regard to the characterization of ferroelectric degradation.

8.3 Switching Characteristics

Lastly, the electrical characterization of the ferroelectric behavior of transferred HZO membranes was carried out. For reference, Figure 8.8a displays a PUND measurement (see Section 6.1) of the as-grown epitaxial STO/LSMO/HZO (6 nm) system with Pt top electrode. A clear distinction between switching and non-switching (dashed) pulses is observed upon applying 3.5 V.

On NSTO, corresponding to the XRD measurements in Figure 8.3c, the measured current at 5 V is approximately one order of magnitude higher, consisting predominantly of leakage current. No ferroelectric switching signal is discernible. Complementary quasi-static I–V sweeps further confirm this increased leakage, effectively masking any potential ferroelectric contribution. A significant monoclinic phase fraction was observed in the XRD measurement post-transfer, which was absent in the as-grown film. This may indicate an elevated defect density introduced during the release

and transfer process, which can be understood by the connected formation of dislocations and possibly cracks in the membrane serving as sites for structural relaxation into the stable m-phase. Simultaneously, such defects facilitate leakage conduction through the HZO layer. As a result, no definitive conclusions can be drawn regarding the ferroelectric behavior in this sample, but the findings underscore the critical importance of careful handling throughout the membrane processing.

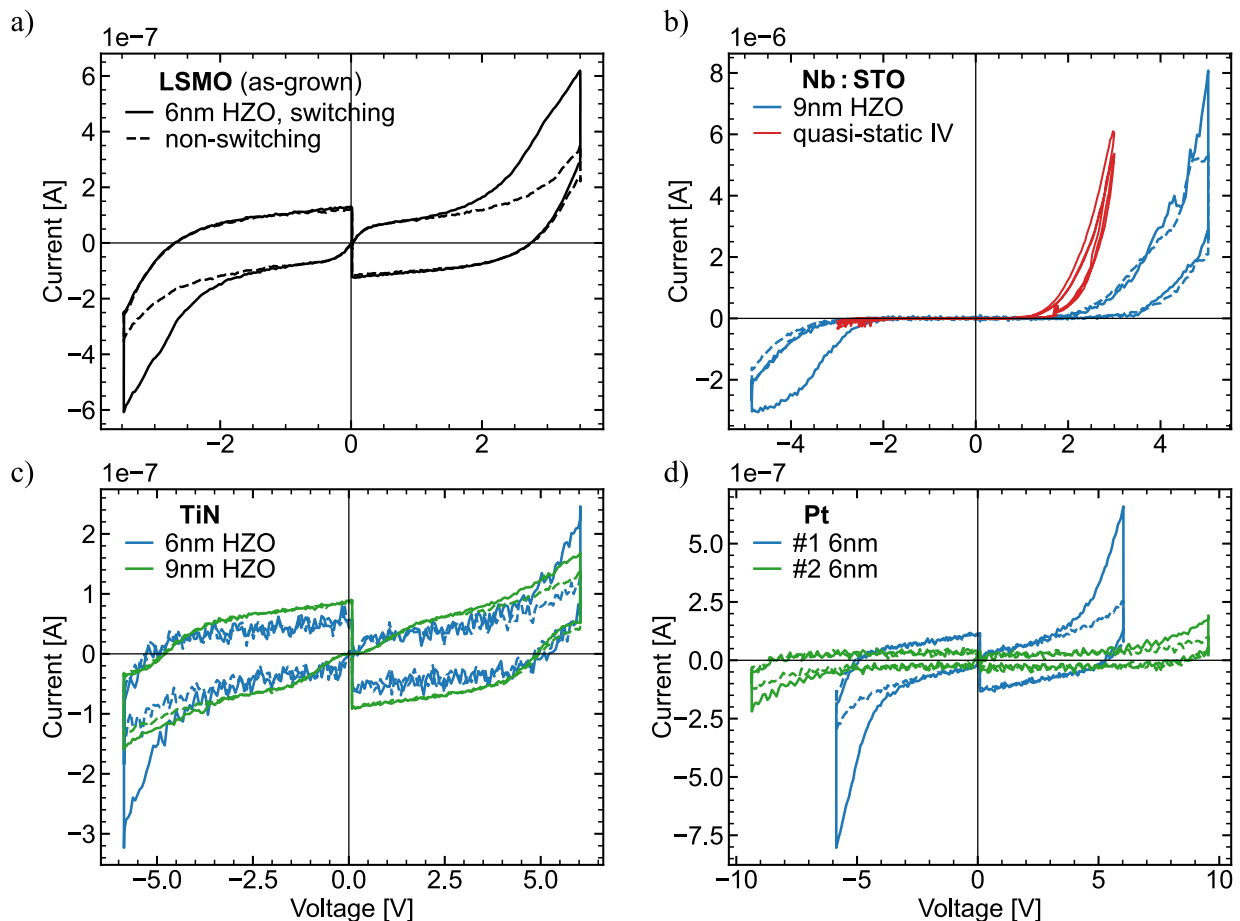


Figure 8.8: PUND measurements of HZO on different substrates. a) As-grown STO/LSMO/HZO epitaxial system with 6 nm HZO. b) 9 nm HZO membrane transferred onto NSTO. PUND measurement (blue) and quasi-static I-V sweeps (red). c) 6 nm and 9 nm HZO membranes on TiN. Corresponding to the XRD measurements TiN #1 and #2 in Figure 8.3a,b, respectively. d) Two 6 nm HZO membranes on Pt, showing different behavior. #1 corresponds to a HZO membrane from the same as-grown sample as TiN #1. XRD measurements are shown in Figure A.8.

Two transferred membranes on TiN were electrically assessed, corresponding to the XRD results labeled TiN #1 and TiN #2 in Figures 8.3a and 8.3b, respectively. As expected, the TiN #1 membrane (6 nm, blue), which exhibited great phase stability upon transfer, also demonstrated superior ferroelectric performance. There is a clear difference visible between switching and non-switching pulses, although requiring nearly double the voltage compared to the as-grown sample. However,

the overall switching magnitude remains lower, suggesting that even higher voltages may be necessary to achieve comparable switching currents. In contrast, the TiN #2 membrane (9 nm, green), which showed a pre-existing m-phase in the as-grown state that increased upon transfer, exhibited a significantly suppressed ferroelectric response at 6 V. Interestingly, despite the dominant m-phase, the leakage current remained low, indicating that the enhanced leakage in the NSTO case can not be directly deduced from the m-phase content.

For Pt substrates, two membranes of equal thickness (6 nm HZO) exhibited vastly different ferroelectric responses. Sample #1 on Pt showed a ferroelectric switching behavior comparable to the as-grown reference when a bias of 6 V was applied. In contrast, sample #2 required a higher voltage of 9 V and still displayed only a weak ferroelectric signal, albeit with minimal leakage. This difference suggests different series resistances between the two samples transferred onto Pt, due to the qualitatively similar behavior but largely different biases required. The transferred XRD measurements of both samples are shown in Figure A.8. The HZO membrane of sample #1 originates from the same as-grown epitaxial STO/LSMO/HZO sample as #1 on TiN, showing approximately pure o-phase. However, after the transfer onto Pt, a significant monoclinic peak emerges. Sample #2 on Pt also shows only o-phase in the as-grown state; here, no m-contribution develops during release and transfer onto Pt. It follows that the presence or emergence of a monoclinic phase is most likely not responsible for the observed differences in ferroelectric performance between the membranes on Pt. The qualitative similarity between the PUND measurement on LSMO and #1 on Pt, despite the m-phase contribution, further suggests that the ferroelectric response is, to a certain extent, insensitive to the presence of the monoclinic phase. The primary distinction lies in the required bias to address ferroelectric switching, which is consistently elevated for all transferred membranes, requiring at least twice the voltage or up to probably ≥ 15 V in some cases. Additionally, the observed selective increase in leakage current following membrane transfer can obscure the ferroelectric response. However, this behavior is not clearly correlated with any specific structural phase change.

Overall, the general feasibility of macroscopic ferroelectric switching in transferred HZO membranes could be demonstrated. In all investigated cases, a parasitic series resistance emerged following the transfer to a new host substrate. As a result, higher or significantly higher applied voltages were required to achieve ferroelectric switching comparable to that of the as-grown state. The magnitude of this varied considerably between individual membranes, showing no direct correlation with the type of host substrate or the presence of a monoclinic phase. This suggests substrate-independent variability introduced during the fabrication and transfer process, likely originating from differences in the quality of the newly formed membrane–substrate interface. On a positive note, it was found that a certain extent of m-phase is not inherently detrimental to the post-transfer ferroelectric response. This implies that phase transformation may occur preferentially at the membrane periphery, thereby sparing the actively used device region in the membrane center. It appears that challenges in measuring ferroelectric hysteresis loops after transfer might have also been involved in the literature. For example, PFM is employed to verify the ferroelectric switching of 1-5 nm HZO membranes [122]. In contrast, Zhong et al. successfully demonstrated conventional hysteresis loops on 10 nm membranes on Si/SiO₂ and on mica/Pt, with the switching behavior nearly

unchanged compared to the as-grown epitaxial reference on STO/LSMO. Only a minor increase in the required switching voltage (approximately 1 V) was observed, underscoring that successful electrical characterization post-transfer is feasible.

8.4 Summary

The structural integrity of the orthorhombic ferroelectric phase during the membrane transfer process was systematically investigated. XRD analysis revealed that membranes with negligible monoclinic phase fractions retain their structural phase stability upon transfer. In contrast, membranes exhibiting pre-existing m-phase components showed an increased m-phase contribution post-transfer, indicating that initial monoclinic content compromises phase stability. Additionally, even o-phase-pure membranes can develop an m-phase contribution during transfer, suggesting a degree of stochasticity likely related to the manual fabrication process.

The thermal stability of transferred membranes on various substrates, including Si/SiO₂ and different single-crystalline substrates of varying lattice constants, revealed largely universal characteristics. All membranes show a decline in o-phase intensity between 250–350°C. A second decline around 700°C is observed in most cases, with the exception of DyScO₃, suggesting that substantial tensile strain (as provided by DSO) may aid the o-phase retention. However, no clear correlation between substrate lattice parameters and the evolution of the $d_{o(111)}$ spacing in HZO was observed, implying that stabilization mechanisms likely include factors beyond strain, such as interface chemistry and crystallite orientation.

Mechanical stability was successfully demonstrated by transferring HZO membranes onto flexible Au/mica substrates. No phase transformation was detected down to bending radii as low as 3 mm, confirming excellent mechanical robustness of the free-standing HZO membranes.

Lastly, ferroelectric switching was confirmed in transferred membranes, although requiring higher voltages than the as-grown films. This behavior was attributed to increased parasitic series resistance, likely originating at the newly formed membrane–substrate interface. Importantly, the presence of a monoclinic phase fraction was not consistently linked to degraded ferroelectric performance. Instead, substrate-independent variations, like leakage current and additional resistance, point to fabrication-related inconsistencies, particularly at the membrane-substrate interface.

In summary, this chapter demonstrates the potential of transferred epitaxial HZO membranes for flexible and CMOS-compatible ferroelectric applications, while highlighting the need for improved transfer reproducibility and interface engineering.

9 Conclusion and Outlook

This thesis explored the coexistence and mutual independence of ferroelectric and filamentary-type resistive switching mechanisms in epitaxial $\text{Hf}_{0.5}\text{Zr}_{0.5}\text{O}_2$ thin films, grown on $\text{La}_{0.8}\text{Sr}_{0.2}\text{MnO}_3$ -buffered SrTiO_3 substrates. The primary objective was to investigate how this dual-mode switching phenomenon operates within a single-crystalline device and how the individual performances and their interplay are governed by structural, electrical, and chemical factors, particularly those related to oxygen vacancy dynamics.

In the ferroelectric mode, HZO exhibited stable polarization switching, marked by well-defined hysteresis loops with negligible wake-up. The fatigue is dominated by the reduction of the remanent polarization; an additional increase of leakage current is occasionally observed.

In contrast, quasi-static I–V measurements induce the formation of localized conductive filaments within the HZO layer, enabling resistive switching based on a filamentary valence change mechanism (VCM). The resistive switching operates without the need for an external current compliance, due to the passive current compliance provided by the LSMO bottom electrode. No electroforming step is required to initiate the filamentary switching, owing to inherent preferential current paths inside the HZO and the LSMO electrode serving as a reservoir for oxygen vacancies. These vacancies can be supplied to support the filament formation under normal SET operation. The high resistance state could be re-established via a standard RESET operation, effectively restoring the pristine state, enabled by the re-incorporation of oxygen vacancies into the LSMO layer. This allows for the unmasked observation of subsequent ferroelectric switching when reverting to high-frequency voltage pulses. The hysteresis loops following the resistive switching are unchanged compared to those measured in the pristine state. Consequently, the oxygen vacancy migration associated with the filament formation and dissolution does not compromise the ferroelectric properties of the HZO layer, confirming that the resistive and ferroelectric switching mechanisms are not only distinct but also largely non-interfering, establishing the dual-mode operation of LSMO/HZO/Pt devices.

For an in-depth understanding of the oxygen vacancy dynamics of both switching mechanisms, qualitatively and quantitatively, synchrotron-based spectroscopy techniques were employed. Operando X-ray photoelectron emission microscopy (XPEEM) provided direct spatial evidence of the conductive filament and further switching-related phenomena, supported by distinct spectral shifts in the local core-level spectra. The findings confirm the highly localized nature of resistive switching and provide an estimate of the electro-chemical footprint of the filament in this system. The filament size was determined to be < 100 nm in diameter, with an oxygen vacancy concentration of

approximately 14%. Other spectroscopic signatures demonstrated a comparably slight reduction of the HZO in the LRS, likely arising along structural defects with lowered oxygen vacancy mobility or formation energy.

Further, in the vicinity of probable switching sites, possible signatures of a phase change into the monoclinic bulk phase upon switching-related Joule heating were identified, although requiring further investigation for clarification.

Simultaneously, operando hard X-ray photoelectron spectroscopy (HAXPES) enabled the depth-resolved analysis of oxygen vacancy dynamics during ferroelectric cycling and degradation. Field-induced redistribution of oxygen vacancies was observed throughout the HZO layer, with preferential accumulation near the buried LSMO/HZO interface, especially with well-advanced fatigue. The polarization-dependent redistribution is most pronounced at the HZO/Pt interface, showing minor complementary changes in the LSMO. While oxygen exchange between the HZO and the LSMO bottom electrode occurs, the majority of additionally generated oxygen vacancies during fatigue are found localized within the HZO, likely accountable for domain pinning and associated ferroelectric degradation.

Jointly considered, these results establish that ferroelectric and resistive switching in epitaxial HZO films can coexist and operate in parallel, governed by different physical processes occurring on distinct voltage and timescales. Ferroelectric switching involves a large spatial spread, with electrochemical changes along the whole device area and depth, whereas resistive switching is driven by strong, highly localized reduction by oxygen vacancy migration. This dual-mode operation is made possible by the unique properties of the crystalline oxide system and the active role of the LSMO electrode, which mediates vacancy transport across both modes without permanent degradation of either switching mechanism.

Epitaxial HZO is generally not compatible with integration into established CMOS processes. The exploration of free-standing ferroelectric HZO membranes tackles this problem. In this work, promising structural and functional stability of HZO membranes was demonstrated across different substrate configurations, under mechanical deformation, and for thermal treatment below 350°C. Reductions in the orthorhombic phase were noted at higher temperatures, together with an increase in the monoclinic phase, which tends to propagate once formed. Nevertheless, the overall phase stability and switching behavior remained robust. The main obstacle for fully unperturbed ferroelectric performance post-transfer was identified to be a varying degree of additional series resistance emerging from the newly formed membrane interfaces, suggesting room for optimization of the fabrication process.

In summary, this work not only demonstrated the unprecedented coexistence of ferroelectric and filamentary resistive switching in a single epitaxial system but also provided a comprehensive experimental framework for characterizing oxygen vacancy behavior under realistic device operating conditions. The insights gained into the role of interfaces, vacancy transport, and material structure lay a strong foundation for future advances in multifunctional oxide electronics and CMOS-compatible non-volatile memory technologies.

Outlook

While this work has focused primarily on quasi-static measurements for resistive switching, practical memory applications demand high-speed performance. Therefore, future investigations should extend into pulsed switching regimes to determine the intrinsic switching speed limits in both ferroelectric and valence change memory modes and to identify possible switching protocols that independently address both mechanisms, also in this regime.

A significant finding of this study was the spatially inhomogeneous redistribution of oxygen vacancies during ferroelectric switching. To enhance device endurance and stability, future research should explore methods to suppress the local pinning of oxygen vacancies, possibly by in-depth interface engineering involving the LSMO bottom electrode, thereby mitigating or at least reducing associated degradation effects.

To gain further insight into resistive switching-related structural changes, *operando* characterizations could be extended to nano-focused X-ray diffraction (nano-XRD) techniques to correlate local phase distribution with the locations of filament formation.

The utilization of free-standing HZO membranes is still in its early stages but holds significant potential for future exploration. The primary objective should be the improvement of the membrane/electrode interface to isolate and better understand the intrinsic properties of the membrane itself, as well as its interaction with new host substrates, by minimizing the influence of fabrication-related artifacts. Preventing the formation and propagation of undesirable monoclinic phases is crucial, as these phases can detrimentally affect device performance.

Evaluating the long-term stability of membrane-based devices on diverse substrates will be essential to explore different interface interactions and degradation mechanisms, consequently ensuring reliability across a broad range of application environments. In the same regard, the switching behavior under mechanical deformation, such as during or after bending the membrane, still needs to be investigated. The stability of the orthorhombic phase was demonstrated. Consequently, sustained ferroelectric switching can be expected, opening up a wide range of possibilities regarding the development of flexible electronics.

A Appendix

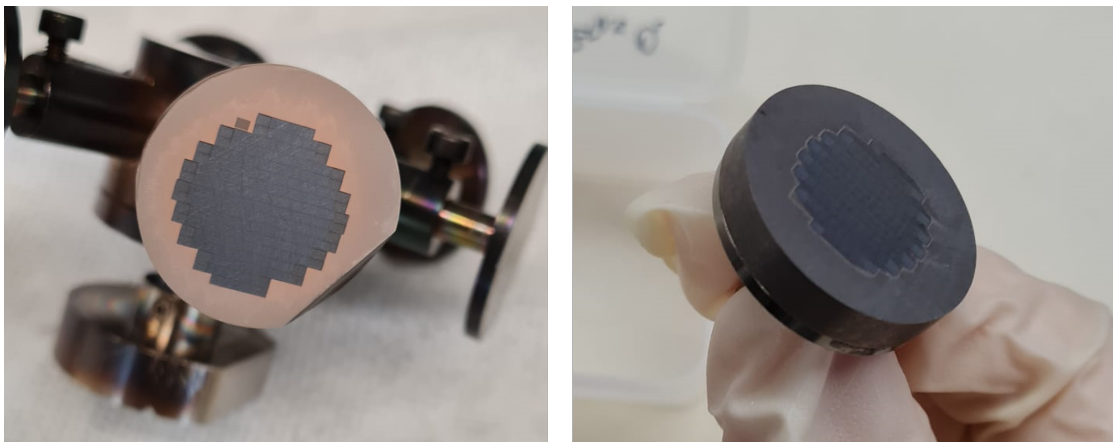


Figure A.1: Different intensity of HZO target discoloring after growth at 1 J/cm^2 laser fluence. Observed together with a significantly reduced growth rate.

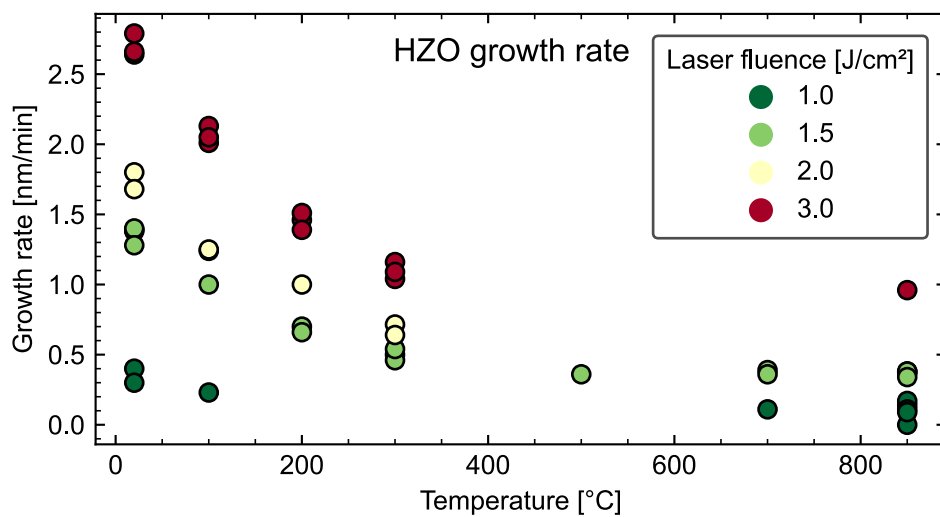


Figure A.2: HZO growth rate at various temperatures and laser fluences at 2 Hz and 0.1 mbar O_2 growth pressure.

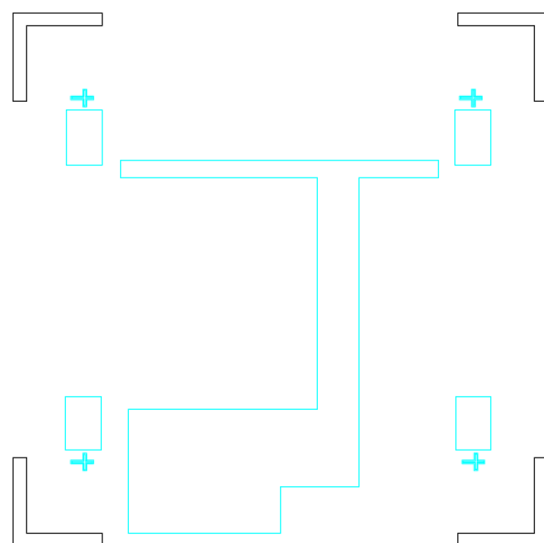


Figure A.3: Mask for additional bottom electrode etching of the *operando* HAXPES sample design.

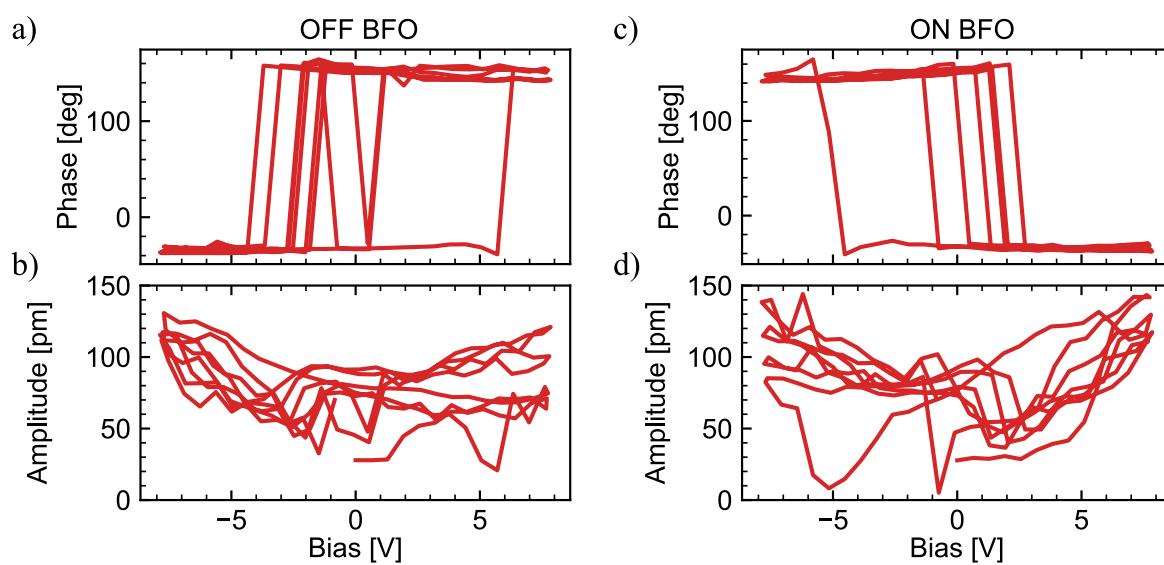


Figure A.4: Switching spectroscopy PFM measurements of a BiFeO_3 sample, serving as a reference to determine the direction of the phase switch in HZO. a) off-field phase b) off-field amplitude c) on-field phase d) on-field amplitude.

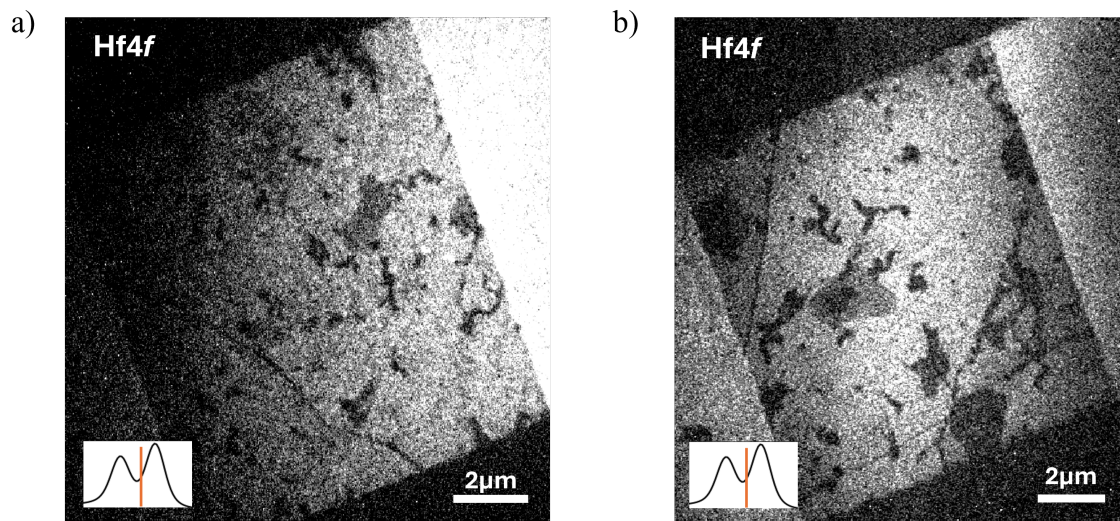


Figure A.5: XPEEM Hf 4f measurements of additional, equivalent devices. Both devices, a) and b) in the pristine state show no signs of the spotty structures found in Figure 7.2. The sketched spectrum in the bottom left indicates that the image is extracted at a similar relative position. Adapted with permission from [134].

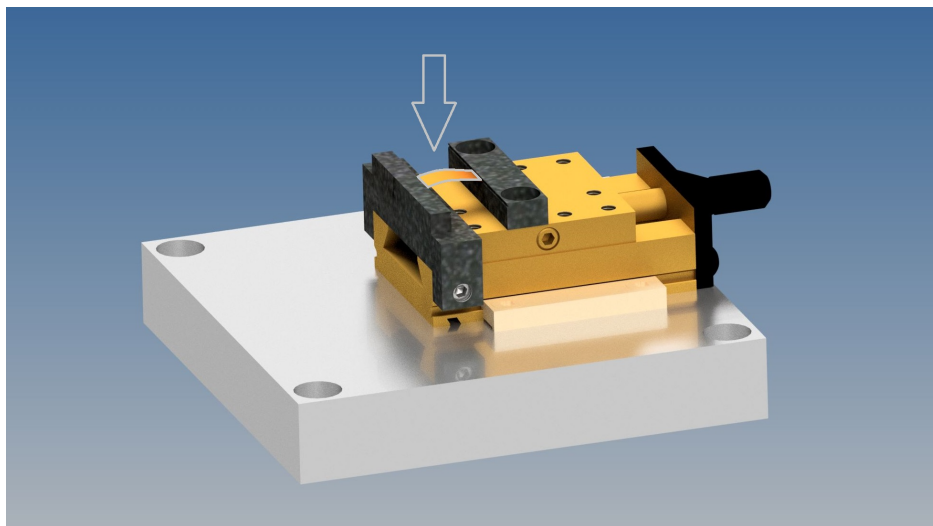


Figure A.6: Setup that can be installed inside a Bruker D8 discover for XRD measurements of bent flexible samples. The sample is fixed between two notches, indicated by the arrow. It bends upwards by tightening the screw on the right side. Image courtesy of Stephan Masberg.

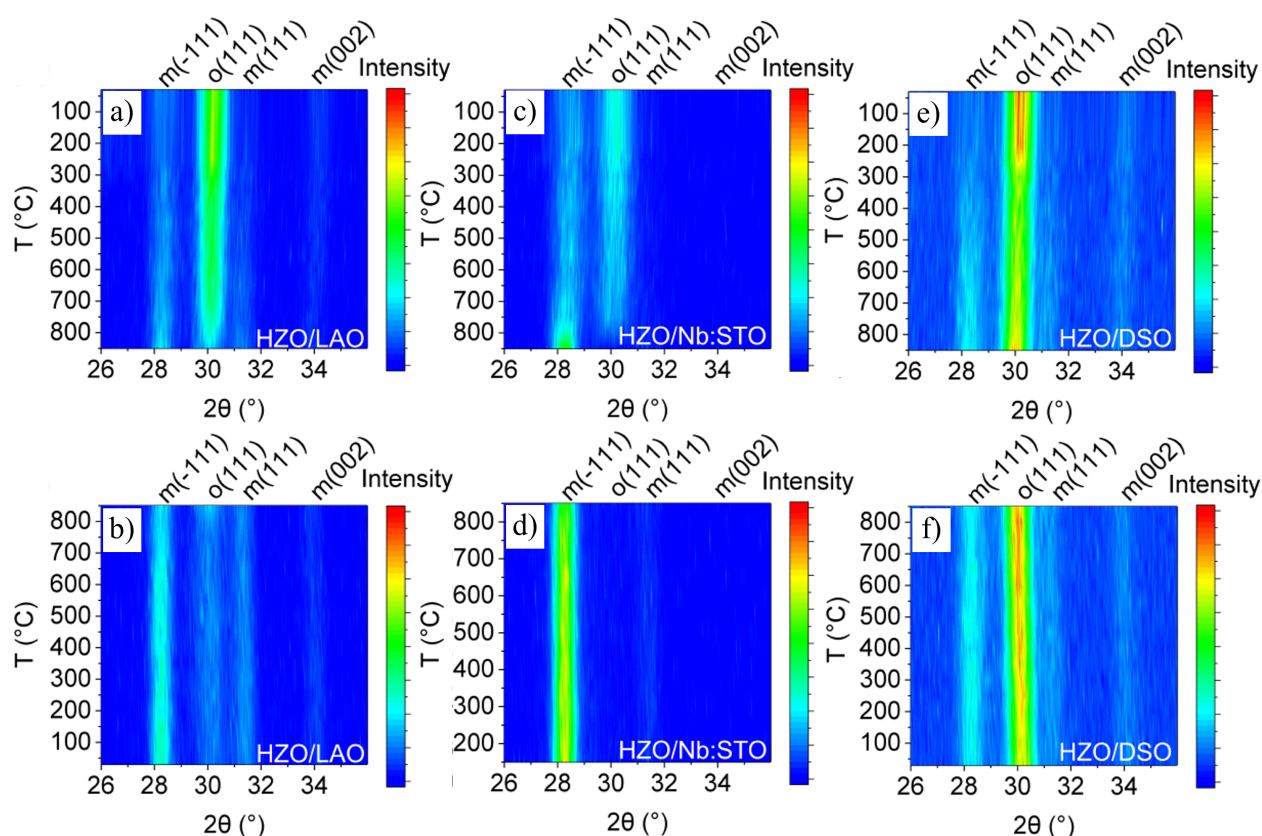


Figure A.7: *In-situ* HT-XRD measurements of HZO membranes on different single crystalline substrates. a) Heating and b) cooling of a 10 nm HZO membrane on LaAlO_3 . c) Heating and d) cooling of a 9 nm HZO membrane on Nb:SrTiO_3 . e) Heating and f) cooling of a 10 nm HZO membrane on DyScO_3 . The membranes on LAO and DSO are from the same epitaxial as-grown film. The HZO membrane on NSTO was grown at 750°C , resulting in a more pronounced monoclinic phase in the pristine state.

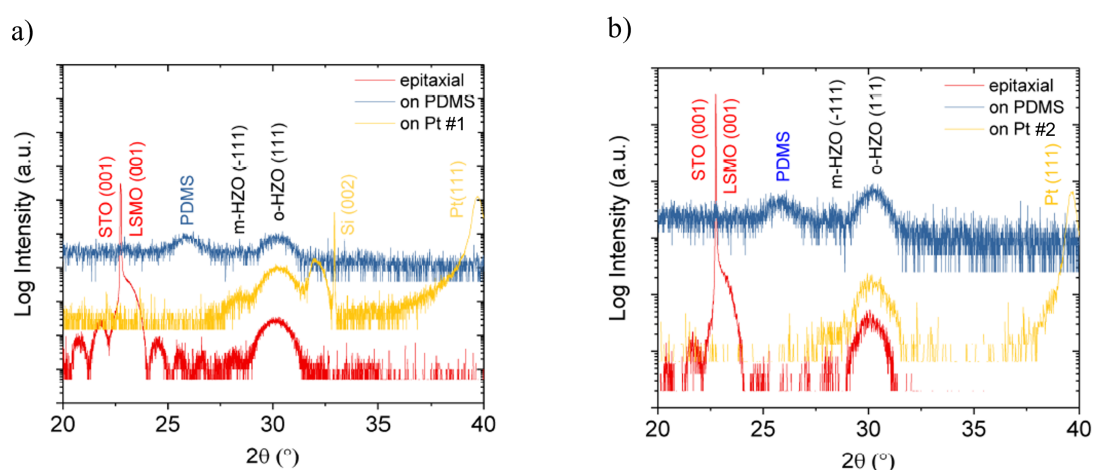


Figure A.8: XRD patterns of the #1 6 nm a) and #2 6 nm b) HZO membranes transferred onto Pt substrates. The diffraction patterns of the as-grown HZO films and the films on PDMS are shown for comparison. Both HZO films were grown using same growth parameters. The film #1 is from the same as-grown sample as #1 on TiN.

Bibliography

- [1] G. E. Moore. “Cramming More Components onto Integrated Circuits”. *Electronics* 38.8 (1965), pp. 114–.
- [2] Y. Taur. “CMOS Design near the Limit of Scaling”. *IBM Journal of Research and Development* 46.2.3 (2002), pp. 213–222.
- [3] R. Waser, R. Dittmann, C. Staikov, and K. Szot. “Redox-Based Resistive Switching Memories Nanoionic Mechanisms, Prospects, and Challenges”. *Advanced Materials* 21.25-26 (2009), pp. 2632–2663.
- [4] A. Chen, J. Hutchby, V. V. Zhirnov, and G. Bourianoff. *Emerging Nanoelectronic Devices*. John Wiley & Sons, Ltd, 2015.
- [5] M. Coll et al. “Towards Oxide Electronics: A Roadmap”. *Applied Surface Science* 482 (2019), pp. 1–93.
- [6] A. Sawa. “Resistive Switching in Transition Metal Oxides”. *Materials Today* 11.6 (2008), pp. 28–36.
- [7] J. J. Yang, D. B. Strukov, and D. R. Stewart. “Memristive Devices for Computing”. *Nature Nanotechnology* 8.1 (2013), pp. 13–24.
- [8] R. Dittmann, S. Menzel, and R. Waser. “Nanoionic Memristive Phenomena in Metal Oxides: The Valence Change Mechanism”. *Advances in Physics* 70.2 (2022), pp. 155–349.
- [9] J. Joshua Yang, F. Miao, M. D. Pickett, D. A. Ohlberg, D. R. Stewart, C. N. Lau, and R. S. Williams. “The Mechanism of Electroforming of Metal Oxide Memristive Switches”. *Nanotechnology* 20.21 (2009).
- [10] H.-S. P. Wong, H.-Y. Lee, S. Yu, Y.-S. Chen, Y. Wu, P.-S. Chen, B. Lee, F. T. Chen, and M.-j. Tsai. “Metal–Oxide RRAM”. *Proceedings of the IEEE* 100.6 (2012), pp. 1951–1970.
- [11] H.-Y. Lee, P.-S. Chen, C.-C. Wang, S. Maikap, P.-J. Tzeng, C.-H. Lin, L.-S. Lee, and M.-J. Tsai. “Low-Power Switching of Nonvolatile Resistive Memory Using Hafnium Oxide”. *Japanese Journal of Applied Physics* 46.4B (2007), pp. 2175–2179.
- [12] R. Dittmann and J. P. Strachan. “Redox-Based Memristive Devices for New Computing Paradigm”. *APL Materials* 7.11 (2019), p. 110903.

-
- [13] A. Grossi, M. Coppetta, S. Aresu, A. Kux, T. Kern, and R. Strenz. “28nm Data Memory with Embedded RRAM Technology in Automotive Microcontrollers”. 2023, pp. 1–4.
- [14] C. Baeumer et al. “Spectromicroscopic Insights for Rational Design of Redox-Based Memristive Devices”. *Nature Communications* 6 (2015), p. 9610.
- [15] D.-H. Kwon et al. “Atomic Structure of Conducting Nanofilaments in TiO₂ Resistive Switching Memory”. *Nature Nanotechnology* 5.2 (2010), pp. 148–153.
- [16] J.-Y. Chen, C.-W. Huang, C.-H. Chiu, Y.-T. Huang, and W.-W. Wu. “Switching Kinetic of VCM-Based Memristor: Evolution and Positioning of Nanofilament”. *Advanced Materials* 27.34 (2015), pp. 5028–5033.
- [17] T. Heisig, K. Lange, A. Gutsche, K. T. Goss, S. Hambsch, A. Locatelli, T. O. Menten, F. Genuzio, S. Menzel, and R. Dittmann. “Chemical Structure of Conductive Filaments in Tantalum Oxide Memristive Devices and Its Implications for the Formation Mechanism”. *Advanced Electronic Materials* 8.8 (2022), pp. 2100936/1–.
- [18] J. Valasek. “Piezo-Electric and Allied Phenomena in Rochelle Salt”. *Physical Review* 17 (1920), p. 475.
- [19] R. W. Whatmore, Y.-M. You, R.-G. Xiong, and C.-B. Eom. “100 Years of Ferroelectricity—A Celebration”. *APL Materials* 9.7 (2021), p. 070401.
- [20] J. F. Scott and C. A. Paz-de-Araujo. “Ferroelectric Memories”. *Science, USA* 246.4936 (1989), pp. 1400–5.
- [21] N. Setter et al. “Ferroelectric Thin Films: Review of Materials, Properties, and Applications”. *Journal of Applied Physics, USA* 100.5 (2006), pp. 51606-1–46.
- [22] T. S. Böscke, J. Müller, D. Bräuhäus, U. Schröder, and U. Böttger. “Ferroelectricity in Hafnium Oxide Thin Films”. *Applied Physics Letters* 99.10 (2011), pp. 2–4.
- [23] T. Mikolajick, U. Schroeder, and S. Slesazek. “The Past, the Present, and the Future of Ferroelectric Memories”. *IEEE Transactions on Electron Devices* 67.4 (2020), pp. 1434–1443.
- [24] W. Banerjee, A. Kashir, and S. Kamba. “Hafnium Oxide (HfO₂) - A Multifunctional Oxide: A Review on the Prospect and Challenges of Hafnium Oxide in Resistive Switching and Ferroelectric Memories”. *Small* 2107575 (2022), pp. 1–50.
- [25] J. Müller, T. S. Böscke, U. Schröder, S. Mueller, D. Bräuhäus, U. Böttger, L. Frey, and T. Mikolajick. “Ferroelectricity in Simple Binary ZrO₂ and HfO₂”. *Nano Letters* 12.8 (2012), pp. 4318–4323.
- [26] J. Müller, P. Polakowski, S. Mueller, and T. Mikolajick. “Ferroelectric Hafnium Oxide Based Materials and Devices: Assessment of Current Status and Future Prospects”. *ECS Journal of Solid State Science and Technology* 4.5 (2015), N30–N35.
- [27] R. Materlik, C. Kunneth, and A. Kersch. “The Origin of Ferroelectricity in Hf_{1-x}Zr_xO₂: A Computational Investigation and a Surface Energy Model”. *Journal of Applied Physics* 117.13 (2015), p. 134109.

- [28] Y. Wei et al. “A Rhombohedral Ferroelectric Phase in Epitaxially Strained Hf_{0.5}Zr_{0.5}O₂ Thin Films”. *Nature Materials* 17.12 (2018), pp. 1095–1100.
- [29] S. Estandía, N. Dix, J. Gazquez, I. Fina, J. Lyu, M. F. Chisholm, J. Fontcuberta, and F. Sánchez. “Engineering Ferroelectric Hf_{0.5}Zr_{0.5}O₂ Thin Films by Epitaxial Stress”. *ACS Applied Electronic Materials* 1.8 (2019), pp. 1449–1457.
- [30] S. Estandía, T. Cao, R. Mishra, I. Fina, F. Sánchez, and J. Gazquez. “Insights into the Atomic Structure of the Interface of Ferroelectric Hf_{0.5}Zr_{0.5}O₂ Grown Epitaxially on La_{2/3}Sr_{1/3}MnO₃”. *Physical Review Materials* 5.7 (2021), p. 074410.
- [31] S. Estandía, J. Gàzquez, M. Varela, N. Dix, M. Qian, R. Solanas, I. Fina, and F. Sánchez. “Critical Effect of the Bottom Electrode on the Ferroelectricity of Epitaxial Hf_{0.5}Zr_{0.5}O₂ Thin Films”. *Journal of Materials Chemistry C* 9.10 (2021), pp. 3486–3492.
- [32] M. Pešić et al. “Physical Mechanisms behind the Field-Cycling Behavior of HfO₂-Based Ferroelectric Capacitors”. *Advanced Functional Materials* 26.25 (2016), pp. 4601–4612.
- [33] F. P. G. Fengler et al. “Domain Pinning: Comparison of Hafnia and PZT Based Ferroelectrics”. *Advanced Electronic Materials* 3.4 (2017), p. 1600505.
- [34] D. R. Islamov and T. V. Perevalov. “Effect of Oxygen Vacancies on the Ferroelectric Hf_{0.5}Zr_{0.5}O₂ Stabilization: DFT Simulation”. *Microelectronic Engineering* 216 (2019), p. 111041.
- [35] P. Nukala et al. “Reversible Oxygen Migration and Phase Transitions in Hafnia-Based Ferroelectric Devices”. *Science* 372.6542 (2021), pp. 630–635.
- [36] S. Starschich, S. Menzel, and U. Böttger. “Evidence for Oxygen Vacancies Movement during Wake-up in Ferroelectric Hafnium Oxide”. *Applied Physics Letters* 108.3 (2016), p. 032903.
- [37] B. Max, M. Pešić, S. Slesazek, and T. Mikolajick. “Interplay between Ferroelectric and Resistive Switching in Doped Crystalline HfO₂”. *Journal of Applied Physics* 123.13 (2018).
- [38] P. Jiang et al. “Freely Switching between Ferroelectric and Resistive Switching in Hf_{0.5}Zr_{0.5}O₂ Films and Its Application on High Accuracy on-Chip Deep Neural Networks”. *Science China Information Sciences* 66.2 (2023), pp. 1–10.
- [39] J. Lyu, I. Fina, and F. Sánchez. “Fatigue and Retention in the Growth Window of Ferroelectric Hf_{0.5}Zr_{0.5}O₂ Thin Films”. *Applied Physics Letters* 117.7 (2020), p. 072901.
- [40] D. Shin, A. V. Ievlev, K. Beckmann, J. Li, P. Ren, N. Cady, and Y. Li. “Oxygen Tracer Diffusion in Amorphous Hafnia Films for Resistive Memory”. *Materials Horizons* 11.10 (2024), pp. 2372–2381.
- [41] S. U. Sharath et al. “Control of Switching Modes and Conductance Quantization in Oxygen Engineered HfO_x Based Memristive Devices”. *Advanced Functional Materials* 27.32 (2017), pp. 1–13.

- [42] W. Hamouda, F. Mehmood, T. Mikolajick, U. Schroeder, T. O. Menten, A. Locatelli, and N. Barrett. “Oxygen Vacancy Concentration as a Function of Cycling and Polarization State in TiN/Hf_{0.5}Zr_{0.5}O₂/TiN Ferroelectric Capacitors Studied by x-Ray Photoemission Electron Microscopy”. *Applied Physics Letters* 120.20 (2022), p. 202902.
- [43] M. O. Hill et al. “Depth-Resolved X-Ray Photoelectron Spectroscopy Evidence of Intrinsic Polar States in HfO₂-Based Ferroelectrics”. *Advanced Materials* (2024), p. 2408572.
- [44] K. M. Rabe, C. H. Ahn, and J.-M. Triscone, eds. *Physics of Ferroelectrics: A Modern Perspective*. Topics in Applied Physics v. 105. Berlin: Springer, 2007.
- [45] M. Dawber, K. M. Rabe, and J. F. Scott. “Physics of Thin-Film Ferroelectric Oxides”. *Reviews of Modern Physics* 77.4 (2005), pp. 1083–1130.
- [46] S. Hoffmann-Eifert, D. Richter, and S. Trolier-Mc Kinsty. “Dielectric, Ferroelectric and Optical Properties”. *Nanoelectronics and Information Technology*. Ed. by R. Waser. 2012, pp. 35–89.
- [47] W. J. Merz. “Domain Formation and Domain Wall Motions in Ferroelectric BaTiO₃ Single Crystals”. *Physical Review* 95.3 (1954), pp. 690–698.
- [48] A. K. Tagantsev, I. Stolichnov, N. Setter, J. S. Cross, and M. Tsukada. “Non-Kolmogorov-Avrami Switching Kinetics in Ferroelectric Thin Films”. *Physical Review B* 66.21 (2002), p. 214109.
- [49] Y. Ishibashi and H. Orihara. “A Theory of D-E Hysteresis Loop-Application of Avrami Model”. *Integrated Ferroelectrics, UK* 9.1-3 (1995), pp. 57–61.
- [50] T. Schenk, U. Schroeder, and T. Mikolajick. “Correspondence - Dynamic Leakage Current Compensation Revisited”. *IEEE Transactions on Ultrasonics, Ferroelectrics, and Frequency Control* 62.3 (2015), pp. 596–599.
- [51] U. Schroeder, M. H. Park, T. Mikolajick, and C. S. Hwang. “The Fundamentals and Applications of Ferroelectric HfO₂”. *Nature Reviews Materials* 7.8 (2022), pp. 653–669.
- [52] D. Ielmini and R. Waser. *Resistive Switching - From Fundamentals of Nanoionic Redox Processes to Memristive Device Applications*. 2016.
- [53] R. Muenstermann, T. Menke, R. Dittmann, and R. Waser. “Coexistence of Filamentary and Homogeneous Resistive Switching in Fe-doped SrTiO₃ Thin-Film Memristive Devices”. *Advanced Materials* 22.43 (2010), pp. 4819–4822.
- [54] D. Cooper, C. Baeumer, N. Bernier, A. Marchewka, C. La Torre, R. E. Dunin-Borkowski, S. Menzel, R. Waser, and R. Dittmann. “Anomalous Resistance Hysteresis in Oxide ReRAM: Oxygen Evolution and Reincorporation Revealed by in Situ TEM”. *Advanced Materials* 29.23 (2017), p. 1700212.
- [55] H. Zhang, S. Yoo, S. Menzel, C. Funck, F. Cüppers, D. J. Wouters, C. S. Hwang, R. Waser, and S. Hoffmann-Eifert. “Understanding the Coexistence of Two Bipolar Resistive Switching Modes with Opposite Polarity in Pt/TiO₂/Ti/Pt Nanosized ReRAM Devices”. *ACS Applied Materials and Interfaces* 10.35 (2018), pp. 29766–29778.

- [56] D. S. Jeong, B. J. Choi, and C. S. Hwang. “Electroforming Processes in Metal Oxide Resistive-Switching Cells”. *Resistive Switching: From Fundamentals of Nanoionic Redox Processes to Memristive Device Applications*. 2016, pp. 289–316.
- [57] S. Menzel, M. Waters, A. Marchewka, U. Böttger, R. Dittmann, and R. Waser. “Origin of the Ultra-nonlinear Switching Kinetics in Oxide-Based Resistive Switches”. *Advanced Functional Materials* 21.23 (2011), pp. 4487–4492.
- [58] A. Fantini, L. Goux, R. Degraeve, D. J. Wouters, N. Raghavan, G. Kar, A. Belmonte, Y. Y. Chen, B. Govoreanu, and M. Jurczak. “Intrinsic Switching Variability in HfO₂ RRAM”. *2013 5th IEEE International Memory Workshop, IMW 2013* (2013), pp. 30–33.
- [59] S. Ambrogio, S. Member, S. Balatti, S. Member, A. Cubeta, A. Calderoni, N. Ramaswamy, S. Member, D. Ielmini, and S. Member. “Statistical Fluctuations in HfO_x Resistive-Switching Memory : Part I - Set / Reset Variability”. *IEEE Transactions on Electron Devices* 61.8 (2014), pp. 2912–2919.
- [60] C. Baeumer et al. “Subfilamentary Networks Cause Cycle-to-Cycle Variability in Memristive Devices”. *ACS Nano* 11.7 (2017), pp. 6921–6929.
- [61] G. Indiveri, E. Linn, and S. Ambrogio. “ReRAM-Based Neuromorphic Computing”. *Resistive Switching: From Fundamentals of Nanoionic Redox Processes to Memristive Device Applications*. 2016, pp. 715–736.
- [62] F. Cüppers, S. Menzel, C. Bengel, A. Hardtdegen, M. von Witzleben, U. Böttger, R. Waser, and S. Hoffmann-Eifert. “Exploiting the Switching Dynamics of HfO₂-based ReRAM Devices for Reliable Analog Memristive Behavior”. *Applied Physics Letters: Materials* 7.9 (2019), pp. 091105/1–9.
- [63] J. M. D. Coey, M. Viret, and S. von Molnár. “Mixed-Valence Manganites”. *Advances in Physics* 48.2 (1999), pp. 167–293.
- [64] M. Gaudon, C. Laberty-Robert, F. Ansart, P. Stevens, and A. Rousset. “Preparation and Characterization of La_{1-x}Sr_xMnO_{3+δ} (0 ≤ x ≤ 0.6) Powder by Sol–Gel Processing”. *Solid State Sciences* 4.1 (2002), pp. 125–133.
- [65] L. P. Gor’kov and V. Z. Kresin. “Mixed-Valence Manganites: Fundamentals and Main Properties”. *Physics Reports-Review Section of Physics Letters* 400.3 (2004), pp. 149–208.
- [66] K. Momma and F. Izumi. “VESTA 3 for Three-Dimensional Visualization of Crystal, Volumetric and Morphology Data”. *Journal of Applied Crystallography* 44.6 (2011), pp. 1272–1276.
- [67] O. Ohtaka, H. Fukui, T. Kunisada, T. Fujisawa, K. Funakoshi, W. Utsumi, T. Irifune, K. Kuroda, and T. Kikegawa. “Phase Relations and Volume Changes of Hafnia under High Pressure and High Temperature”. *Journal of the American Ceramic Society* 84 (2001), pp. 1369–1373.
- [68] J. Mueller et al. “Ferroelectricity in Yttrium-Doped Hafnium Oxide”. *Journal of Applied Physics* 110 (2011), p. 114113.

- [69] S. Mueller, J. Mueller, A. Singh, S. Riedel, J. S. qvist, U. Schroeder, and T. Mikolajick. “Incipient Ferroelectricity in Al-Doped HfO₂ Thin Films”. *Advanced Functional Materials* 22.11 (2012), pp. 2412–2417.
- [70] U. Schroeder, E. Yurchuk, J. Muller, D. Martin, T. Schenk, P. Polakowski, C. Adelman, M. I. Popovici, S. V. Kalinin, and T. Mikolajick. “Impact of Different Dopants on the Switching Properties of Ferroelectric Hafniumoxide”. *Japanese Journal of Applied Physics* 53.8S1 (2014), 08LE02 (5 PP.)–08LE0.
- [71] M. Hoffmann et al. “Stabilizing the Ferroelectric Phase in Doped Hafnium Oxide”. *Journal of Applied Physics* 118.7 (2015), pp. 72006/1–.
- [72] M. Materano, P. D. Lomenzo, A. Kersch, M. H. Park, T. Mikolajick, and U. Schroeder. “Interplay between Oxygen Defects and Dopants: Effect on Structure and Performance of HfO₂-based Ferroelectrics”. *Inorganic Chemistry Frontiers* 8.10 (2021), pp. 2650–2672.
- [73] H. A. Hsain, Y. Lee, G. Parsons, and J. L. Jones. “Compositional Dependence of Crystallization Temperatures and Phase Evolution in Hafnia-Zirconia (Hf_xZr_{1-x})O₂ Thin Films”. *Applied Physics Letters* 116.19 (2020), p. 192901.
- [74] T. Shiraishi et al. “Impact of Mechanical Stress on Ferroelectricity in (Hf_{0.5}Zr_{0.5})O₂ Thin Films”. *Applied Physics Letters* (2016).
- [75] S. J. Kim et al. “Large Ferroelectric Polarization of TiN/Hf_{0.5}Zr_{0.5}O₂/TiN Capacitors Due to Stress-Induced Crystallization at Low Thermal Budget”. *Applied Physics Letters* 111.24 (2017), p. 242901.
- [76] T. Shiraishi et al. “Effect of the Film Thickness on the Crystal Structure and Ferroelectric Properties of (Hf_{0.5}Zr_{0.5})O₂ Thin Films Deposited on Various Substrates”. *Materials Science in Semiconductor Processing. Control of Semiconductor Interfaces and SiGe Technology/Devices* 70 (2017), pp. 239–245.
- [77] S. S. Cheema et al. “Enhanced Ferroelectricity in Ultrathin Films Grown Directly on Silicon”. *Nature* 580.7804 (2020), pp. 478+.
- [78] T. Mimura, T. Shimizu, and H. Funakubo. “Ferroelectricity in YO_{1.5}-HfO₂ Films around 1 μm in Thickness”. *Applied Physics Letters* 115 (2019), p. 032901.
- [79] E. D. Grimley, T. Schenk, X. Sang, M. Pešić, U. Schroeder, T. Mikolajick, and J. M. LeBeau. “Structural Changes Underlying Field-Cycling Phenomena in Ferroelectric HfO₂ Thin Films”. *Advanced Electronic Materials* 2.9 (2016).
- [80] P. Buragohain, C. Richter, T. Schenk, H. Lu, T. Mikolajick, U. Schroeder, and A. Gruverman. “Nanoscope Studies of Domain Structure Dynamics in Ferroelectric La: HfO₂ Capacitors”. *Applied Physics Letters* 112.22 (2018), pp. 222901/1–5.
- [81] K. Lee, K. Park, H. J. Lee, M. S. Song, K. C. Lee, J. Namkung, J. H. Lee, J. Park, and S. C. Chae. “Enhanced Ferroelectric Switching Speed of Si-doped HfO₂ Thin Film Tailored by Oxygen Deficiency”. *Scientific Reports* 11.1 (2021), pp. 6290/1–9.

- [82] J. F. Scott and M. Dawber. “Oxygen-Vacancy Ordering as a Fatigue Mechanism in Perovskite Ferroelectrics”. *Applied Physics Letters, USA* 76.25 (2000), pp. 3801–3803.
- [83] T. Mimura, T. Shimizu, T. Kiguchi, A. Akama, T. J. Konno, Y. Katsuya, O. Sakata, and H. Funakubo. “Effects of Heat Treatment and in Situ High-Temperature X-ray Diffraction Study on the Formation of Ferroelectric Epitaxial Y-doped HfO₂ Film”. *Japanese Journal of Applied Physics* 58 (2019), SBBB09/1–5.
- [84] S. Estandía, N. Dix, M. F. Chisholm, I. Fina, and F. Sánchez. “Domain-Matching Epitaxy of Ferroelectric Hf_{0.5}Zr_{0.5}O₂(111) on La_{2/3}Sr_{1/3}MnO₃(001)”. *Crystal Growth & Design* 20.6 (2020), pp. 3801–3806.
- [85] J. Lyu, I. Fina, R. Solanas, J. Fontcuberta, and F. Sánchez. “Robust Ferroelectricity in Epitaxial Hf_{1/2}Zr_{1/2}O₂ Thin Films”. *Applied Physics Letters* 113.8 (2018), p. 082902.
- [86] P. Nukala, Y. Wei, V. de Haas, Q. Guo, J. Antoja-Lleonart, and B. Noheda. “Guidelines for the Stabilization of a Polar Rhombohedral Phase in Epitaxial Hf_{0.5}Zr_{0.5}O₂ Thin Films”. *Ferroelectrics* 569.1 (2020), pp. 148–163.
- [87] Y. Shen, M. Haruta, I.-C. Lin, L. Xie, D. Kan, and Y. Shimakawa. “Stabilization of Ferroelectric Hf_{0.5}Zr_{0.5}O₂ Epitaxial Films via Monolayer Reconstruction Driven by Valence-Dependent Interfacial Redox Reaction and Intralayer Electron Transfer”. *Physical Review Materials* 7.11 (2023), p. 114405.
- [88] R. Eason. *Pulsed Laser Deposition of Thin Films Applications-led Growth of Functional Materials*. 2007.
- [89] D. H. Lowndes, D. B. Geohegan, A. A. Puretzky, D. P. Norton, and C. M. Rouleau. “Synthesis of Novel Thin-Film Materials by Pulsed Laser Deposition”. *Science* 273.5277 (1996), pp. 898–903.
- [90] N. A. Shepelin, Z. P. Tehrani, N. Ohannessian, C. W. Schneider, D. Pergolesi, and T. Lippert. “A Practical Guide to Pulsed Laser Deposition”. *Chemical Society Reviews* 52.7 (2023), pp. 2294–2321.
- [91] D. Blank, G. Koster, E. Van Setten, P. Slycke, and H. Rogalla. “Imposed Layer-by-Layer Growth by Pulsed Laser Interval Deposition”. *Applied Physics A: Materials Science and Processing* 69.7 (2000), pp. 223–226.
- [92] G. Rijnders and D. H. A. Blank. “In Situ Diagnostics by High-Pressure RHEED During PLD”. *Pulsed Laser Deposition of Thin Films: Applications-Led Growth of Functional Materials*. Wiley, 2006, pp. 85–97.
- [93] K. Wasa, Kanno, Isaku, and Kotera, Hidetoshi. *Handbook of Sputter Deposition Technology*. 2nd ed. 2012.
- [94] D. M. Mattox. “Physical Sputtering and Sputter Deposition (Sputtering)”. *Handbook of Physical Vapor Deposition (PVD) Processing*. 2010, pp. 237–286.
- [95] D. Depla and S. Mahieu. *Reactive Sputter Deposition*. 2008.

- [96] B. Voigtländer. *Scanning Probe Microscopy*. NanoScience and Technology. Springer, 2015.
- [97] M. P. Murrell, M. E. Welland, S. J. O’Shea, T. M. H. Wong, J. R. Barnes, A. W. McKinnon, M. Heyns, and S. Verhaverbeke. “Spatially Resolved Electrical Measurements of SiO₂ Gate Oxides Using Atomic Force Microscopy”. *Applied Physics Letters* 62.7 (1993), pp. 786–788.
- [98] M. Lanza, U. Celano, and F. Miao. “Nanoscale Characterization of Resistive Switching Using Advanced Conductive Atomic Force Microscopy Based Setups”. *Journal of Electroceramics* 39.1 (2017), pp. 94–108.
- [99] A. Guinier. *X-Ray Diffraction In Crystals, Imperfect Crystals , and Amorphous Bodies*. W. H. Freeman and Company, 1963.
- [100] E. Chason and T. M. Mayer. “Thin Film and Surface Characterization by Specular X-ray Reflectivity”. *Critical Reviews in Solid State and Materials Sciences* 22.1 (1997), pp. 1–67.
- [101] S. Huefner. *Photoelectron Spectroscopy: Principles and Applications*. 1995.
- [102] S. Hofmann. *Auger- and X-Ray Photoelectron Spectroscopy in Materials Science: A User-Oriented Guide*. Vol. 49. Springer Series in Surface Sciences. Berlin, Heidelberg: Springer Berlin Heidelberg, 2013.
- [103] M. T. Greiner, L. Chai, M. G. Helander, W. M. Tang, and Z. H. Lu. “Transition Metal Oxide Work Functions: The Influence of Cation Oxidation State and Oxygen Vacancies”. *Advanced Functional Materials* 22.21 (2012), pp. 4557–4568.
- [104] D. Céolin et al. “Hard X-ray Photoelectron Spectroscopy on the GALAXIES Beamline at the SOLEIL Synchrotron”. *Journal of Electron Spectroscopy and Related Phenomena*. Recent Advances in Hard X-ray Photoelectron Spectroscopy (HAXPES) 190 (2013), pp. 188–192.
- [105] E. E. Alp, S. M. Mini, and M. Ramanathan. *X-Ray Absorption Spectroscopy: EXAFS (Extended X-ray Absorption Fine Structure) and XANES (X-ray Absorption Near Edge Structure)*. Tech. rep. CONF-900190-1. Argonne National Lab., IL (USA), 1990.
- [106] J. Yano and V. K. Yachandra. “X-Ray Absorption Spectroscopy”. *Photosynthesis Research* 102.2 (2009), pp. 241–254.
- [107] J. Chen. “NEXAFS Investigations of Transition Metal Oxides, Nitrides, Carbides, Sulfides and Other Interstitial Compounds”. *Surface Science Reports* 30.1-3 (1997), pp. 1–152.
- [108] F. Frati, M. O. J. Y. Hunault, and F. M. F. de Groot. “Oxygen K-edge X-ray Absorption Spectra”. *Chemical Reviews* 120.9 (2020), pp. 4056–4110.
- [109] D.-Y. Cho, H.-S. Jung, and C. S. Hwang. “Structural Properties and Electronic Structure of HfO₂-ZrO₂ Composite Films”. *Physical Review B* 82.9 (2010), p. 094104.
- [110] C. M. Schneider and G. Schönhense. “Investigating Surface Magnetism by Means of Photoexcitation Electron Emission Microscopy”. *Reports on Progress in Physics* 65.12 (2002), p. 1785.

- [111] J. Feng and A. Scholl. *Photoemission Electron Microscopy (PEEM)*. In: Hawkes P.W., Spence J.C.H. (Eds) *Science of Microscopy*. Tech. rep. 2007.
- [112] O. Renault, N. Barrett, A. Bailly, L. F. Zagonel, D. Mariolle, J. C. Cezar, N. B. Brookes, K. Winkler, B. Krömker, and D. Funnemann. “Energy-Filtered XPEEM with *NanoESCA* Using Synchrotron and Laboratory X-ray Sources: Principles and First Demonstrated Results”. *Surface Science*. Proceedings of the Fifth International Conference on LEEM/PEEM 601.20 (2007), pp. 4727–4732.
- [113] A. Locatelli, L. Aballe, T. O. Montes, M. Kiskinova, and E. Bauer. *Photoemission Electron Microscopy with Chemical Sensitivity: SPELEEM Methods and Applications*. Tech. rep. 2006.
- [114] Y. Niu, N. Vinogradov, A. Preobrajenski, C. Struzzi, B. Sarpi, L. Zhu, E. Golias, and A. Zakharov. “MAXPEEM: A Spectromicroscopy Beamline at MAX IV Laboratory”. *Journal of Synchrotron Radiation* 30.2 (2023), pp. 468–478.
- [115] T. O. Montes and A. Locatelli. “Angle-Resolved X-ray Photoemission Electron Microscopy”. *Journal of Electron Spectroscopy and Related Phenomena*. Photoelectron Microscopy, Time Resolved Pump-Probe PES 185.10 (2012), pp. 323–329.
- [116] J. M. Börgers. “Combining Experimental and Computational Approaches to Characterise and Understand Oxygen Diffusion in (La,Sr)MnO₃”. PhD thesis. 2022.
- [117] J. Lyu, I. Fina, R. Solanas, J. Fontcuberta, and F. Sánchez. “Growth Window of Ferroelectric Epitaxial Hf_{0.5}Zr_{0.5}O₂ Thin Films”. *ACS Applied Electronic Materials* 1.2 (2019), pp. 220–228.
- [118] K. Pinggen. *Pulsed Laser Deposition and Characterisation of Epitaxial HfO₂ Thin Films*. Tech. rep. 2020.
- [119] J. Garcia-Barriocanal, A. Rivera-Calzada, M. Varela, Z. Sefrioui, E. Iborra, C. Leon, S. J. Pennycook, and J. Santamaria. “Colossal Ionic Conductivity at Interfaces of Epitaxial ZrO₂:Y₂O₃/SrTiO₃ Heterostructures”. *Science* 321.5889 (2008), pp. 676–680.
- [120] M. Hyuk Park, H. Joon Kim, Y. Jin Kim, W. Lee, T. Moon, and C. Seong Hwang. “Evolution of Phases and Ferroelectric Properties of Thin Hf_{0.5}Zr_{0.5}O₂ Films According to the Thickness and Annealing Temperature”. *Applied Physics Letters* 102.24 (2013), p. 242905.
- [121] N. Kaiser, Y.-J. Song, T. Vogel, E. Piros, T. Kim, P. Schreyer, S. Petzold, R. Valentí, and L. Alff. “Crystal and Electronic Structure of Oxygen Vacancy Stabilized Rhombohedral Hafnium Oxide”. *ACS Applied Electronic Materials* 5.2 (2023), pp. 754–763.
- [122] Y. Shen, K. Ooe, X. Yuan, T. Yamada, S. Kobayashi, M. Haruta, D. Kan, and Y. Shimakawa. “Ferroelectric Freestanding Hafnia Membranes with Metastable Rhombohedral Structure down to 1-Nm-Thick”. *Nature Communications* 15.1 (2024), p. 4789.
- [123] DoITPoMS. *The Interactive Ellingham Diagram*. Department of Materials Science & Metallurgy, University of Cambridge, 2004.

- [124] K. McKenna and A. Shluger. “The Interaction of Oxygen Vacancies with Grain Boundaries in Monoclinic HfO₂”. *Applied Physics Letters* 95.22 (2009), p. 222111.
- [125] Y. Zheng et al. “Atomic-Scale Characterization of Defects Generation during Fatigue in Ferroelectric Hf_{0.5}Zr_{0.5}O₂ Films: Vacancy Generation and Lattice Dislocation”. *2021 IEEE International Electron Devices Meeting (IEDM)*. 2021, pp. 33.5.1–33.5.4.
- [126] N. Schmidt, N. Kaiser, T. Vogel, E. Piros, S. Karthaeuser, R. Waser, L. Alff, and R. Dittmann. “Impact of Non-Stoichiometric Phases and Grain Boundaries on the Nanoscale Forming and Switching of HfO_x Thin Films”. *Advanced Electronic Materials* 2300693 (2024).
- [127] G. Bersuker et al. “Grain Boundary-Driven Leakage Path Formation in HfO₂ Dielectrics”. *Solid-State Electronics* 65–66 (2011), pp. 146–150.
- [128] O. Pirrotta, L. Larcher, M. Lanza, A. Padovani, M. Porti, M. Nafria, and G. Bersuker. “Leakage Current through the Poly-Crystalline HfO₂: Trap Densities at Grains and Grain Boundaries”. *Journal of Applied Physics* 114.13 (2013), pp. 134503/1–5.
- [129] M. Lederer, T. Kämpfe, R. Olivo, D. Lehninger, C. Mart, S. Kirbach, T. Ali, P. Polakowski, L. Roy, and K. Seidel. “Local Crystallographic Phase Detection and Texture Mapping in Ferroelectric Zr Doped HfO₂ Films by Transmission-EBSD”. *Applied Physics Letters* 115.22 (2019), p. 222902.
- [130] M. C. Sulzbach, S. Estandía, X. Long, J. Lyu, N. Dix, J. Gàzquez, M. F. Chisholm, F. Sánchez, I. Fina, and J. Fontcuberta. “Unraveling Ferroelectric Polarization and Ionic Contributions to Electroresistance in Epitaxial Hf_{0.5}Zr_{0.5}O₂ Tunnel Junctions”. *Advanced Electronic Materials* 6.1 (2020), p. 1900852.
- [131] H. Lu et al. “Electrically Induced Cancellation and Inversion of Piezoelectricity in Ferroelectric Hf_{0.5}Zr_{0.5}O₂”. *Nature Communications* 15.1 (2024), p. 860.
- [132] Baeumer, C. “Spectroscopic Characterization of Local Valence Change Processes in Resistively Switching Complex Oxides”. PhD thesis. 2016.
- [133] T. Heisig. “Spectromicroscopic Investigation of Local Redox Processes in Resistive Switching Transition Metal Oxides”. PhD thesis. 2021.
- [134] J. Knabe et al. “Oxygen Vacancy Dynamics in Different Switching Modes of Hf_{0.5}Zr_{0.5}O_{2-δ}”. *ACS Nano* 19.32 (2025), pp. 29405–29415.
- [135] A. Koehl. “Micro-Spectroscopic Investigation of Valence Change Processes in Resistive Switching SrTiO₃ Thin Films”. PhD thesis. 2014.
- [136] B. Arndt. “Resistive Switching in Pr_{1-x}CaxMnO₃/YSZ: Conclusive Model and Switching Kinetics”. PhD thesis. 2022.
- [137] S. Jesse, A. P. Baddorf, and S. V. Kalinin. “Switching Spectroscopy Piezoresponse Force Microscopy of Ferroelectric Materials”. *Applied Physics Letters* 88.6 (2006), p. 062908.

- [138] R. K. Vasudevan, N. Balke, P. Maksymovych, S. Jesse, and S. V. Kalinin. “Ferroelectric or Non-Ferroelectric: Why so Many Materials Exhibit “Ferroelectricity” on the Nanoscale”. *Applied Physics Reviews* 4.2 (2017), p. 021302.
- [139] C. Daumont et al. “Strain Dependence of Polarization and Piezoelectric Response in Epitaxial BiFeO₃ Thin Films”. *Journal of Physics: Condensed Matter* 24.16 (2012), p. 162202.
- [140] Y. Wei, X. Wang, J. Zhu, X. Wang, and J. Jia. “Dielectric, Ferroelectric, and Piezoelectric Properties of BiFeO₃–BaTiO₃ Ceramics”. *Journal of the American Ceramic Society* 96.10 (2013), pp. 3163–3168.
- [141] J. Liu, S. Liu, L. H. Liu, B. Hanrahan, and S. T. Pantelides. “Origin of Pyroelectricity in Ferroelectric HfO₂”. *Physical Review Applied* 12.3 (2019), p. 034032.
- [142] S. Dutta, P. Buragohain, S. Glinsek, C. Richter, H. Aramberri, H. Lu, U. Schroeder, E. Defay, A. Gruverman, and J. Íñiguez. “Piezoelectricity in Hafnia”. *Nature Communications* 12.1 (2021), p. 7301.
- [143] S. Starschich, T. Schenk, U. Schroeder, and U. Boettger. “Ferroelectric and Piezoelectric Properties of Hf_{1-x}ZrxO₂ and Pure ZrO₂ Films”. *Applied Physics Letters* 110.18 (2017), p. 182905.
- [144] A. Chouprik, R. Kirtaev, E. Korostylev, V. Mikheev, M. Spiridonov, and D. Negrov. “Nanoscale Doping and Its Impact on the Ferroelectric and Piezoelectric Properties of Hf_{0.5}Zr_{0.5}O₂”. *Nanomaterials* 12.9 (2022), p. 1483.
- [145] P. Buragohain et al. “Quantification of the Electromechanical Measurements by Piezoresponse Force Microscopy”. *Advanced Materials* 34.47 (2022), p. 2206237.
- [146] H. Akinaga and H. Shima. “Resistive Random Access Memory (ReRAM) Based on Metal Oxides”. *Proceedings of the Ieee* 98.12 (2010), pp. 2237–2251.
- [147] D. Ielmini. “Resistive Switching Memories Based on Metal Oxides: Mechanisms, Reliability and Scaling”. *Semiconductor Science and Technology* 31.6 (2016), p. 063002.
- [148] S. Brivio, S. Spiga, and D. Ielmini. “HfO₂-based Resistive Switching Memory Devices for Neuromorphic Computing”. *The Institute of Physics* 2.4 (2022).
- [149] S. U. Sharath, J. Kurian, P. Komissinskiy, E. Hildebrandt, T. Bertaud, C. Walczyk, P. Calka, T. Schroeder, and L. Alf. “Thickness Independent Reduced Forming Voltage in Oxygen Engineered HfO₂ Based Resistive Switching Memories”. *Applied Physics Letters* 105.7 (2014), pp. 73505/1–4.
- [150] Y. Wang et al. “Reliable Resistive Switching of Epitaxial Single Crystalline Cubic Y-HfO₂ RRAMs with Si as Bottom Electrodes”. *Nanotechnology* 31.20 (2020), pp. 205203/1–7.
- [151] J. O. Capulong, B. D. Briggs, S. M. Bishop, M. Q. Hovish, R. J. Matyi, and N. C. Cady. “Effect of Crystallinity on Endurance and Switching Behavior of HfO_x-based Resistive Memory Devices”. 2012, pp. 22–25.

- [152] C. Lin, Y. Wu, T. Hung, and C. Hou. “Impact of Dielectric Crystallinity on the Resistive Switching Characteristics of ZrTiO_x-based Metal-Insulator-Metal Devices”. *Microelectronic Engineering* 109 (2013), pp. 374–377.
- [153] X. Guan, S. Yu, and H. S. Wong. “On the Switching Parameter Variation of Metal-Oxide RRAM - Part I: Physical Modeling and Simulation Methodology”. *IEEE Transactions on Electron Devices* 59.4 (2012), pp. 1172–1182.
- [154] J. Knabe, F. Berg, K. T. Goss, U. Boettger, and R. Dittmann. “Dual-Mode Operation of Epitaxial Hf_{0.5}Zr_{0.5}O₂: Ferroelectric and Filamentary-Type Resistive Switching”. *physica status solidi (a)* 221.22 (2023), p. 2300409.
- [155] K. Fleck, C. La Torre, N. Aslam, S. Hoffmann-Eifert, U. Böttger, and S. Menzel. “Uniting Gradual and Abrupt SET Processes in Resistive Switching Oxides”. *Physical Review Applied* 6.6 (2016), p. 064015.
- [156] A. Hardtdegen, C. La Torre, F. Cüppers, S. Menzel, R. Waser, and S. Hoffmann-Eifert. “Improved Switching Stability and the Effect of an Internal Series Resistor in HfO₂/TiO_x Bilayer ReRAM Cells”. *IEEE Transactions on Electron Devices* 65.8 (2018), pp. 3229–3236.
- [157] L. Zhao, H. Chen, S. Wu, Z. Jiang, S. Yu, T. Hou, H. P. Wong, and Y. Nishi. “Multi-Level Control of Conductive Nano-Filament Evolution in HfO₂ ReRAM by Pulse-Train Operations”. *Nanoscale* 6 (2014), pp. 5698–5702.
- [158] C. Giovinazzo, J. Sandrini, E. Shahrabi, O. T. Celik, Y. Leblebici, and C. Ricciardi. “Analog Control of Retainable Resistance Multistates in HfO₂ Resistive-Switching Random Access Memories (ReRAMs)”. *Applied Electronic Materials* 1 (2019), pp. 900–909.
- [159] H. Dou, M. Hellenbrand, M. Xiao, Z. Hu, S. Kunwar, A. Chen, J. L. MacManus-Driscoll, Q. Jia, and H. Wang. *Engineering of Grain Boundaries in CeO₂ Enabling Tailorable Resistive Switching Properties*. Tech. rep. 2023.
- [160] S. Park, S. Klett, T. Ivanov, A. Knauer, J. Doell, and M. Ziegler. “Engineering Method for Tailoring Electrical Characteristics in TiN/TiO_x/HfO_x/Au Bi-Layer Oxide Memristive Devices”. *Frontiers in Nanotechnology* 3 (2021), p. 29.
- [161] S. Won, S. Y. Lee, J. Park, and H. Seo. “Forming-Less and Non-Volatile Resistive Switching in WOX by Oxygen Vacancy Control at Interfaces”. *Scientific Reports* 7 (2017), pp. 10186/1–8.
- [162] D. Cho, M. Lübben, S. Wiefels, K. Lee, and I. Valov. “Interfacial Metal – Oxide Interactions in Resistive Switching Memories”. *ACS Applied Materials & Interfaces* 9.22 (2017), pp. 19287–19295.
- [163] A. Sawa and R. Meyer. *Interface Type Switching*. Tech. rep. 2016, pp. 457–482.
- [164] H. Y. Lee, Y. S. Chen, P. S. Chen, T. Y. Wu, F. Chen, C. C. Wang, P. J. Tzeng, M. Tsai, and C. Lien. “Low-Power and Nanosecond Switching in Robust Hafnium Oxide Resistive Memory With a Thin Ti Cap”. *Ieee Electron Device Letters* 31.1 (2010), pp. 44–46.

- [165] A. Hardtdegen, H. Zhang, and S. Hoffmann-Eifert. “Tuning the Performance of Pt/HfO₂/Ti/Pt ReRAM Devices Obtained from Plasma-Enhanced Atomic Layer Deposition for HfO₂ Thin Films”. *ECS Transactions* 75.6 (2016), pp. 177–184.
- [166] S. Park, B. Spetzler, T. Ivanov, and M. Ziegler. “Multilayer Redox-Based HfO_x/Al₂O₃/TiO₂ Memristive Structures for Neuromorphic Computing”. *Scientific Reports* 12 (2022), p. 18266.
- [167] S. Tirano, L. Perniola, J. Buckley, J. Cluzel, V. Jousseau, C. Muller, D. Deleruyelle, B. De Salvo, and G. Reimbold. *Accurate Analysis of Parasitic Current Overshoot during Forming Operation in RRAMs*. Tech. rep. 2011.
- [168] Y. M. Lu, M. Noman, W. Chen, P. A. Salvador, J. A. Bain, and M. Skowronski. “Elimination of High Transient Currents and Electrode Damage during Electroformation of TiO₂-based Resistive Switching Devices”. *Journal of Physics D: Applied Physics* 45.39 (2012), p. 395101.
- [169] X. Long, H. Tan, F. Sánchez, I. Fina, and J. Fontcuberta. “Ferroelectric Electroresistance after a Breakdown in Epitaxial Hf_{0.5}Zr_{0.5}O₂ Tunnel Junctions”. *ACS Applied Electronic Materials* 5.2 (2023), pp. 740–747.
- [170] Z. Wen, C. Li, D. Wu, A. Li, and N. Ming. “Ferroelectric-Field-Effect-Enhanced Electroresistance in Metal/Ferroelectric/Semiconductor Tunnel Junctions”. *Nature Materials* 12.7 (2013), pp. 617–621.
- [171] R. Degraeve, A. Fantini, N. Raghavan, L. Goux, S. Clima, B. Govoreanu, A. Belmonte, D. Linten, and M. Jurczak. “Causes and Consequences of the Stochastic Aspect of Filamentary RRAM”. *Microelectronic Engineering* 147 (2015), pp. 171–175.
- [172] H. Y. Lee, P. S. Chen, T. Y. Wu, Y. S. Chen, C. C. Wang, P. J. Tzeng, C. H. Lin, F. Chen, C. H. Lien, and M. J. Tsai. “Low Power and High Speed Bipolar Switching with a Thin Reactive Ti Buffer Layer in Robust HfO₂ Based RRAM”. *Technical Digest - International Electron Devices Meeting, IEDM* (2008), pp. 3–6.
- [173] S. U. Sharath et al. “Towards Forming-Free Resistive Switching in Oxygen Engineered HfO_{2-x}”. *Applied Physics Letters* 104.6 (2014), pp. 3–8.
- [174] L. Goux, Y. Y. Chen, L. Pantisano, X. P. Wang, G. Groeseneken, M. Jurczak, and D. J. Wouters. “On the Gradual Unipolar and Bipolar Resistive Switching of TiN/HfO₂/Pt Memory Systems”. *Electrochemical and Solid-State Letters* 13.6 (2010), pp. 4–7.
- [175] A. Marchewka, B. Roesgen, K. Skaja, H. Du, C.-L. Jia, J. Mayer, V. Rana, R. Waser, and S. Menzel. “Nanoionic Resistive Switching Memories: On the Physical Nature of the Dynamic Reset Process”. *Advanced Electronic Materials* 2.1 (2016), p. 1500233.
- [176] C. Baeumer et al. “Quantifying Redox-Induced Schottky Barrier Variations in Memristive Devices via in Operando Spectromicroscopy with Graphene Electrodes”. *Nature Communications* 7.1 (2016), p. 12398.
- [177] S. Brivio, G. Tallarida, E. Cianci, and S. Spiga. “Formation and Disruption of Conductive Filaments in a HfO₂/TiN Structure”. *Nanotechnology* 25.38 (2014), p. 385705.

- [178] D.-Y. Cho, J.-M. Lee, S.-J. Oh, H. Jang, J.-Y. Kim, J.-H. Park, and A. Tanaka. “Influence of Oxygen Vacancies on the Electronic Structure of HfO Films”. *Physical Review B* 76.16 (2007), p. 165411.
- [179] P. Calka et al. “Chemical and Structural Properties of Conducting Nanofilaments in TiN/HfO₂-based Resistive Switching Structures”. *Nanotechnology* 24.8 (2013).
- [180] Y. Yang, X. Zhang, L. Qin, Q. Zeng, X. Qiu, and R. Huang. “Probing Nanoscale Oxygen Ion Motion in Memristive Systems”. *Nature Communications* 8.1 (2017), p. 15173.
- [181] U. Celano, T. Hantschel, G. Giammaria, R. Chintala, T. Conard, H. Bender, and W. Vandervorst. “Evaluation of the Electrical Contact Area in Contact-Mode Scanning Probe Microscopy”. *Journal of Applied Physics* 117.21 (2015), p. 214305.
- [182] S. Privitera, G. Bersuker, B. Butcher, A. Kalantarian, S. Lombardo, C. Bongiorno, R. Geer, D. C. Gilmer, and P. D. Kirsch. “Microscopy Study of the Conductive Filament in HfO₂ Resistive Switching Memory Devices”. *Microelectronic Engineering. Insulating Films on Semiconductors 2013* 109 (2013), pp. 75–78.
- [183] Y. Zhang et al. “Evolution of the Conductive Filament System in HfO₂-based Memristors Observed by Direct Atomic-Scale Imaging”. *Nature Communications* 12.1 (2021), p. 7232.
- [184] A. Kindsmüller, C. Schmitz, C. Wiemann, K. Skaja, D. J. Wouters, R. Waser, C. M. Schneider, and R. Dittmann. “Valence Change Detection in Memristive Oxide Based Heterostructure Cells by Hard X-ray Photoelectron Emission Spectroscopy”. *APL Materials* 6.046106 (2018).
- [185] S. Deshmukh, M. M. Rojo, E. Yalon, S. Vaziri, C. Koroglu, R. Islam, R. A. Iglesias, K. Saraswat, and E. Pop. “Direct Measurement of Nanoscale Filamentary Hot Spots in Resistive Memory Devices”. *Science Advances* 8.13 (2022), eabk1514.
- [186] C. Bengel, A. Siemon, F. Cüppers, S. Hoffmann-Eifert, A. Hardtdegen, M. von Witzleben, L. Hellmich, R. Waser, and S. Menzel. “Variability-Aware Modeling of Filamentary Oxide Based Bipolar Resistive Switching Cells Using SPICE Level Compact Models”. *IEEE Transactions on Circuits and Systems I: Regular Papers* 67.12 (2020), pp. 4618–4630.
- [187] C. Bengel, K. Zhang, J. Mohr, T. Ziegler, S. Wiefels, R. Waser, D. Wouters, and S. Menzel. “Tailor-Made Synaptic Dynamics Based on Memristive Devices”. *Frontiers in Electronic Materials* 3 (2023).
- [188] K. Skaja, M. Andrae, V. Rana, R. Waser, R. Dittmann, and C. Baeumer. “Reduction of the Forming Voltage through Tailored Oxygen Non-Stoichiometry in Tantalum Oxide ReRAM Devices”. *Scientific Reports* 8 (2018), pp. 10861/1–7.
- [189] P. Lackner, Z. Zou, S. Mayr, U. Diebold, and M. Schmid. “Using Photoelectron Spectroscopy to Observe Oxygen Spillover to Zirconia”. *Physical Chemistry Chemical Physics* 21.32 (2019), pp. 17613–17620.

- [190] C. Lenser, A. Koehl, I. Slipukhina, H. Du, M. Patt, V. Feyer, C. M. Schneider, M. Lezaic, R. Waser, and R. Dittmann. “Formation and Movement of Cationic Defects During Forming and Resistive Switching in SrTiO₃ Thin Film Devices”. *Advanced Functional Materials* 25.40 (2015), pp. 6360–6368.
- [191] T. Heisig, J. Kler, H. Du, C. Baeumer, F. Hensling, M. Glöss, M. Moors, A. Locatelli, T. O. Montes, and F. Genuzio. “Antiphase Boundaries Constitute Fast Cation Diffusion Paths in SrTiO₃ Memristive Devices”. *Advanced Functional Materials* 25 (2020), p. 2004118.
- [192] H. Jalili, Y. Chen, and B. Yildiz. “Structural, Chemical, and Electronic State on La_{0.7}Sr_{0.3}MnO₃ Dense Thin-Film Surfaces at High Temperature: Surface Segregation”. *ECS Transactions* 28.11 (2010), p. 235.
- [193] A. K. Tagantsev, I. Stolichnov, E. L. Colla, and N. Setter. “Polarization Fatigue in Ferroelectric Films: Basic Experimental Findings, Phenomenological Scenarios, and Microscopic Features”. *Journal of Applied Physics* 90.3 (2001), pp. 1387–1402.
- [194] Y. Lee, Y. Goh, J. Hwang, D. Das, and S. Jeon. “The Influence of Top and Bottom Metal Electrodes on Ferroelectricity of Hafnia”. *IEEE Transactions on Electron Devices* 68.2 (2021), pp. 523–528.
- [195] M. C. Biesinger, B. P. Payne, A. P. Grosvenor, L. W. M. Lau, A. R. Gerson, and R. S. C. Smart. “Resolving Surface Chemical States in XPS Analysis of First Row Transition Metals, Oxides and Hydroxides: Cr, Mn, Fe, Co and Ni”. *Applied Surface Science* 257.7 (2011), pp. 2717–2730.
- [196] B. Gilbert, B. H. Frazer, A. Belz, P. G. Conrad, K. H. Nealson, D. Haskel, J. C. Lang, G. Srajer, and G. De Stasio. “Multiple Scattering Calculations of Bonding and X-ray Absorption Spectroscopy of Manganese Oxides”. *The Journal of Physical Chemistry A* 107.16 (2003), pp. 2839–2847.
- [197] N. Zagni, F. M. Puglisi, P. Pavan, and M. A. Alam. “Reliability of HfO₂-Based Ferroelectric FETs: A Critical Review of Current and Future Challenges”. *Proceedings of the IEEE* 111.2 (2023), pp. 158–184.
- [198] P. Liao, Y. Chang, Y.-H. Lee, Y. Lin, S. Yeong, R. Hwang, V. Hou, C. Nien, R. Lu, and C. Lin. “Characterization of Fatigue and Its Recovery Behavior in Ferroelectric HfZrO”. *2021 Symposium on VLSI Technology*. 2021, pp. 1–2.
- [199] T. Song, S. Estandía, H. Tan, N. Dix, J. Gàzquez, I. Fina, and F. Sánchez. “Positive Effect of Parasitic Monoclinic Phase of Hf_{0.5}Zr_{0.5}O₂ on Ferroelectric Endurance”. *Advanced Electronic Materials* 8.1 (2022), p. 2100420.
- [200] L. Baumgarten, T. Szyjka, T. Mittmann, A. Gloskovskii, C. Schlueter, T. Mikolajick, U. Schroeder, and M. Müller. “Smart Design of Fermi Level Pinning in HfO₂ -Based Ferroelectric Memories”. *Advanced Functional Materials* 34.3 (2024), p. 2307120.

- [201] M. Qian, I. Fina, M. C. Sulzbach, F. Sánchez, and J. Fontcuberta. “Synergetic Electronic and Ionic Contributions to Electroresistance in Ferroelectric Capacitors”. *Advanced Electronic Materials* 5.3 (2019), p. 1800646.
- [202] M. Lanza, K. Zhang, M. Porti, M. Nafria, Z. Y. Shen, L. F. Liu, J. F. Kang, D. Gilmer, and G. Bersuker. “Grain Boundaries as Preferential Sites for Resistive Switching in the HfO₂ Resistive Random Access Memory Structures”. *Applied Physics Letters* 100.12 (2012), p. 123508.
- [203] S. Petzold et al. “Forming-Free Grain Boundary Engineered Hafnium Oxide Resistive Random Access Memory Devices”. *Advanced Electronic Materials* 5.10 (2019), p. 1900484.
- [204] J. Narayan. “Recent Progress in Thin Film Epitaxy across the Misfit Scale (2011 Acta Gold Medal Paper)”. *Acta Materialia* 61.8 (2013), pp. 2703–2724.
- [205] H. Kum, D. Lee, W. Kong, H. Kim, Y. Park, Y. Kim, Y. Baek, S.-H. Bae, K. Lee, and J. Kim. “Epitaxial Growth and Layer-Transfer Techniques for Heterogeneous Integration of Materials for Electronic and Photonic Devices”. *Nature Electronics* 2.10 (2019), pp. 439–450.
- [206] D. Lu, D. J. Baek, S. S. Hong, L. F. Kourkoutis, Y. Hikita, and H. Y. Hwang. “Synthesis of Freestanding Single-Crystal Perovskite Films and Heterostructures by Etching of Sacrificial Water-Soluble Layers”. *Nature Materials* 15.12 (2016), pp. 1255–1260.
- [207] S. R. Bakaul et al. “Single Crystal Functional Oxides on Silicon”. *Nature Communications* 7.1 (2016), p. 10547.
- [208] J. Yoon et al. “GaAs Photovoltaics and Optoelectronics Using Releasable Multilayer Epitaxial Assemblies”. *Nature* 465.7296 (2010), pp. 329–333.
- [209] X. Jia, R. Guo, B. K. Tay, and X. Yan. “Flexible Ferroelectric Devices: Status and Applications”. *Advanced Functional Materials* 32.45 (2022), p. 2205933.
- [210] H. Zhong et al. “Large-Scale Hf_{0.5}Zr_{0.5}O₂ Membranes with Robust Ferroelectricity”. *Advanced Materials* 34.24 (2022), p. 2109889.
- [211] L. Shen et al. “Epitaxial Lift-Off of Centimeter-Scaled Spinel Ferrite Oxide Thin Films for Flexible Electronics”. *Advanced Materials* 29.33 (2017), p. 1702411.
- [212] D. Pesquera et al. “Beyond Substrates: Strain Engineering of Ferroelectric Membranes”. *Advanced Materials* 32.43 (2020), p. 2003780.
- [213] T. Song, H. Tan, N. Dix, R. Moalla, J. Lyu, G. Saint-Girons, R. Bachelet, F. Sánchez, and I. Fina. “Stabilization of the Ferroelectric Phase in Epitaxial Hf_{1-x}Zr_xO₂ Enabling Coexistence of Ferroelectric and Enhanced Piezoelectric Properties”. *ACS Applied Electronic Materials* 3.5 (2021), pp. 2106–2113.
- [214] K. Persson. *Materials Data on HfO₂ by Materials Project*. 2020.
- [215] H. Yu et al. “Flexible Inorganic Ferroelectric Thin Films for Nonvolatile Memory Devices”. *Advanced Functional Materials* 27.21 (2017), p. 1700461.

- [216] W. Xiao, C. Liu, Y. Peng, S. Zheng, Q. Feng, C. Zhang, J. Zhang, Y. Hao, M. Liao, and Y. Zhou. “Thermally Stable and Radiation Hard Ferroelectric $\text{Hf}_{0.5}\text{Zr}_{0.5}\text{O}_2$ Thin Films on Muscovite Mica for Flexible Nonvolatile Memory Applications”. *ACS Applied Electronic Materials* 1.6 (2019), pp. 919–927.
- [217] H. Liu et al. “Flexible Quasi-van Der Waals Ferroelectric Hafnium-Based Oxide for Integrated High-Performance Nonvolatile Memory”. *Advanced Science* 7.19 (2020), p. 2001266.
- [218] H. Joh, M. Jung, J. Hwang, Y. Goh, T. Jung, and S. Jeon. “Flexible Ferroelectric Hafnia-Based Synaptic Transistor by Focused-Microwave Annealing”. *ACS Applied Materials & Interfaces* 14.1 (2022), pp. 1326–1333.
- [219] A. Chouprik, V. Mikheev, I. Margolin, E. Kalika, M. Spiridonov, and D. Negrov. “Superflexible and Stretchable Ferroelectric Memory on a Biocompatible Platform”. *Advanced Electronic Materials* 10.5 (2024), p. 2300449.

List of Publications

Parts of this thesis have previously been published:

- **J. Knabe**, F. Berg, K. T. Goß, U. Boettger, and R. Dittmann. “Dual-Mode Operation of Epitaxial $\text{Hf}_{0.5}\text{Zr}_{0.5}\text{O}_2$: Ferroelectric and Filamentary-Type Resistive Switching”. *physica status solidi (a)* 221.22 (2023), p. 2300409.
- **J. Knabe**, K. Goss, Y.-P. Liu, E. Goliias, A. Zakharov, I. Cojocariu, M. Jugovac, A. Locatelli, T. O. Menteş, D. Céolin, A. Gutsche, D. Gogoi, M. L. Weber, R. Timm, R. Dittmann, "Oxygen Vacancy Dynamics in Different Switching Modes of $\text{Hf}_{0.5}\text{Zr}_{0.5}\text{O}_2$ ", *ACS Nano* 2025 19 (32), 29405-29415.

The following collaborative work is being prepared for publication and is not part of this thesis:

- M. L. Weber, T. Priamushko, D. Jennings, A. Staykov, D. Kim, A. Kaus, L. Heymann, A. Gutsche, **J. Knabe**, K. Goß, K. Nayak, D. Ceolin, R. Dittmann, R. Waser, S. Nemsak, Felix Gunkel, "Exsolution-driven surface activation and stability enhancement of perovskite oxide electrocatalysts for the oxygen evolution reaction".

Conference talks:

- **J. Knabe**, K. Goß, Y.-P. Liu, E. Goliias, A. Zakharov, I. Cojocariu, M. Jugovac, A. Locatelli, T. O. Menteş, D. Céolin, A. Gutsche, M. Weber, D. Gogoi, R. Timm, R. Dittmann, Oxygen vacancy dynamics in different switching modes of $\text{Hf}_{0.5}\text{Zr}_{0.5}\text{O}_{2-\delta}$, *NamLab High-k Workshop*, Dresden, 2024.
- **J. Knabe**, K. Goß, Y.-P. Liu, E. Goliias, A. Zakharov, I. Cojocariu, M. Jugovac, A. Locatelli, T. O. Menteş, D. Céolin, A. Gutsche, M. Weber, D. Gogoi, R. Timm, R. Dittmann, Spectroscopic investigation of ferroelectric and resistive switching in epitaxial $\text{Hf}_{0.5}\text{Zr}_{0.5}\text{O}_2$, *IEEE Ultrasonics, Ferroelectrics, and Frequency Control Joint Symposium (UFFC-JS)*, Taiwan, 2024 and *CMD-General Conference of the Condensed Matter Division*, Portugal, 2024.
- **J. Knabe**, F. Berg, K. T. Goß, U. Boettger, R. Dittmann, Interplay between ferroelectric and resistive switching in epitaxial $\text{Hf}_{0.5}\text{Zr}_{0.5}\text{O}_2$, *Fall Meeting of the European Materials Research Society (E-MRS)*, 2023.

Acknowledgements

This PhD journey has been both intellectually challenging and personally transformative, and I am deeply grateful to all those who have supported me along the way.

First and foremost, I would like to express my sincere gratitude to my supervisor, Prof. Dr. Regina Dittmann, for the opportunity to conduct my research in her institute and group, and for her encouragement and support throughout this project. Her insightful feedback and constructive criticism have significantly helped shape this thesis. I am also very grateful to Professor Dr. Klemradt for acting as co-examiner, and to the other members of my thesis committee.

I would like to thank everyone at PGI-7 for creating a positive collegial atmosphere during the roughly five years of my master's and PhD work here.

During all this time I couldn't have asked for a better office mate - thank you, Alexandros, for your continuous open ear and advice along the way.

A major part of my PhD involved a one of a kind beamtime marathon. Thank you, Kalle, for your big effort in making it all possible for both of us. Also, thanks to Alex Gutsche, Yen-Po Liu, Peijia Yuan, Moritz Weber and Daisy Gogoi for their great company and support during one or more of those beamtimes.

I would like to thank Lee-Kang Huang, who not only contributed to this work through his master's thesis but also taught me a lot about communication and mentorship.

Many thanks to Fenja Berg, Jan Lübben and Dr. Ulrich Böttger for the introduction to ferroelectrics and for the support in all things related. Thank you, also, Jacqueline Börgers and Sebastian Hamsch for countless help during the early days of my time at PGI-7. Special thanks go to the administrative and technical staff whose behind-the-scenes contributions were invaluable: Georg Pickartz, Marcel Gerst, Malte Deckers, Maria Garcia, Stephan Masberg, Shayan Shoja, Sylvia de Waal and Grigory Potemkin.

Lastly, special mention goes to the ZAT PLD team, for going through the highs and lows of operation together and to the lunch group, for making the daily breaks something to look forward to.

Finally, a big thank you goes to my friends and family! Thank you for believing in me and listening to me whenever I needed advice or just an ear to vent. This achievement is as much yours as it is mine.